SYNTHESIS, CHARACTERIZATION, AND MODIFICATION OF VARIOUS MESOPOROUS SILICA PHASES

DISSERTATION

zur Erlangung des Doktorgrades
des Fachbereichs Chemie
der Universität Hamburg

vorgelegt von

RALF KÖHN

aus Hamburg

Hamburg 2001

Die vorliegende Arbeit entstand in der Zeit von August 1997 bis Mai 2001 am Institut für Anorganische und Angewandte Chemie der Universität Hamburg in der Arbeitsgruppe von Prof. Dr. Michael Fröba

Gutachter: Prof. Dr. Michael Fröba
Gutachter: Prof. Dr. Dieter Rehder

Man kann alles lernen, wenn man nur will.

Mein Vater

Contents

Appendix I

Appendix II

1 Introduction

In 1992, researchers of the Mobil Oil Company reported a new concept in the synthesis of porous materials [1,2]. In contrast to the well-known synthesis of zeolites using single, solvated organic molecules or metal ions as templates, the new concept introduced self-assembled molecular arrays of amphiphilic surfactant molecules (lyotropic liquid crystals) as structure-directing agents[*]. Their removal leads to mesoporous[**] [3] molecular sieves with adjustable pore sizes ranging from 2 to 10 nm. The very regular pore arrangements and narrow pore size distributions of these new materials, denoted as M41S phases, are almost comparable to microporous zeolites [4]. Due to their larger pores and high surface areas these new materials are of great interest for size- and shape-selective applications. Therefore, attention arose from different fields of materials science, i.e. as sorption materials [5-14], as nanostructured host-guest compounds [15-20], and in catalysis [21-24]. The synthesis, characterization and applications of these new phases will be briefly discussed in the following chapters.

1.1 Synthesis and characterization of mesoporous silica

Originally, the M41S synthesis was carried out via an electrostatic templating route using cationic quaternary ammonium micelles (S^+), which act as structure-directing agents in order to mesostructure anionic inorganic precursors (I^-). This assembly, which is driven by electrostatic and steric interactions leading to charge-matching at the organic-inorganic interface, was extended to further combinations of ion pairs, including charge-reversed (S^-I^+) and counter-ion mediated ($S^+X^-I^+$ and $S^-X^+I^-$) synthetic pathways [25].

---

[*] A template leads to one particular, structurally unique (crystalline) product while a structure-directing agent gives one or more periodically ordered, but usually amorphous structures with respect to the short-range atomic structure.

[**] The IUPAC nomenclature divides porous materials in three different classes due to their pore diameter: macroporous (> 50 nm), mesoporous (2-50 nm), and microporous (< 2 nm).

It is also possible to use neutral surfactants (S^0) instead of charged structure-directing agents. So-called HMS[*] phases were formed using primary long-chain alkylamines in the presence of neutral silica species at pH 7 for the synthesis of mesoporous molecular sieves [26]. This neutral templating route is based on hydrogen-bonding interactions and self-assembly between neutral surfactants (S^0) and neutral inorganic precursors (I^0). Comparable interactions were used in the synthesis applying non-ionic surfactant molecules (N^0) [27]. Polyethylene oxide (PEO) surfactants were used as structure-directing agents to form the mesoporous silica molecular sieves MSU-X[**]. With triblock copolymers the mesoporous silica SBA-15[***] with pore diameters up to 30 nm were obtained. In contrast to the strong ionic interaction in the electrostatic templating route, the neutral and the non-ionic surfactants interact with the inorganic building units via weak hydrogen bonds. Compared with electrostatically templated mesoporous silica, these materials exhibit thicker framework walls, smaller X-ray scattering domain sizes, and substantially improved textural mesoporosity.

Very strong organic-inorganic interactions are achieved by so-called ligand-assisted liquid-crystal templating in which covalent bonds are formed between the inorganic precursor species and the organic surfactants prior to the self-assembly process [28]. Recently, it could be shown that appropriate surfactants can even act as structure-directing agent and as reactants in the course of the synthesis [29]. Extended information and a more comprehensive description on the variety of different synthetic pathways were given in various publications within the last years [15,21,22,30-37]. The further discussion will be focused on the electrostatic templating route (S^+I^-), which provides the basis for this work.

The first mechanism for this electrostatic templating route was proposed in 1992 as so-called „liquid crystal templating“ (LCT) [2]. Two main pathways are shown in Figure 1-1. The “liquid crystal initiated” pathway starts with the formation of the liquid-crystal phase before the silicate species are added, in contrast to the “silicate anion initiated” pathway, in which the addition of the silicate results in the ordering of the subsequent silicate-encased surfactant micelles.

---

[*] HMS stands for *h*exagonal *m*esoporous *s*ilica.

[**] MSU stands for *M*ichigan *S*tate *U*niversity and the X denotes the specific materials templated by a particular PEO-based surfactant.

[***] SBA-15 stands for *S*anta *Ba*rbara No. 15.

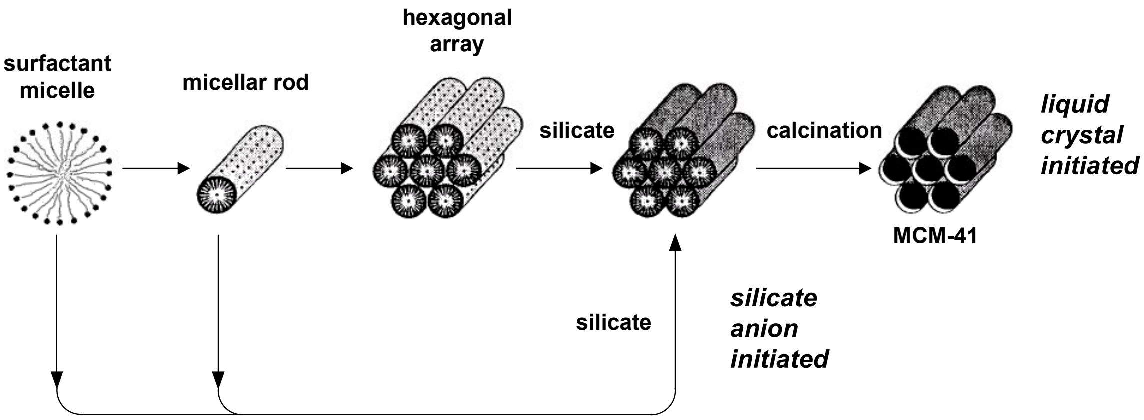

Figure 1-1: "Liquid-crystal templating" (LCT) mechanism [2] showing two possible pathways for the formation of mesoporous MCM-41 silica structure: liquid-crystal initiated (top) and silicate anion initiated (bottom).

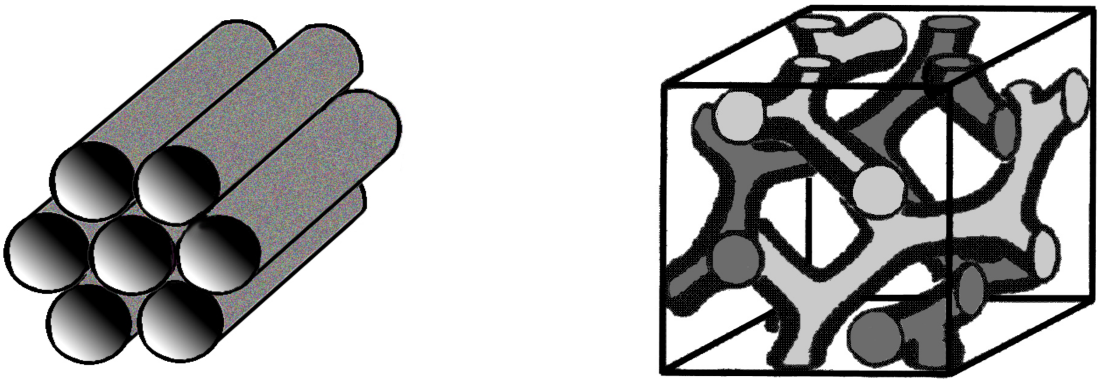

Figure 1-2: Comparison of the hexagonal mesoporous channel system of MCM-41 silica (left) and the three-dimensional channel system of MCM-48 silica (right).

The two different reaction pathways are caused by the alteration of the surfactant properties in water in the presence of different anions. In case of the hexadecyltrimethylammonium bromide (cetyltrimethylammonium bromide, CTAB) – the commonly used surfactant in the first syntheses – the bromide is exchanged for anionic silicate species during the synthesis. The fact that the mesostructures can be synthesized with surfactant concentrations far below the critical micelle concentration (cmc) shows the strong influence of the inorganic species [38,39].

An alternative synthesis for preparing mesoporous silicate was described in 1990 before the syntheses of the M41S phases were published [40]. This synthesis utilized the layered silicate kanemite, which consists of single layers of SiO_4 tetrahedra. The surfactants molecules are intercalated between the galleries of the layers („folded sheet" mechanism), hence transforming this material into the mesostructured FSM-16[*] material [41,42].

Originally, the M41S family has been classified into three subgroups: a hexagonal (MCM-41), a cubic (MCM-48) and a lamellar phase (MCM-50)[**]. In contrast to the hexagonal MCM-41 silica phase (space group: *P*6*m*) with its one-dimensional channel system, the cubic MCM-48 silica phase bears the advantage of a three-dimensional pore system as shown in Figure 1-2 (right).

The surface-defining MCM-48 silica is the gyroid or G-surface, forming a structure with the space group $Ia\bar{3}d$ [43-48], which is frequently observed in water-surfactant systems [49-51]. The structure contains a three-dimensional network with channels running along {111} and {100}, which provides large surface areas and a high accessibility of all sites within the porous network structure even if part of the pore entrances cannot be used due to blockage [52], which is of great advantage compared to the one-dimensional channel system of MCM-41 silica. The synthesis of the cubic MCM-48 silica phase is more difficult in comparison to the MCM-41 silica phase. This is the reason why only few groups have focused their efforts on this particular cubic phase and originally most of the interest has been concentrated almost exclusively on MCM-41 silica. Only little information was available on MCM-48 silica [53-55]. Recently, research groups have started to optimize the synthesis of the cubic phase [56-62] and it was even possible to obtain small MCM-48 single crystals [63].

Apart from the general problems in the synthesis of MCM-48 silica phases; there are only a few surfactants that can form this three-dimensional system [64]. Therefore, only little variations in the pore size diameter of the MCM-48 silica between 2 and 3 nm are available. In contrast, the pore size distribution of the MCM-41 silica phase can be "tuned" from 2 to 10 nm. The concept of the pore size tuning is to use surfactants with longer alkyl chains or to use so-called expanding molecules, e.g. mesitylene or alkanes, which "blow up" the hydrophobic core of the micelles in the MCM-41 silica synthesis. The use of expanding molecules does not work satisfactorily in case of the MCM-48 silica phase; it destroys the feasible balance between the inorganic and the organic compounds in the synthesis. The use of the alkyltrimethylammonium bromides is confined to alkyl chains with 14, 16 and 18 carbon atoms. An alkyl carbon chain of 20

---

[*] FSM stand for *F*olded *S*heet *M*esoporous Material.

[**] MCM stands for *M*obil *C*omposition of *M*atter.

atoms forms layered MCM-50 silica materials only [65]. This can be explained with the concept of the effective surfactant ion pair packing parameter $g = V/a_0{\cdot}l$, where V is the total volume of the surfactant chains plus any cosolvent organic molecules between the chains, a_0 is the effective head group area at the micelle surface, and l is the kinetic surfactant tail length or the curvature elastic energy [66,67]. This concept was designed for the description of surfactant organization in amphiphilic liquid-crystal arrays. Table 1-1 shows the expected mesophase sequence as a function of the packing parameter in classical micelle chemistry. The value of g increases when a_0 or l decrease or V increases. Since the increase in chain length of an alkyltrimethylammonium bromide changes V and l in the same magnitude it is supposed that a coiling of the hydrocarbon chain may be a reason for the observed increase of g for $C_nH_{2n+1}(CH_3)_3N^+$ surfactants with n > 18. The total volume of the hydrocarbon chain does not change significantly in contrast to the decrease of l due to coiling of the hydrocarbon chain [64]. The solution for this problem is the decrease of g by an increase of a_0.

Recently a synthesis with mixed surfactants was reported allowing the formation of MCM-41 silica phases with surfactant chain lengths n > 18 [68]. The surfactants used are alkyltriethylammonium bromides with alkyl chain lengths of up to 22 carbon atoms mixed with the corresponding alkyltrimethylammonium bromides. a_0 is increased significantly by the triethylammonium head group and the parameter g can be adjusted in the correct region only by adding the alkyltrimethylammonium bromide. The mixing of the two surfactants is illustrated in Figure 1-3 c.

Table 1-1: Expected mesophase sequence as a function of the packing parameter.

g	mesophase
$\frac{1}{3}$	cubic($Pm\bar{3}n$)
$\frac{1}{2}$	hexagonal ($p6m$)
$\frac{1}{2}-\frac{2}{3}$	cubic($Ia\bar{3}d$)
1	lamellar

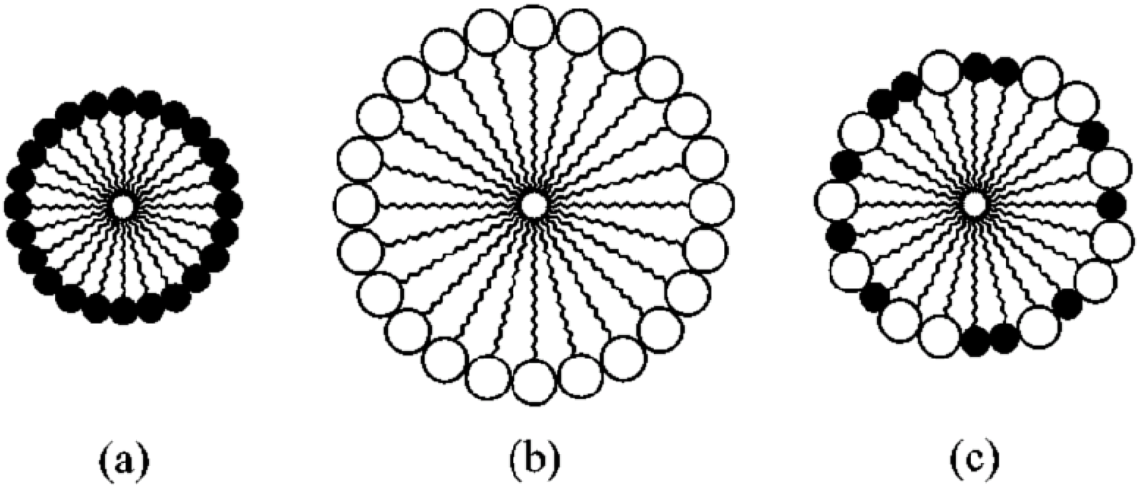

Figure 1-3: Schematic models for the cross section of surfactant micelles. (a) The small N^+Me_3 *head group is suitable for short alkyl tails, for the formation of the hexagonal* C_{12}*MCM-41 mesophase. (b) The large* N^+Et_3 *head group for* C_{22}*MCM-41. (c) The micelle packing in an intermediate case can be controlled with mixed surfactants [68].*

Initial reports on the formation of mesoporous MCM-48 silica with larger mesopores were due to a calculation error [69]. The commonly used theory for pore size calculation in the mesoporous regime is the Barret-Joyner-Halenda (BJH) procedure which is based on macroscopic thermodynamic models like the modified Kelvin equation [70] which underestimates the calculated pore diameter by ca. 1 nm [12]. This method leads to the upper border of 3 nm for the mesopores of MCM-48 silica materials. A new empirically corrected BJH method [71] was applied for the calculation of these “new” materials. The empirical correction is based on calibration using MCM-41 silica. Due to the different pore geometry of MCM-41 in comparison to MCM-48 silica this method should not be applied to the MCM-48 silica phase as it may introduce some systematic errors. The large pores of 3.8 nm diameter are below 3 nm if calculated by the original BJH theory. Recently the use of mixtures of cationic alkyltrimethylammonium surfactants (alkyl chain length from 12 to 20 carbon atoms) with neutral cosurfactants (polyoxyethylene alkyl ethers) lead to larger mesopores in MCM-48 silica materials [72,73]. Pore diameters up to 4.5 nm were calculated with the new empirical method [71]. The physisorption data and the X-ray diffraction data show that these materials have pore diameters above 3 nm although the mistakes due to that method are not known in detail.

Apart from syntheses with variable alkyltrimethylammonium bromide surfactant molecules, various other cationic surfactants can be used. Based on the electrostatic approach high-quality silica mesostructures were synthesized using cationic so-called

„gemini surfactants“, in which two quaternary ammonium head groups are separated by a methylene chain of variable length. Each head group is attached to a hydrophobic tail and the product obtained is denoted SBA-2. This mesophase consists of regular supercages that can be dimensionally tailored. It exhibits a three-dimensional hexagonal ($P6_3/mmc$) symmetry and a large specific surface area [74]. Recently, the silica mesophase SBA-8 was reported. It can be synthesized using so-called „bolaform surfactants“ at room temperature [75]. Bolaform amphiphiles are built of two hydrophilic moieties connected by a hydrophobic chain, but without hydrophobic tails. SBA-8 consists of a two-dimensional pore structure with a centered rectangular lattice (space group: *cmm*), which has no reported lyotropic liquid crystal analogue.

In addition to the interest in new mesoporous materials, several studies have been published within the last three years, which were devoted to new synthetic pathways in order to optimize the synthesis [76], to obtain single crystals [63], special morphologies [77,78], or bimodal pore systems [79], to investigate the formation mechanism [80] as well as to analyze the hydrothermal or mechanical stability of MCM-48 type of materials [81-83].

1.2 Application of mesoporous silica

1.2.1 Sorption materials

The M41S materials have been regarded as a suitable mesoporous model adsorbent for testing theoretical predictions of pore condensation and hysteresis [12,84,85], which are of great importance for the characterization of porous media by analysis of appropriate physisorption isotherms (nitrogen, argon and krypton physisorption at 77 K and 87 K). No materials with narrow pore size distributions in the lower mesoporous range were available before the discovery of the M41S materials. The state and thermodynamic stability of pure fluids in narrow pores depends on one hand on the relationship between the strength of fluid-wall and fluid-fluid interactions and the effects of confined pore space on the other. The physisorption behavior is dominated in micropores (pore width < 2 nm) almost entirely by the interactions between fluid molecules and the pore wall; pore filling phenomena occurring in mesopores (pore width: 2 – 50 nm) depend both on the attractive fluid-wall and fluid-fluid interactions, which may lead to pore condensation [86,87].

Pore condensation represents a first-order phase transition from a gas to a liquid-like state of the pore fluid occurring at a pressure p below the corresponding saturation pressure p_0 of the bulk fluid. In the classic Kelvin equation the occurrence of pore condensation, i.e. the shift of the gas-liquid phase transition of a confined fluid from bulk coexistence, is expressed in macroscopic quantities like the surface tension γ of the bulk fluid, the densities of the coexistent liquid ρ^l and gas ρ^g and the contact angle θ of the liquid meniscus against the pore wall. For cylindrical pores the Kelvin equation is given by

$$\ln\frac{p}{p_0} = \frac{-2\gamma\cos\theta}{k_b T\Delta\rho(R_p - t_c)} \qquad \textit{equation 1-1}$$

where $\Delta\rho = \rho^l - \rho^g$, T = experimental temperature, k_b = Boltzmann constant, R_p the pore radius and t_c the thickness of an adsorbed multilayer film at the onset of pore condensation, which is formed prior to pore condensation [87]. The stability of this multilayer film, which covers the pore walls in case of complete wetting, is determined by attractive fluid-wall interactions, surface tension, and curvature of the liquid-vapor interface. In the range of small film thickness the attractive fluid-wall interactions are dominant and multilayer adsorption occurs. However, when the adsorbed liquid-like film becomes thick, curvature effects become dominant. At a certain critical film thickness $t_c = R_p - R_k$, where R_k is the so-called core radius, pore condensation occurs, controlled by intermolecular forces in the core fluid. Hence, pore condensation does not occur in the entire pore but rather in the inner core.

Various models attempt to account for the multilayer (statistical) film thickness t_c by combining the Kelvin equation with a standard isotherm or a so-called t-curve, which usually refers to adsorption measurements on a non-porous solid. Taking into account the Frenkel-Halsey-Hill theory the film thickness t on flat substrates is expected to vary with p as [86] $\ln(p/p_0) = -\alpha t^{-m}$, where α is the fluid-wall interaction parameter. In case of non-retarded van-der-Waals fluid-wall interactions m has a theoretical value of 3. However, experimental values for m are often significantly lower than the theoretical value, even for strongly attractive adsorbents like graphite, i.e. m = 2.5 - 2.7 [86,87].

Pore condensation is often accompanied by hysteresis, i.e. capillary evaporation occurs at a lower relative pressure than capillary condensation. The details of physisorption hysteresis depend on the thermodynamic state of the pore fluid and on the texture of the adsorbent, i.e. the presence of a pore network. It is now widely accepted that there is a correlation between the shape of the hysteresis loop and the pore size distribution, geometry, and texture of the mesoporous adsorbent, although the detailed effects of these various factors on hysteresis are still not fully understood. An empirical classification of hysteresis loops is given by the IUPAC [3]. However, the mechanism and origin of physisorption hysteresis is still subject to discussion. Essentially, there are two models which contribute to the understanding of physisorption hysteresis [88,89]:

(i) *Independent (single) pore model*: Physisorption hysteresis is considered as an intrinsic property of the phase transition in a single, idealized pore, reflecting the existence of metastable gas states.
(ii) *Network model*: Physisorption hysteresis is due to network effects, which reflect the shape of the pores, the distribution of pore sizes and their connectivity in the porous medium.

The network model takes into account that in real materials the pores are interconnected and form a three-dimensional network [88-94]. Specific network models were developed in which adsorption and pore condensation can be fully described in terms of thermodynamics. Capillary evaporation is essentially understood as caused by connectivity and pore blocking effects, which may lead to a percolation process. This would result in a step-like desorption branch, i.e. type H2 hysteresis (IUPAC classification [3]) found for instance for the adsorption of fluids in porous vycor glass [89,95].

In contrast to the network model, theoretical approaches based on methods of statistical physics (e.g. density functional theory) support the picture that hysteresis may occur also in a single pore caused by the fact that the adsorption branch persists to the limit of metastability before jumping to the liquid branch [89,96]. In principle, metastability is thermodynamically feasible on either branch, but in practice it occurs only during the adsorption process as the nucleation of the liquid capillary phase may be delayed. Assuming a pore of finite length, vaporization during the desorption process can occur via a receding meniscus; nucleation and therefore metastability do not occur during capillary evaporation [97]. Hence, the jump from liquid to gas on desorption occurs more likely at thermodynamic equilibrium. The independent (single) pore model explaining hysteresis is important for physisorption isotherms exhibiting the hysteresis type H1, which was found to be characteristic of physisorption isotherms of fluids in MCM-41 silica materials [87], which consist of a one-dimensional channel system of cylindrical pores and in materials of well-defined pore shape and narrow pore size distribution like controlled-pore glasses (CPG) [98,99] or ordered xerogels [100].

In case of sufficiently wide mesopores the state of the pore fluid and the shift of the gas-liquid phase transition (pore condensation) from bulk coexistence can be expressed by classical approaches like the Kelvin equation in terms of macroscopic quantities. However, these macroscopic concepts do not account for the peculiarities of the critical region and cannot be applied to describe the state of the pore fluid in small mesopores anymore. Recently developed microscopic theories based on advances in statistical mechanics as for instance the density functional theory (NLDFT) [101,102], lattice model calculations [103], and various computer simulation studies [104-106] provide a detailed description of the structure of fluids confined to narrow pores on a molecular level and have therefore led to an improved understanding of the physisorption and phase behavior of fluids in micro- and mesopores.

These microscopic models suggest that a fluid in a pore can exist with two possible density profiles corresponding to inhomogeneous gas and liquid configurations in the pore. In this sense pore condensation is considered as a first order phase transition between an inhomogeneous gas configuration, which consists of vapor in the core region of the pore in equilibrium with a liquid-like adsorbed film, and a liquid configuration where the pore is completely filled with liquid. At the critical point of the confined fluid these two fluid configurations, hitherto distinct but with the same grand potential, become indistinguishable [102]. However, the locus of the critical point of the pore fluid is not identical with the bulk critical point. The critical temperature of the confined fluid is shifted to lower temperatures, i.e. in contrast to the predictions of the Kelvin equation pore condensation and physisorption hysteresis are not expected to persist up to the critical temperature T_c of the bulk fluid, but will vanish already at temperatures below T_c. The shift of the pore critical temperature is correlated with the pore width, i.e. the narrower the pore, the larger is the shift of the pore critical temperature to lower temperatures [102,107,108].

In addition to the shift in critical temperature, experiments and theory indicate that, as a result of the combined effects of fluid-wall forces and finite-size, the freezing temperature and triple point of the pore fluid may be also shifted to lower temperature relative to the bulk triple point as long as the wall-fluid attraction is not too strong, i.e. the pore walls do not prefer the solid phase [109-111]. In fact, recent theoretical and experimental studies led to the conclusion that the complete coexistence curve of the confined fluid is shifted to lower temperature and higher mean density [99,112,113]. Hence, the shape of the observed physisorption isotherms depends not only on the pore width, pore shape and texture of the porous material (as is reflected in the appropriate IUPAC classification of physisorption isotherms and hysteresis loops), but also on the thermodynamic state of the confined fluid. This is taken into account in the way that the thermodynamics of the pore fluid is determined by phenomena spanning the complete pore network [114]. Hysteresis is here associated with thermodynamic metastability of the low and high density phases of the pore fluid. Within this context one expects pore condensation and hysteresis to disappear already at temperatures which are still below the bulk critical temperature, but may be observed even at temperatures below the bulk triple point. This has to be taken into account for the characterization of porous media by the analysis of appropriate physisorption isotherms (e.g. nitrogen, argon, and krypton physisorption at 77 and 87 K). So far most systematic physisorption studies on model adsorbents like the M41S materials have focused on MCM-41 silica phases [115-124]. The occurrence of physisorption hysteresis of Type H1 (IUPAC Classification) in MCM-41 silica and aluminosilicate, which consist of a one-dimensional channel system, indicates that physisorption hysteresis can indeed be considered here as an intrinsic property of the pore fluid and thus supporting the single pore model of physisorption hysteresis. The MCM-41 and MCM-48 silica phases with their differences in structure are ideal for comparative studies for the influence of their pore systems on physisorption theory.

1.2.2 Nanostructured host/guest compounds and catalysis

In addition to the importance of the M41S materials as suitable mesoporous model adsorbents for testing theoretical predictions of pore condensation and hysteresis these materials have been also regarded as important materials for size- and shape-selective applications. Depending on the structure differences these phases are of different importance for various fields of material science, e.g. the linear arranged pores of the MCM-41 silica as host for laser dye molecules for the fabrication of a nanolaser [125]. Few attempts to introduce nanoparticles on the basis of iron(III) or Fe_2O_3 particles into M41S materials were limited to the hexagonal MCM-41 silica phase [126,127] and in none of these cases direct solid proof was given that the nanoparticles have been incorporated into the pore structure.

Recently the mesoporous MCM-48 silica phases were used as templates for the structuring of mesoporous carbon [128-130]. A filling of the mesopores was achieved by impregnation with carbon precursors, such as sucrose, followed by a carbonization process using sulfuric acid as catalyst. Removal of the MCM-48 silica template was achieved by hydrolysis of the silica in an aqueous solution of sodium hydroxide. The final product, designated as CMK-1*, exhibits both micropores and mesopores. By now two other routes have been developed employing modified MCM-48 silica phases as starting materials [131,132].

In comparison to the linear mesopores in the MCM-41 silica phases the three-dimensional pore structure of the mesoporous MCM-48 silica phase is very interesting as a matrix to immobilize catalytically active metal species [133]. *Table 1-2* summarizes the various reports with respect to the metal atoms located onto or within the silica walls of mesoporous MCM-48 silica phases; with respect to the synthesis procedures, e.g. direct synthesis (D), grafting of precursor species from the gas phase or wet impregnation (G).

In general, there are two different ways to introduce catalytic active sites into the mesoporous MCM-48 silica system [168]: (**i**) Addition of the metal ions to the synthesis gel of the MCM-48 silica phase prior to the hydrothermal treatment or (**ii**) post-synthetic incorporation. The disadvantage of the first method is a lower long-range order of the final material due to distortion of the liquid crystalline structure-directing agent by the metal ions during the synthesis.

The advantage of the post-synthetic treatment is the opportunity of starting with a highly ordered mesoporous material with a very high inner surface. There are two different ways for the post-synthetic treatment: Grafting of precursor species from the gas phase or wet impregnation. Gas phase introduction usually results in low loadings but without any affection of the porous host. The wet impregnation technique, however, allows higher degrees of loading but requires a very careful preparation, otherwise the host structure can be destroyed.

The main problem in all cases is the characterization of the products and particularly the chemical nature of the nanostructured guest compounds. To prove that most of the catalytic metal species are inside the porous host structure the combination of comprehensive characterization techniques, i.e. powder X-ray diffraction (P-XRD), high resolution transmission electron microscopy (HRTEM), selected area electron

---

[*] CMK stands for *C*arbons *m*esostructured by *K*AIST.

diffraction (SAED), energy dispersive spectroscopy (EDS), or nitrogen physisorption, is necessary. To characterize the metal species itself, techniques like IR-, UV/Vis-spectroscopy, thermogravimetry coupled with differential thermal analysis and mass spectroscopy (TG/DTA/MS), or X-ray absorption spectroscopy have to be applied.

Table 1-2: Synthesis approaches of MCM-48 silica phase with metal atoms located onto the silica surface or within the silica walls (D: direct synthesis; G: grafting).

metal	**synthesis method**	**authors [reference]**
Ag	G	Wang et al. [134]
Al	D	Schmidt et al. [135], Kosslick et al. [136], Romero et al. [137], Chen et al. [138], Schumacher et al. [139], Chang et al. [140]
B	D	Yuan et al. [141]
Cr	D	Zhang et al. [142], Kawi et al.[143]
Cu	D	Hartmann et al. [144,145], Reller et al. [17]
Fe	D, G	Echached et al. [146], Kosslick et al. [136], Köhn et al. [16], Fröba et al. [18]
Ga	D	Kosslick et al. [136]
Mn	D, G	Zhao et al. [147], Xu et al. [148]
Mo	G	Morey et al. [149], Ferreira et al. [150], Kang et al. [151]
Ti	D, G	Morey et al. [152,153],Zhang et al. [142], Koyano et al. [154], Walker et al. [155], Anpo et al. [156], Corma et al [60], Schumacher et al. [139], Ahn et al. [157], Kang et al. [151], Ferreira et al. [158], Pena et al. [159], Widenmeyer et al. [160], Schrijnemakers et al. [161]
V	D, G	Zhang et al. [142], Morey et al. [162], Schumacher et al. [139], Van Der Voort et al. [163-165], Kang et al. [151], Mathieu et al. [166], Pena et al. [167], Chang et al. [140]
Zn	D	Hartmann et al. [144]
Zr	D	Morey et al. [168], Kang et al. [151]

1.3 Aim of this work

The aim of this thesis was the synthesis and characterization of high quality mesoporous MCM-48 silica materials with respect to their capability to serve as new model adsorbents as well as host materials for transition metal/metal oxide guest species.

In order to obtain high quality mesoporous MCM-48 silica materials with various pore size distributions systematic studies with commercially available and newly synthesized surfactants had to be applied.

The wet impregnation technique in combination with calcination was chosen to prove the capability of the mesoporous MCM-48 silica materials to act as host for transition metal/metal oxides nanostructures.

In addition, comprehensive characterization techniques were to be applied in order to learn more about the structure of these new nanostructured materials as well as to gain better insight into their formation and their material properties, respectively.

Apart from the synthesis special attention is paid to the characterization of the mesoporous MCM-48 silica materials by physisorption methods and to compare these results to the behavior of other mesoporous silica materials as MCM-41 silica and controlled-pore glass (CPG).

2 Experimental

2.1 Synthesis of pristine mesoporous MCM-48 silica

The syntheses of the pristine MCM-48 silica materials were carried out by mixing reactants with the following relative molar composition: 1.0 tetraethylorthosilicate (TEOS) : 0.65 quaternary ammonium bromide surfactant : 0.5 KOH : 62 H_2O. For a pre-hydrolization of the TEOS the surfactant was added after ten minutes of vigorous stirring. Stirring was continued for additional 20 - 30 minutes to homogenize the synthesis mixture. The condensation of the silica was performed for 48 to 72 h in a Teflon-lined steel autoclave under hydrothermal conditions (388 K). The resultant white product was filtered off and washed several times with warm deionized water. After drying it was calcined at 773 - 823 K (heating ramp of 1 K/min) in air for 6 h in a programmable furnace of the company GERO, type F 40-500/1300C. The obtained pristine MCM-48 silica are of high quality and thermal stability up to 923 K in air if the samples are thoroughly dried. Total removal of structure-director by the calcination procedure was verified by FTIR exhibiting no corresponding C-C, C-H, C-N bands.

Depending on the desired pore size distribution of the material various cationic quaternary ammonium bromide surfactants were applied in the synthesis. Table 2-1 gives an overview of the used surfactants with abbreviations derived from the common abbreviation C_{16}TAB for hexadecyltrimethylammonium bromide. Most of the surfactants are not commercially available and were synthesized from the corresponding primary bromoalkanes and alkylamines in a nucleophilic substitution reaction [169]. Surfactants with more than 22 carbon atoms were not synthesized due to the expensive educts as no bromoalkanes with more than 22 carbon atoms are commercially available.

2.2 Synthesis of pristine mesoporous MCM-41 silica

The syntheses of the pristine MCM-41 silica materials [170] were carried out at 340 K by mixing reactants with the following molar composition: 1.0 silica (Cab-osil M-5) : 0.25 alkyltrimethylammonium bromide (C_nTAB) : 0.2 TMAOH : 35 H_2O. The mixture was stirred vigorously for at least one hour and the resultant gel

Table 2-1: Used cationic quaternary ammonium bromide surfactants for synthesis with their abbreviation and the product extension for the corresponding M41S phase.

Surfactant	abbreviation	supplier	M41S
dodecyltrimethylammonium bromide	C_{12}TAB	Fluka	**-**
tetradecyltrimethylammonium bromide	C_{14}TAB	Fluka	**A**
hexadecyltrimethylammonium bromide	C_{16}TAB	Merck	**B**
octadecyltrimethylammonium bromide	C_{18}TAB	Fluka	**C**
eicosanyltrimethylammonium bromide	C_{20}TAB	synthesized	-
eicosanylethyldimethylammonium bromide	C_{20}EDMAB	synthesized	**D**
eicosanyldiethylmethylammonium bromide	C_{20}DEMAB	synthesized	-
eicosanyltriethylammonium bromide	C_{20}TEAB	synthesized	-
docosanyltrimethylammonium bromide	C_{22}TAB	synthesized	-
docosanylethyldimethylammonium bromide	C_{22}EDMAB	synthesized	**E**
docosanyldiethylmethylammonium bromide	C_{22}DEMAB	synthesized	-
docosanyltriethylammonium bromide	C_{22}TEAB	synthesized	-

was transferred in a Teflon-lined steel autoclave. The autoclave was kept at 340 K for 24 hours and after a final hydrothermal treatment at 423 K for another 24 hours the white product was filtered off and washed several times with warm deionized water. After drying it was calcined at 823 K (heating ramp of 1 K/min) in air for 6 h in a programmable furnace of the company GERO, type F 40-500/1300C. The obtained pristine MCM-41 silica are of high quality and thermal stability up to 923 K in air if the samples are thoroughly dried. Total removal of structure-director by the calcination procedure was proved by FTIR exhibiting no corresponding C-C, C-H, C-N bands.

Variations in pore diameter were obtained by utilization of alkyltrimethylammonium bromides with variable chain lengths (C_{12} to C_{16}) given in Table 2-1.

2.3 Synthesis of transition metal oxides within mesoporous silica

The formation of the transition metal oxides Fe and Co onto the inner surface of MCM-48 and MCM-41 silica was carried out by the wet impregnation technique followed by thermal transformation (calcination). Metal nitrate solutions in various concentrations were used as precursors and in case of the ternary cobalt iron oxide system a mixture of the corresponding metal nitrates was deployed.

The impregnation was carried out by stirring the mesoporous material with the nitrate solution for at least 10 minutes. The solid was separated off in a centrifuge and dried first at room temperature in air. Final drying was achieved overnight in oil pump vacuum.

The calcination of the transition metal nitrate to the corresponding oxide was carried out in a programmable furnace of the company GERO, type F 40-500/1300C. The heating rate was set at 1 K per minute. A continuous air flow removed the volatile decomposition products from the solid. The waste-loaded gas was purged in a downstream gas washing system with NaOH and H_2SO_4 solutions.

2.3.1 Iron oxide

The loading of iron oxides onto the inner surface of MCM-48 silica was carried out by the wet impregnation technique in two different series; *Fe*-**8A** and *Fe*-**8B**. MCM-41 silica was also loaded with iron oxide in the series *Fe*-**1A**[*] by the wet impregnation method. Calcinations were carried out at 673 K for 6 h, which led to a transformation of the iron nitrate into an oxide indicated by the disappearance of the IR band of the NO_3^- ion at 1380 cm^{-1}.

The materials of the *Fe*-**8A** series were synthesized by stirring MCM-48 silica material with a 1.6 M aqueous solution of iron(III) nitrate ($Fe(NO_3)_3 \cdot 9H_2O$). The calcined product *Fe*-**8A-1** was impregnated and calcined once again to form the product *Fe*-**8A-2**. After the third impregnation/calcination cycles the product *Fe*-**8A-3** was formed.

The materials of the *Fe*-**8B** and the *Fe*-**1A** series were synthesized by stirring MCM-48 or MCM-41 silica materials with various concentrated aqueous solutions of

---

[*] *Fe* stands for the guest metal species; the porous host MCM-4**8** or MCM-4**1** is abbreviated to **8** and **1**; the following abbreviations distinguish the product of a synthesis series.

Table 2-2: Sample codes for the iron oxide loaded MCM-48 and MCM-41silica materials corresponding to the concentration of iron(III) nitrate solution used for their preparation.

Concentration [mol/l]	MCM-48 sample code	MCM-41 sample code
0.07	*Fe*-**8B-1**	*Fe*-**1A-1**
0.37	*Fe*-**8B-2**	*Fe*-**1A-2**
1.18	*Fe*-**8B-3**	*Fe*-**1A-3**
4.87	*Fe*-**8B-4**	*Fe*-**1A-4**

iron(III) nitrate ($Fe(NO_3)_3 \cdot 9H_2O$). Table 2-2 shows the sample codes for both series with respect to the utilized concentration of iron(III) nitrate solution.

In order to verify that haematite (α-Fe_2O_3) was formed exclusively under these experimental conditions, pristine iron(III) nitrate was treated in the same way and the brown powder obtained was identified as α-Fe_2O_3 by powder X-ray diffraction. This material was used as a reference compound for various characterization techniques. It should be noted that the pristine MCM-48 silica materials used for the impregnation for the *Fe*-**8A** and *Fe*-**8B** series were from different batches. Another material, designated as **B_1-Fe_2O_3**, was synthesized especially for physisorption experiments by the same procedure as *Fe*-**8A-1**.

2.3.2 Cobalt iron oxide

Wet impregnation technique was used to introduce cobalt iron oxide into the mesoporous MCM-48 molecular sieve. A 1.6 M mixed aqueous solution of cobalt(II) nitrate and iron(III) nitrate was applied with $Co(NO_3)_2 \cdot 6H_2O$ and iron(III) nitrate $Fe(NO_3)_3 \cdot 9H_2O$ with a ratio of 1 Co : 2 Fe. After impregnation the material was calcined at 848 K for 6 hours, followed by a calcination at 873 K for 72 hours (*product* *$CoFe_2$*-**8A-1**) or at 923 K for 72 hours (product *$CoFe_2$*-**8A-2**), respectively.

The reference material, $CoFe_2O_4$, was obtained by calcination of a mixture of cobalt(II) nitrate and iron(III) nitrate with the same ratio as above (1 Co : 2 Fe). The calcination was carried out at 650° C for 72 hours. Phase purity was controlled by powder X-ray diffraction.

2.3.3 Cobalt oxide

The loading of cobalt oxides onto the inner surface of MCM-48 silica was carried out with a 0.8 M (*Co*-**8A-1**) and a 1.6 M (*Co*-**8A-2**) aqueous solution of cobalt(II) nitrate ($Fe(NO_3)_2 \cdot 6H_2O$). The thermal transformation to the corresponding oxide was carried out at 673 K for 6 h. The disappearance of the IR band of the NO_3^- ion at 1380 cm^{-1} proved the total conversion to the oxide.

The *Co*-**8A-2** sample was reduced in a CHEMBET-3000 (see section 2.4.5) with a mixture of hydrogen in nitrogen (33% : 67%) with a heating rate of 5 K per minute and a maximum temperature of 873 K. The maximum temperature was kept until the reduction was finished.

2.4 Characterization

2.4.1 Powder X-ray diffraction

Powder X-ray diffraction (P-XRD) patterns were recorded with a Bruker/AXS D8 advance diffractometer using filtered Cu-K_α radiation in θ/θ geometry. The diffractometer was equipped with variable slits on the tube and detector side and a secondary monochromator. The data were taken in a step scan mode with $\Delta 2\theta = 0.02°$ and a counting time of 1 s per step as standard configuration.

2.4.2 Physisorption measurements

Specific surface areas and pore diameters were determined by nitrogen adsorption/ desorption measurements. Nitrogen (purity 99.999 vol%), argon (purity 99.999 vol%) and krypton (purity 99.996 vol%) supplied by Messer Griesheim GmbH were used as adsorptives. Physisorption isotherms of nitrogen, argon and krypton at 77 K (i.e. 77.35 K) and 87 K (i.e. 87.27 K) in different MCM-48 silica materials with mean pore diameters 2-3 nm were determined in a pressure range from $p/p_0 = 5$ to 1 using a static volumetric technique (QUANTACHROME AUTOSORB). In order to also investigate the existence of micropores in the material argon physisorption isotherms at 87 K in the range $p/p_0 = 1 \cdot 10^{-5}$ up to 1 were measured. The analysis station of the volumetric apparatus was equipped - in addition to the pressure transducers in the dosing volume of the apparatus - with high precision pressure transducers (MKS Baratron) dedicated to read the pressure only in the sample cell from which adsorbed gas volumes are computed. Hence, the sample cell was isolated during equilibration, which ensured a very small effective void volume and therefore a highly accurate determination of the adsorbed amount. The saturation pressure p_0 was measured throughout the entire analysis by means of a dedicated saturation pressure transducer which allowed the vapor pressure to be monitored for each data point recorded. Before each physisorption measurement the sample was outgassed at 393.15 K for 12 h under turbomolecularpump vacuum.

The surface areas were calculated applying the theoretic equation of Brunauer, Emmet and Teller (BET) [171] for the relative pressures between 0.05 and 0.15 - 0.23, depending on the number of data points that were appropriate for a linear fit. The pore size distributions were calculated by Barrett-Joyner-Halenda (BJH) formula [70] using the desorption branch of the nitrogen physisorption isotherms. Non-local density functional theory (NLDFT) was applied for Nitrogen (77 K) and Argon (87 K) measurements for the relative pressure range from 0.001 to 0.7. All calculations were achieved with the AUTOSORB 1 software for windows 1.24 (June 14.2001).

2.4.3 X-ray absorption spectroscopy (XAS[*])

X-ray absorption spectroscopic measurements were carried out at the storage ring DORIS III (HASYLAB@DESY, Hamburg, Germany) at the EXAFS II beam line, which was equipped with a Si (111) double-crystal monochromator. The Fe K- and Co K-edge spectra were recorded at a temperature of 20 K, 77 K or 300 K in transmission mode depending on the available setup at the synchrotron source. Each spectrum was calibrated against the first inflection point of the corresponding K edge of a reference metal foil, which was measured simultaneously. Freshly prepared corresponding metal oxides were used as reference for the guest compounds. All samples were measured as pressed polyethylene pellets in which the transition metal content was adjusted to give an absorption jump $\Delta\mu d = 0.4 - 0.9$. For further data analyses WinXAS software [172]

---

[*] In modern nomenclature the abbreviation XAFS will be used, too. XAFS represents the combination of the two regions of the absorption spectrum: **XA**NES (*X*-ray *A*bsorption *N*ear-*E*dge *S*tructure) and EXA**FS** (*E*xtended *X*-ray *A*bsorption *F*ine *S*tructure).

was used. Theoretical calculations of the phase shifts and backscattering amplitudes were calculated using FEFF6.01 software [173].

2.4.4 Transmission electron microscopy

For electron microscopic measurements the powders were crushed in ethanol, and the ground material was dispersed on a holey carbon grid. The electron diffraction and HRTEM studies were carried out using a Philips CM20 electron microscope operating at 200 kV with a very low illumination to avoid destruction of the material by the electron beam. The EDS analyses were performed using a Link QX 20 analytical system.

2.4.5 Temperature programmed reduction

Temperature programmed reduction (TPR) was carried out in a QUANTACHROME CHEMBET-3000 with 35% hydrogen in 65% nitrogen. The CHEMBET is equipped with thermal conductivity detectors for signal detection before and after the sample cell. Various gas mixtures are applicable by an external gas mixing system (QUANTACHROME Linear Mass Flow Controller).

2.4.6 Magnetic measurements

The measurements of the dc-magnetization as a function of the applied field and the susceptibility as a function of temperature were performed on a commercial SQUID[*] magnetometer (Quantum Design).

---

[*] SQUID: *S*uperconducting *Qu*antum *I*nterference *D*evice

3 Mesoporous silica

3.1 Powder X-ray diffraction

Powder X-ray diffraction is one of the main characterization methods for mesoporous materials of the M41S type. The as-synthesized mesostructured material as well as the calcined mesoporous M41S material can be investigated. Figure 3-1 shows typical P-XRD patterns of high-quality mesostructured MCM-41 and MCM-48 silica materials. The diffraction peaks above 2 $\theta = 3°$ represent the very good long-range order of the materials. Figure 3-2 shows the corresponding P-XRD patterns of the calcined mesostructures. Both mesostructured MCM-41 and MCM-48 silica shown in Figure 3-1

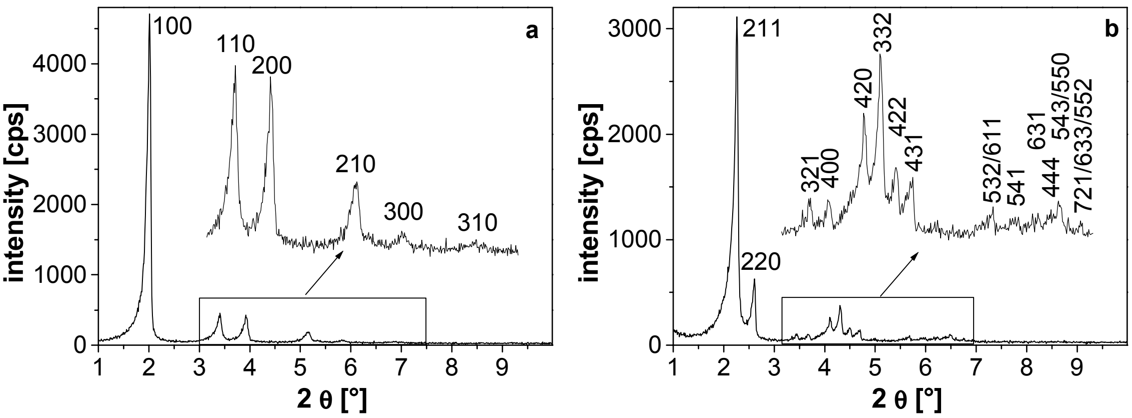

Figure 3-1: P-XRD patterns of (a) MCM-41 and (b) MCM-48 silica materials as synthesized.

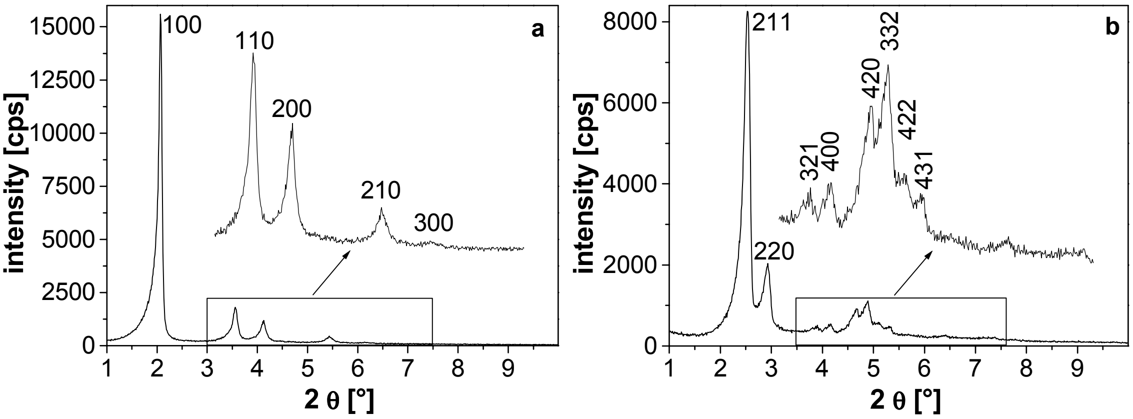

Figure 3-2: P-XRD patterns of calcined (a) MCM-41 and (b) MCM-48 silica materials.

Table 3-1: Miller indices hkl, 2 θ_{hkl}, d_{hkl} values, and calculated unit cell parameter a of the first peak in the diffraction pattern of the as-synthesized (as) and calcined MCM-41 and MCM-48 silica phases shown in Figure 3-1 and Figure 3-2.

sample	hkl	2 θ_{hkl} [°]	d_{hkl} [nm]	a [nm]
MCM-41 as	100	2.01	4.88	5.63
MCM-41	100	2.07	4.74	5.47
MCM-48 as	211	2.26	4.34	10.63
MCM-48	211	2.53	3.88	9.50

and Figure 3-2 were synthesized with cetyltrimethylammonium bromide ($C_{16}TAB$). The main differences between the P-XRD patterns of the as-synthesized materials and the calcined mesoporous silica are a higher intensity and a shift of the peaks to higher 2 θ degrees for the calcined materials.

The intensity is raised by the calcination due to the removal of the structure-directing agent. This effect will be discussed in Chapter 5.1.1.1 in more detail. The shift of the peaks is due to a shrinkage of the unit cell by the calcination procedure. The calcination at elevated temperature leads to a further condensation of silanol groups within the walls of the silica and therefore to the reduction of the unit cell size. This effect can be seen in all parameters given in Table 3-1. The 2 θ value increases from both as-synthesized samples to the corresponding calcined phases. This leads to a decrease of the *d* values calculated by Bragg's law and also gives a decrease in the calculated unit cell parameter *a*[*]. The decrease of the hexagonal MCM-41 silica phase is not as drastic as the shrinkage of the unit cell of the MCM-48 silica phase of more than ten percent. This can be attributed to the more sensitive structure of the MCM-48 silica material.

Besides the synthesis with the $C_{16}TAB$, other surfactant molecules were applied to the synthesis of mesoporous MCM-41 and MCM-48 silica phases as mentioned in Chapters 2.1 and 2.2. The synthesis of the mesoporous MCM-41 silica material was also successful with the $C_{12}TAB$ and $C_{14}TAB$. Figure 3-3 compares the three mesoporous MCM-41 silica phases MCM-41**A** ($C_{12}TAB$), MCM-41**B** ($C_{14}TAB$), and

---

[*] MCM-41: $a = \frac{2}{3}\sqrt{3} \cdot d_{100}$; MCM-48: $a = \sqrt{6} \cdot d_{211}$.

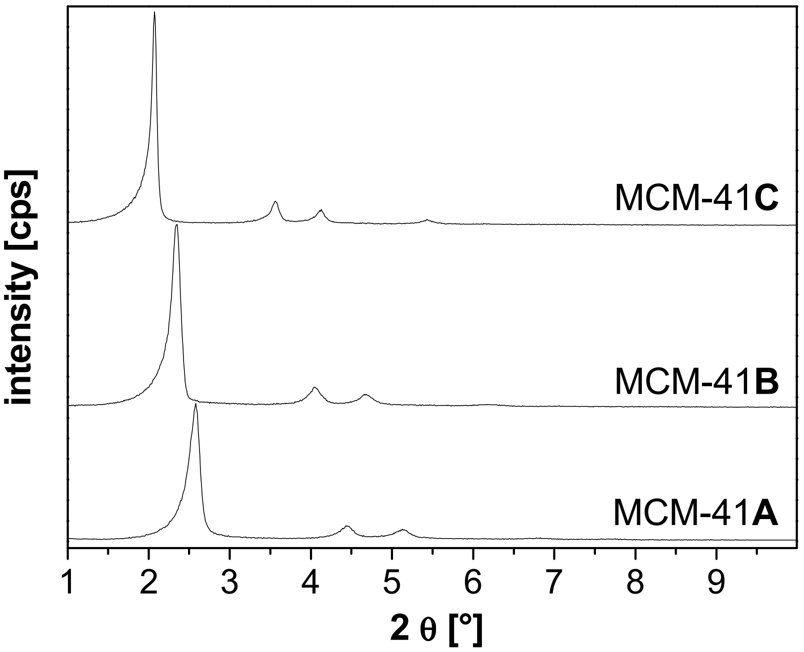

*Figure 3-3: P-XRD patterns of calcined MCM-41 silica **A**, **B**, and **C** synthesized with $C_{12}TAB$, $C_{14}TAB$, and $C_{16}TAB$.*

MCM-41**C** ($C_{16}TAB$) to show the reduction in the unit cell due to the utilization of different chain lengths in the synthesis. The reduction in the unit cell ranges from $a = 5.47$ nm for the MCM-41**C** over $a = 4.82$ nm for the MCM-41**B** to $a = 4.39$ nm for the MCM-41**A** silica phase.

MCM-48 silica phases were synthesized with the commercially available surfactants $C_{14}TAB$, $C_{16}TAB$, and $C_{18}TAB$, denoted as MCM-48**A**, MCM-48**B**, and MCM-48**C**, shown in Figure 3-4. For the synthesis of MCM-48 silica with larger pore diameters various surfactants have been synthesized (given in Table 2-1, page 16). Initially only the trimethylammonium bromide head group was used for the first synthetic attempts based on the concept of the effective surfactant packing parameter g (see Chapter 1.1). The only products obtained from these surfactants were lamellar mesostructures even if the surfactant concentration was decreased over a wide range (from 0.65 mol surfactant per SiO_2 to 0.3 mol). This problem was solved with the increase of the head group to ethyldimethylammonium bromide, diethylmethylammonium bromide or triethylammonium bromide. While the larger head group surfactants gave only hexagonal or unstructured materials the $C_{20}EDMAB$ and $C_{22}EDMAB$ lead to cubic mesostructures, depicted as MCM-48**D** and MCM-48**E**. Figure 3-4 clearly shows the almost linear increase of the unit cell due to the longer chain length. The P-XRD data

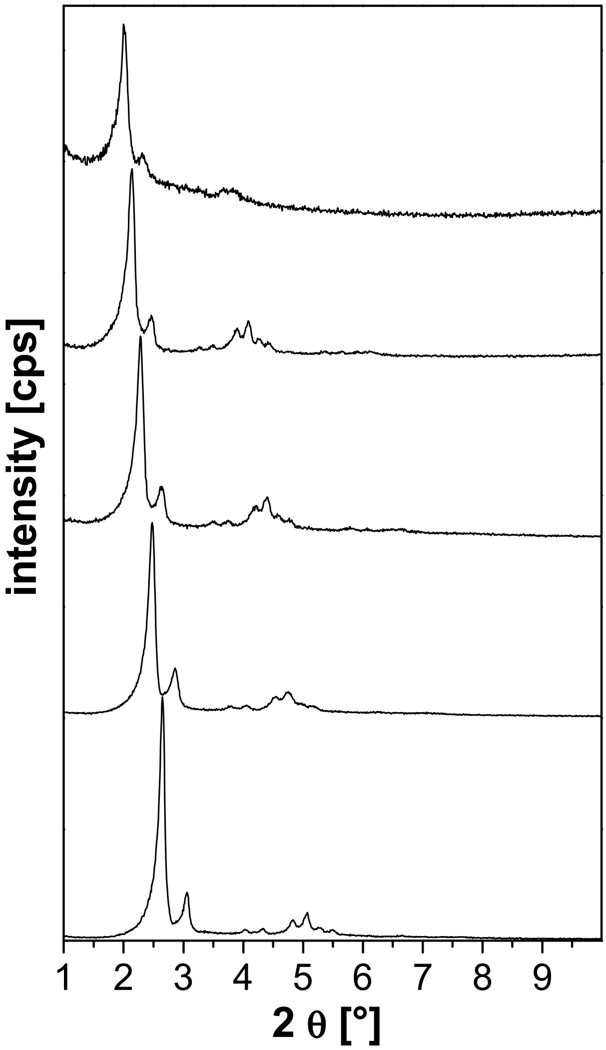

sample (surfactant)	2 θ_{211} [°]	d_{211} [nm]	a [nm]
MCM-48**E** (C_{22}DMEAB)	2.00	4.90	12.0
MCM-48**D** (C_{20}DMEAB)	2.14	4.58	11.2
MCM-48**C** (C_{18}TAB)	2.28	4.30	10.5
MCM-48**B** (C_{16}TAB)	2.48	3.95	9.69
MCM-48**A** (C_{14}TAB)	2.65	3.70	9.07

*Figure 3-4: P-XRD patterns of calcined MCM-48A, **B**, **C**, **D**, and **E** with the corresponding 2 θ_{211}, d_{211} values, and the unit cell parameter a as calculated from the 211 reflection.*

diagrams have been normalized for better comparison. They show perfect mesostructures for the MCM-48**A** to **D** series but a certain lack of long-range order in the case of the MCM-48**E**. A further discussion on the dependence of the unit cell parameter and the pore diameter will be made in Chapter 3.2

Only the standard synthesis procedure was applied to these larger head group surfactants and not the entire synthesis field diagram was investigated. This is due to the expensive educts and the long synthesis times of these special surfactants. Surfactants with longer chains were not synthesized as alkyl bromides longer than docosyl bromide are not commercially available.

The idea to synthesize these new surfactants is illustrated in Figure 3-5. Based on the assumption that a curved micellar structure is only stable if the head groups are in contact with each other and the cores provide enough space to accommodate the carbon chains it is supposed that the lamellar phase is build even at lowest concentrations (Figure 3-5**B**) if the chains are very long. Formation of the curved structure is not possible due to the long chains which leads to a unfilled space between the head groups. This allows to much movement of the head groups as depicted in Figure 3-5**A**. This problem is solved by a change of the head group for a larger one (Figure 3-5**C**), e.g. by replacing one methyl group by an ethyl group.

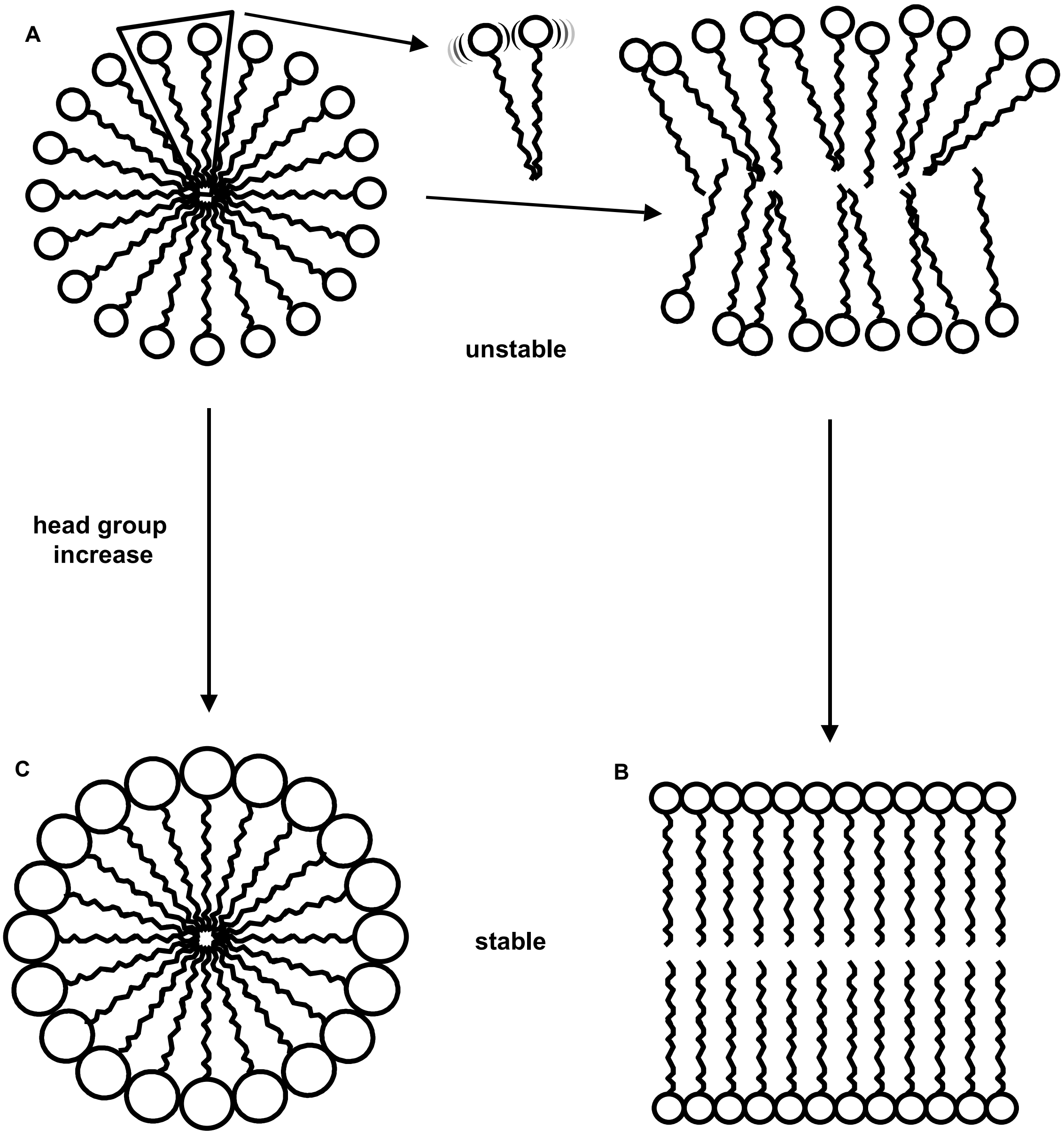

Figure 3-5: Illustration of the effect of head group increase in case of long chain surfactants. ***A*** *is unstable as the head groups have no contact and their movement changes the structure to the stable lamellar structure* ***B****. The stable situation* ***C*** *can be achieve by an increase of the surfactant head groups.*

3.2 Nitrogen physisorption

Together with the powder X-ray diffraction the physisorption method is the most powerful tool for the investigation of the pore system of the mesoporous materials. This method can be applied with different gases as adsorptive; nitrogen, argon, krypton, carbon dioxide, and even alkyl and aromatic hydrocarbons have been used. The BET [171] theory is commonly used for the standard evaluation of surface area and the BJH [70] method is applied for the calculation of pore diameter distributions. Recently developed approaches for the pore size determination are still under discussion as their advances in comparison to the BJH are still not explored in total (see Chapter 1.2.1). An extensive discussion of the different methods for the pore size calculation will be given in Chapter 4. The discussion of the surface and pore characteristics in this chapter will focus only on a brief comparison of the materials introduced in the previous chapter.

Figure 3-6 shows the nitrogen adsorption/desorption data for the samples MCM-41**A**, MCM-41**B**, and MCM-41**C** on the left and the corresponding pore diameter distributions calculated by the BJH method on the right. A comparable shift as expected form the P-XRD patterns can be observed in both diagrams. The specific surface A_S and the mean pore diameter D_p calculated at the maximum of the pore diameter distribution

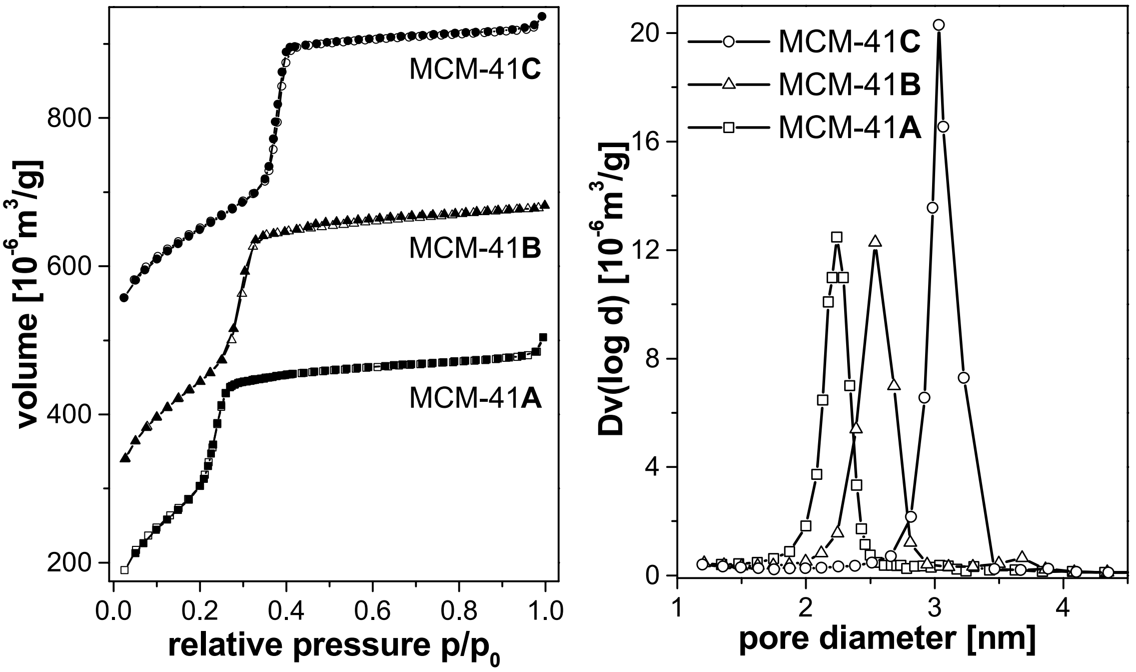

*Figure 3-6: Nitrogen physisorption data (77 K) of MCM-41 silica materials **A**,**B**, and **C** (left) and corresponding pore diameter distributions calculated by BJH (right); open symbols present adsorption and closed desorption; an offset of 150 and 350 $10^{-6}m^3/g$ was added to the volumes of MCM-41**B** and **C** for graphical presentation (left).*

*Table 3-2: d_{100} values, calculated unit cell parameter a, and pore characterization by nitrogen physisorption data (77 K) for MCM-41 silica **A**, **B**, and **C**.*

sample	**d_{100} [nm]**	**a [nm]**	**A_s(BET) [m^2/g]**	**D_p,N_2(BJH) [nm]**	**D_p,N_2(NLDFT) [nm]**	**t_{pw} [nm]**
MCM-41**A**	3.80	4.39	1086	2.24	3.31	1.08
MCM-41**B**	4.17	4.82	1074	2.55	3.66	1.16
MCM-41**C**	4.74	5.47	902	3.03	4.25	1.22

A_s(BET): BET specific surface area; D_p(BJH): BJH mode pore diameter, D_p(NLDFT): NLDFT mode pore diameter; t_{pw}: pore wall thickness calculated by $t_{pw} = a - D_p,N_2$(NLDFT).

are compared to the *d* values and the unit cell parameter *a* in Table 3-2. In case of the MCM-41 silica the pore wall thickness t_{pw} is the difference of *a* and the pore diameter. For this calculation the pore diameters should be as exact as possible; therefore, the NLDFT calculated diameters which are given too in Table 3-2 were applied. The pore wall thickness t_{pw} slightly increases with increasing pore diameter. It should be noted at this point that the determination of the unit cell parameter *a* is not perfect with measurements on a standard powder X-ray diffractometer. Due to the very small angles there is a tailing in the peaks as can be seen in Figure 3-3. This tailing leads to slight errors in the 2 θ evaluation and the *d* spacing. However, since the tailing is an intrinsic problem it may be neglected as long as the data are not regarded as absolute values; they can be used for comparative investigations.

Figure 3-7 shows the nitrogen adsorption/desorption data for the samples MCM-48**A** to **E** on the left and the corresponding pore diameter distributions calculated by the BJH method on the right. A comparable shift as expected from P-XRD patterns can be observed in both diagrams. In Table 3-3 the surface area A_S and the mean pore diameter D_p calculated at the maximum of the pore diameter distribution are compared to the *d* values and the unit cell parameter *a*. The calculation of the pore wall thickness for the mesoporous MCM-48 silica phase is not as straightforward as in the case of the MCM-41 silica material. The applied method is based on the following equation [47]:

$$a/\xi_0 = t_{pw} + D_h/2 \qquad \textit{equation 3-1}$$

where *a* is the unit cell and D_h the hydraulic pore diameter which can be calculated as

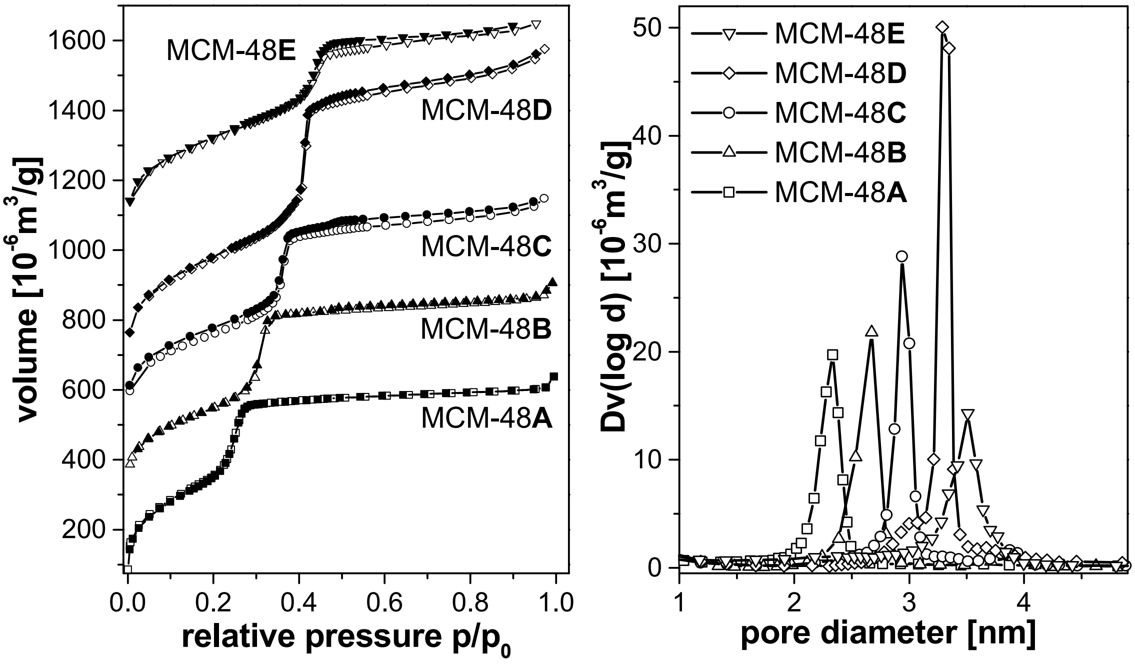

*Figure 3-7: Nitrogen physisorption data (77 K) of MCM-48 silica materials **A**, **B**, **C**, **D**, and **E** (left) and corresponding pore diameter distributions calculated by BJH (right); open symbols present adsorption and closed desorption; an offset of 150, 450, 700, and 1000 $10^{-6}m^3/g$ was added to the volumes of MCM-48**B**, **C**, **D**, and **E** for graphical presentation (left).*

*Table 3-3: d values, calculated unit cell parameter a, and pore characterization by nitrogen physisorption data (77 K) for MCM-48 silica **A**, **B**, **C**, **D**, and **E**.*

sample	**d_{211} [nm]**	**a [nm]**	**A_s(BET) [m^2/g]**	**D_p,N_2(BJH) [nm]**	**D_p,N_2(NLDFT) [nm]**	**t_{pw} [nm]**
MCM-48**A**	3.70	9.07	1282	2.31	3.42	1.22
MCM-48**B**	3.95	9.69	1104	2.64	3.80	1.23
MCM-48**C**	4.30	10.5	1129	2.96	4.18	1.31
MCM-48**D**	4.58	11.2	1379	3.31	4.57	1.34
MCM-48**E**	4.90	12.0	1172	3.49	4.82	1.47

A_s(BET): BET specific surface area; D_p(BJH): BJH mode pore diameter, D_p(NLDFT): NLDFT mode pore diameter; t_{pw}: pore wall thickness calculated by equation 3-1 with $D_h = D_p$,N_2(NLDFT).

mean pore diameter by the NLDFT theory [47]. ξ_0 is the reduced area per crystallographic unit cell. For the bicontinuous structure of the MCM-48 silica centered on the gyroid minimal surface [45,52] the reduced area is $\xi_0 = 3.092$ [174]. The advantage of the determination of the pore wall thickness t_{pw} based on equation 3-1 is that it does not depend on any absolute quantity per unit weight, which would be inaccurate due to impurities or inaccuracies in the weight determination.

In comparison to the MCM-41 silica phases the pore wall thickness of the MCM-48 silica materials is slightly larger and the pore wall thickness of the MCM-48 silica slightly increases with increasing pore width. Figure 3-8 depicts the change of the mean pore diameter calculated by the NLDFT theory depending on the carbon chain length of the used surfactant. The linear fit over all data points A gives a slope of 0.18 nm and a y-intercept of 0.95 nm. But due to the fact that the y-intercept corresponds to the volume that the head group occupies during the synthesis only points with the same head group can be used for such a calculation. The linear fit over all points B obtained by the trimethylammonium head group gives a slope of 0.19 nm and a y-intercept of 0.76 nm for all points. A comparison of the two y-intercepts shows the increase of the surfactant head group from the trimethylammonium to the ethyldimethylammonium head group of more than 0.2 nm or 20%. The real surfactant head group increase in the case of the change of one methyl to an ethyl group may be even larger, but is not detectable at the moment as no MCM-48 silica can be synthesized with a surfactant

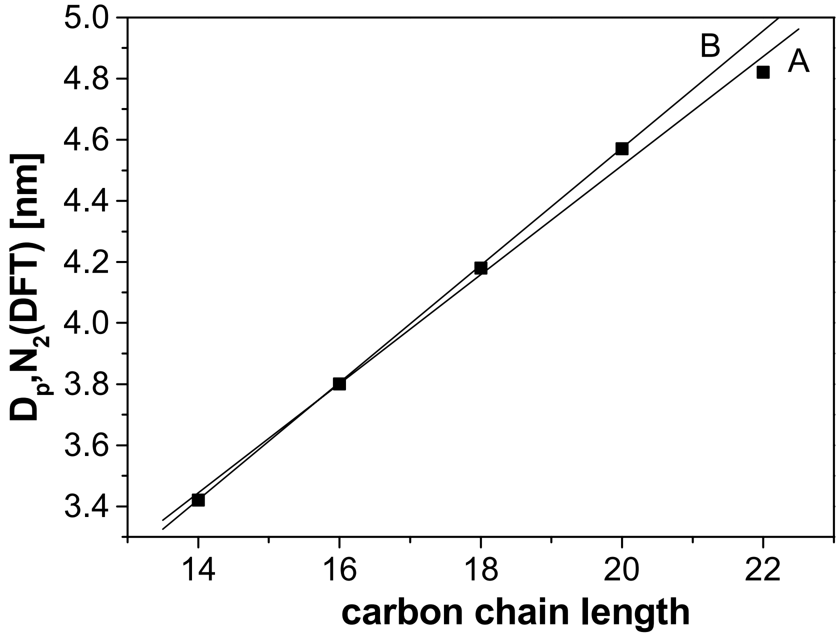

Figure 3-8: Change of pore diameter with increasing surfactant chain length for the MCM-48 silica phases with two linear fits: A for all points and B for the chain lengths of 14 to 18.

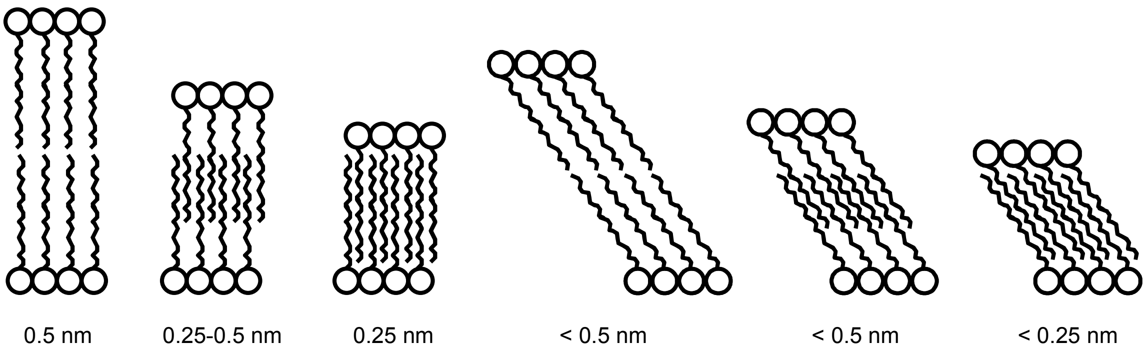

Figure 3-9: Illustration of some possible configurations of surfactant molecules in lamellar micelles and presumed changes in the double layer thickness of the configurations in case of a prolongation of the carbon chain by two carbons.

longer than 22 carbon atoms (see Chapter 2.1, page 15). Therefore, only two points are available for a linear fit which is mathematical insufficient.

Due to the linear increase of the pore size it can be assumed that the mechanism for the formation of the MCM-48 silica is the same for all applied surfactants. The change of the pore diameter with increasing chain length is not as significant as might be expected from geometric aspects. Two additional carbon atoms lead to an increase in the chain length of 0.25 nm and if a cylindrical micelle structure is assumed the total increase in the pore diameter should be 0.5 nm. The reason for the smaller increase may be an overlapping or a non-perpendicular arrangement for the surfactants as illustrated in Figure 3-9. In addition, an ordering of the chains as all "cis" can not be assumed. Some "trans" configurations are possible in the chains as it was reported for natural lamellar micellar structures.

At this point it should be mentioned that, apart from the utilization of different surfactants, the pore diameter can be controlled by other parameters within a smaller range. With longer hydrothermal treatments or higher/lower calcination temperature it is possible to change the pore diameter within +/- 10%. In the following chapters some of the materials were synthesized with slight differences, as compared to the materials described above. As the general route is the same they are named by the system as introduced above with **A**, **B**, **C**, **D**, and **E** due to the used surfactant during the synthesis. In some cases the materials will be further indexed to show that they are different from the ones discussed above; usually the differences are limited to pore diameter, specific surface, and unit cell parameter. The general features, such as high porosity, good long-range order, and symmetry, are maintained.

3.3 Transmission electron microscopy

Transmission electron microscopy (TEM) is another method to prove the preservation of the mesoporous structure of the MCM-48 silica after calcination. Three electron diffraction patterns of the same crystallite (the ⟨100⟩, ⟨111⟩, and ⟨110⟩ section) are presented in Figure 3-10. Together with other patterns, they allow reciprocal space to be reconstructed and the determination of the cubic I-centered Bravais lattice with the following reflection conditions: hkl, $h + k + l = 2n$; hhl, $2h + l = 4$n; and $0kl$, $k = 2$n. These reflection conditions are only compatible with the $I4_1/a\bar{3}2/d$ space group (no. 230), which is in agreement with previous results [43-48]. The {200} and {110} reflections, respectively, present in the ⟨100⟩ (Figure 3-10a) and the ⟨111⟩ zone axis pattern (Figure 3-10b), are forbidden reflections which appear due to multiple diffraction; therefore these reflections do not appear on the ⟨110⟩ zone axis pattern (Figure 3-10c). These electron diffraction patterns, which were taken with a very large camera length, allow the lattice parameter to be estimated as a = 8.0 ± 0.1 nm; a value which is slightly smaller than the one determined from XRD data (see Table 3-1).

Modern electron microscopy allows resolution even below the 0.2-nm level. Because of the large lattice parameters of MCM-48 silica, high-resolution images can, in principle, be obtained along almost all zone axes. However, the limiting factor for resolution here is no longer the interatomic distance, but the stability of the sample under high voltage illumination. The present images were obtained under low dose conditions with direct magnifications not exceeding 10^5. The most informative images, corresponding to the ⟨100⟩, ⟨111⟩, and ⟨110⟩ zone axes are presented in Figure 3-11.

The images reveal the pore architecture of the material and are characteristic of this kind of material [43]. The crystals are remarkably perfect, and no one- or two-dimensional crystal defect has been detected. The microanalysis results show the

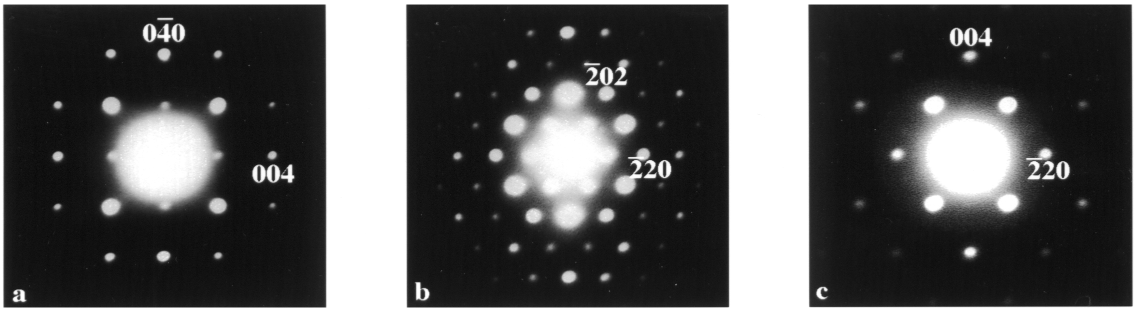

Figure 3-10: Selected area electron diffraction patterns (SAED) of pristine MCM-48 silica material: (a) ⟨100⟩, (b) ⟨111⟩, and (c) ⟨110⟩ zone axis patterns.

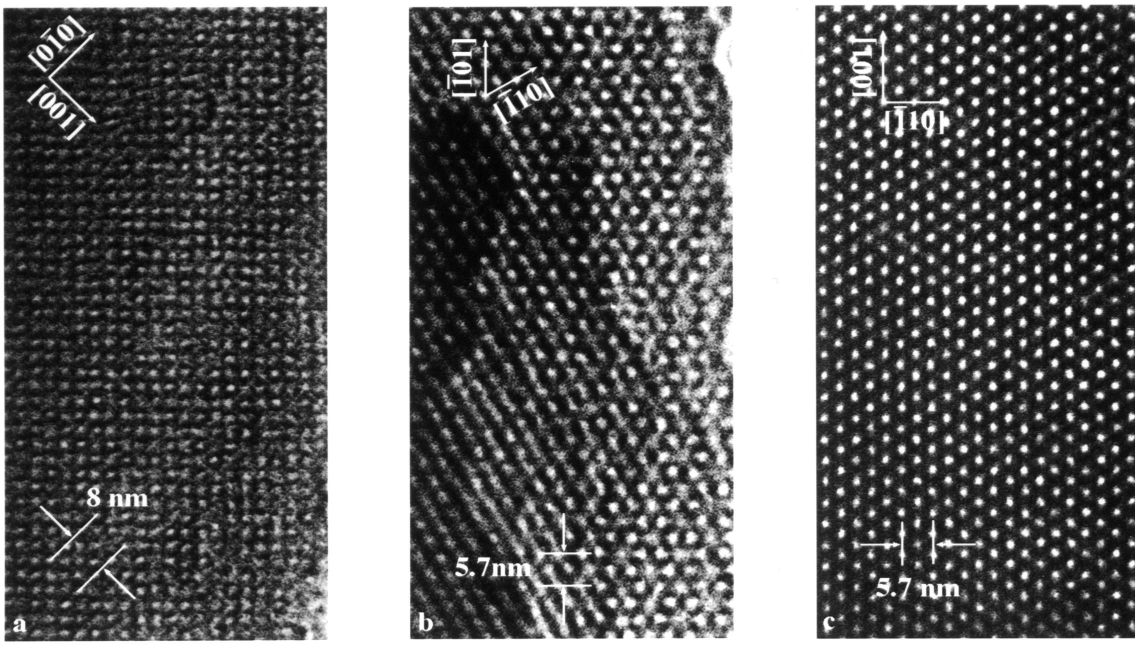

Figure 3-11: HRTEM images of pristine MCM-48 silica material corresponding to the (a) ⟨100⟩, (b) ⟨111⟩, and (c) ⟨110⟩ zone axis.

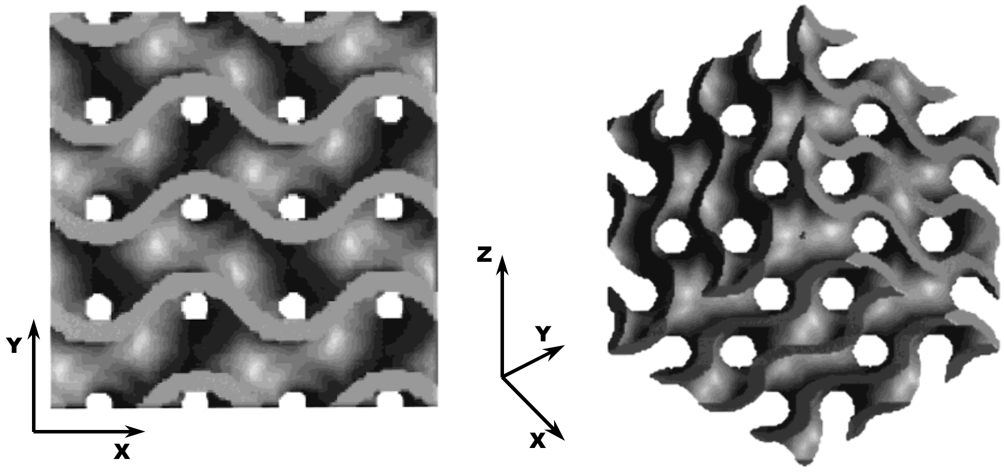

Figure 3-12: Calculated view for MCM-48 silica material corresponding to the ⟨100⟩ (left) and the ⟨111⟩ (right) zone axis [175].

presence of mainly Si, O, and C. The latter element may be intrinsic to the specimen itself, but certainly there is a contribution from the carbon grid and from the contamination which occurs during the recording of the analysis spectrum. In some grains, traces of Cl have been observed.

It must be mentioned that the cubic system shows a cubic arrangement of the reflections only if the view is taken along the ⟨100⟩ zone axis. Figure 3-12 shows this calculated view in comparison to the view along the ⟨111⟩ zone axis. The good agreement of the left picture of Figure 3-12 with the corresponding HRTEM image shown in Figure 3-11a and also the agreement of the right picture of Figure 3-12 to Figure 3-11b proofs the very high quality of the synthesized MCM-48 silica materials.

3.4 Conclusions

For the first time mesoporous MCM-48 silica phases were synthesized with pore sizes from 2.3 to 3.5 nm (BJH), or 3.4 to 4.8 nm (NLDFT) respectively with one single surfactant. These new mesoporous materials were extensively characterized by powder X-ray diffraction, nitrogen physisorption, transition electron microscopy and electron diffraction. Besides the MCM-48 silica materials mesoporous MCM-41 silica materials with varying pore diameters have been synthesized with three different trimethylammonium bromide surfactants. The MCM-41 silica were also characterized by P-XRD and nitrogen physisorption.

Both the MCM-48 and MCM-41 silica materials show high long-range order in the P-XRD diagrams. The materials show high specific surface areas and narrow pore diameter distributions. The increase of the pore diameter of the MCM-48 silica phases depends linearly on the carbon chain length of the used surfactant.

Electron diffraction and high resolution transmission electron microscopy on the MCM-48**B** silica proof the $I4_1/a\bar{3}2/d$ space group of the material and the very well structural order as already found by P-XRD.

In comparison to the recently introduced synthesis by mixtures of cationic alkyltrimethylammonium surfactants (alkyl chain length from 12 to 20 carbon atoms) with neutral cosurfactants (polyoxyethylene alkyl ethers) [72,73] this new method with the increase of the surfactant head group is based only on one surfactant species and gives excellent results with respect to the structural ordering and surface properties. It is an important hint to future investigations in the synthesis of mesostructured and mesoporous materials. It may allow to gather new insight in the processes that occur during the synthesis of these materials. It proves the problems with easy models like the effective surfactant ion pair packing parameter g (see Chapter 1.1).

4 Systematic physisorption studies on mesoporous silica

Apart from P-XRD, nitrogen physisorption is the method of choice to characterize mesoporous materials. This method gives information on the specific surface area and the mean pore diameter. Even if the applied theories for the calculation of the pore diameters of small mesopores (< 5 nm) are still not perfect they can be used to give proper information about the differences between various mesoporous materials. Calculations of mean pore diameters of mesoporous materials on the basis of the BJH theory are common. These calculations are based on the Kelvin equation and underestimate the mean pore diameter of small mesopores by the magnitude of at least 1 nm [37]. Nevertheless, comprehensive studies have shown that, compared to other theories for pore size calculations like Saito-Foley (SF) [176,177] or non-local density functional theory (NLDFT) [47,123], the BJH method gives appropriate results to determine the differences between pristine and modified MCM-48 silica materials [11,12].

4.1 N_2, Ar, and Kr at 77 K and 87 K in various MCM-48 silica

4.1.1 Characterization of MCM-48 silica by physisorption

In these studies mesoporous MCM-48 silica phases comparable to the materials described in Chapter 3 were used. The materials were chosen due to their value for the investigation of phenomena occurring in physisorption experiments in the mesoporous range. The MCM-48 silica materials $\mathbf{A_1}$, $\mathbf{B_1}$, and $\mathbf{C_1}$ discussed in this chapter are characterized in Table 4-1 with respect to their unit cell parameter a, the specific surface area A_s(BET), the pore size distribution calculated by BJH, SF or NLDFT theory D_p, pore volume V_p, and pore wall thickness t_{pw} calculated as described in Chapter 3.2. In addition, argon physisorption isotherms at 87 K for all materials were analyzed with respect to pore size D_p(SF) and pore volume V_p(SF) by applying the Saito-Foley method.

Figure 4-1 and Figure 4-2 show nitrogen and argon physisorption isotherms measured at 77 K and 87 K for different pristine MCM-48 silica materials. The N_2 isotherms at

Table 4-1: Characterization of the pristine MCM-48 silica phases $\boldsymbol{A_1}$*,* $\boldsymbol{B_1}$*, and* $\boldsymbol{C_1}$ *with respect to unit cell parameter, specific surface area, pore size and pore volume using various methods.*

adsorbent	MCM-48$\mathbf{A_1}$	MCM-48$\mathbf{B_1}$	MCM-48$\mathbf{C_1}$
a [nm]	8.08	8.48	9.19
A_s(BET) [m^2/g]	1261	1202	1078
V_p,N_2 [$10^{-6}m^3$/g]	0.70 (p/p_0=0.32) 0.77 (p/p_0=0.95)	0.81 (p/p_0=0.40) 0.91 (p/p_0=0.95)	0.82 (p/p_0=0.40) 0.95 (p/p_0=0.95)
D_p,N_2(BJH) [nm]	2.05	2.52	2.81
D_h,N_2 [nm]	2.21	2.68	3.04
D_p,N_2(NLDFT) [nm]	3.18	3.51	4.09
t_{pw} [nm]	1.02	0.99	0.93
D_p,Ar(BJH) [nm]	2.02	2.39	2.65
D_p,Ar(SF) [nm]	2.42	2.86	3.31
V_p,Ar(SF) [$10^{-6}m^3$/g]	0.68	0.72	0.78

A_s(BET): BET specific surface area; V_p: pore volume; D_p(BJH): BJH mode pore diameter; $D_h = 4V_p/A_s$: average pore diameter; D_p(NLDFT): NLDFT mode pore diameter; t_{pw}: pore wall thickness. Argon physisorption isotherms at 87 K for all materials were analyzed with respect to pore size (D_p(SF)) and pore volume (V_p(SF)) by applying the Saito-Foley method.

77 K as well as the physisorption isotherms of Ar at 87 K reveal for the MCM-48 silica phases $\mathbf{A_1}$ and $\mathbf{B_1}$ reversible pore condensation at relative pressures $p/p_0 < 0.4$ without physisorption hysteresis. With increasing pore size the occurrence of pore condensation is shifted to higher relative pressures as expected from classical theories of pore condensation.

Pore condensation accompanied with hysteresis is observed for argon physisorption at 87 K in MCM-48$\mathbf{C_1}$ in a relative pressure range $p/p_0 = 0.365 - 0.413$. (In addition, in the same isotherm a very small hysteresis loop at relative pressures > 0.4 is detected, which may be caused by larger meso- and macropores combined with pore blocking, i.e. network effects). The MCM-48 silica do not exhibit microporosity as revealed by

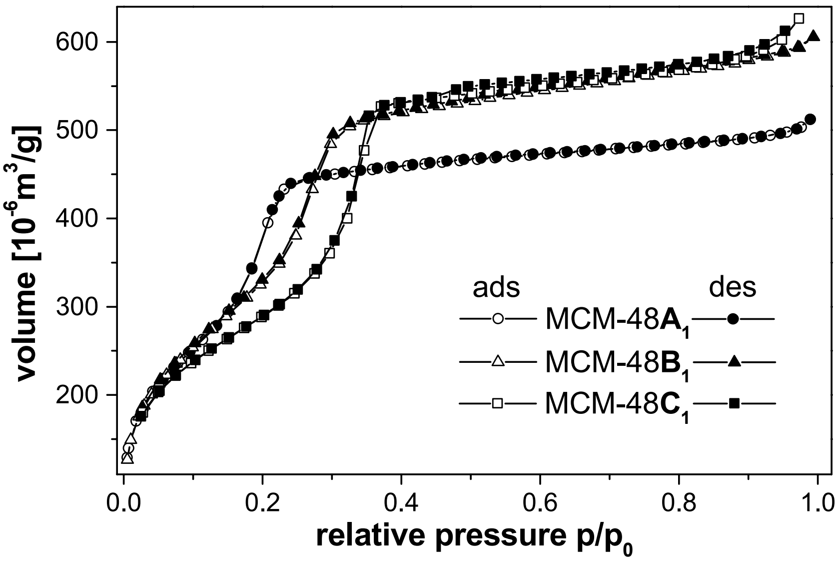

*Figure 4-1: Nitrogen physisorption isotherms (77 K) of pristine MCM-48 silica materials **A$_1$**, **B$_1$**, and **C$_1$**.*

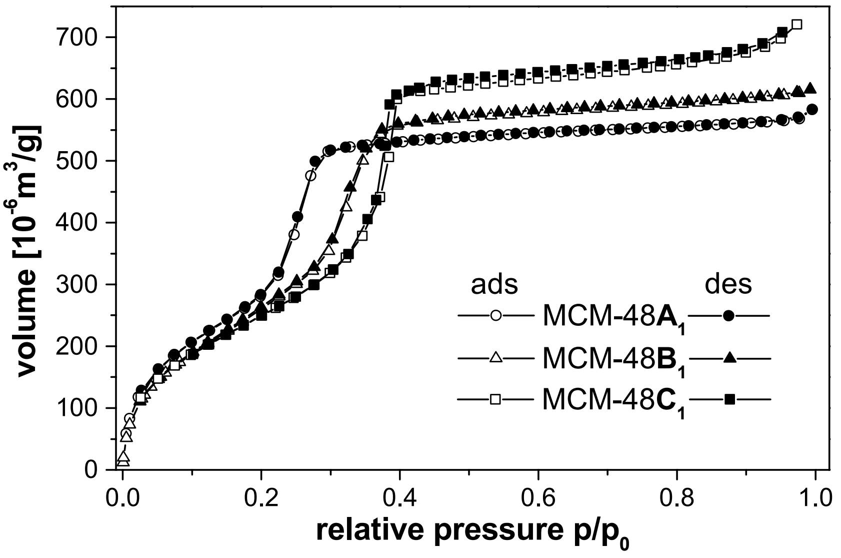

*Figure 4-2: Argon physisorption isotherms (87 K) of pristine MCM-48 silica materials **A$_1$**, **B$_1$**, and **C$_1$**.*

measurements in the low pressure region and by appropriate t-plots.

Different methods were used to analyze the nitrogen isotherms on the pristine MCM-48 silica materials with respect to surface and pore size characteristics. The results given in Table 4-1 indicate that these specific surface areas decrease, but the pore widths and pore volumes increase from MCM-48 silica **A$_1$** to **C$_1$**. The BET surface areas were determined from nitrogen isotherms at 77 K in a range of relative pressures p/p_0 prior to the occurrence of pore condensation for each MCM-48 (**A$_1$**: 0.07-0.15; **B$_1$**: 0.07-0.15; **C$_1$**: 0.07-0.25) assuming a cross-sectional area of a nitrogen molecule to be

0.162 nm^2. However, as already indicated for small pore MCM-41 silica material [118], the BET method is inaccurate for estimating the surface area for MCM-48 silica materials because pore condensation also occurs within the relative pressure range 0.05–0.3, where the BET theory is usually considered to be valid. Thus, pore filling is observed at pressures very close to the pressure range in which monolayer-multilayer formation on the pore walls occurs.

Most classical methods used for the analysis of "meso"pore size distributions (PSD) from physisorption isotherms, like the most prominent method of Barett, Joyner and Halenda (BJH) [70,86], are based on macroscopic thermodynamic models like the modified Kelvin equation (see equation 1-1, page 8). Applying the BJH method the pore size distributions of the MCM-48 silica phases can be derived from nitrogen (77 K) and argon (87 K) isotherms. In both cases the BJH pore size distributions were calculated from the desorption branches of the physisorption isotherms by estimating the (statistical) thickness t_c of the adsorbed film at the pore walls $t_c = R_p - R_k$, where R_p is the pore radius and R_k is the Kelvin or core radius, by applying the Frenkel-Halsey-Hill approach. The BJH pore diameter (maximum of pore size distribution curves) calculated from nitrogen and argon adsorption isotherms are in good agreement with each other as shown in Figure 4-3. The obtained narrow pore size distributions and the powder X-ray diffraction patterns (not depicted) both indicate that the MCM-48 silica

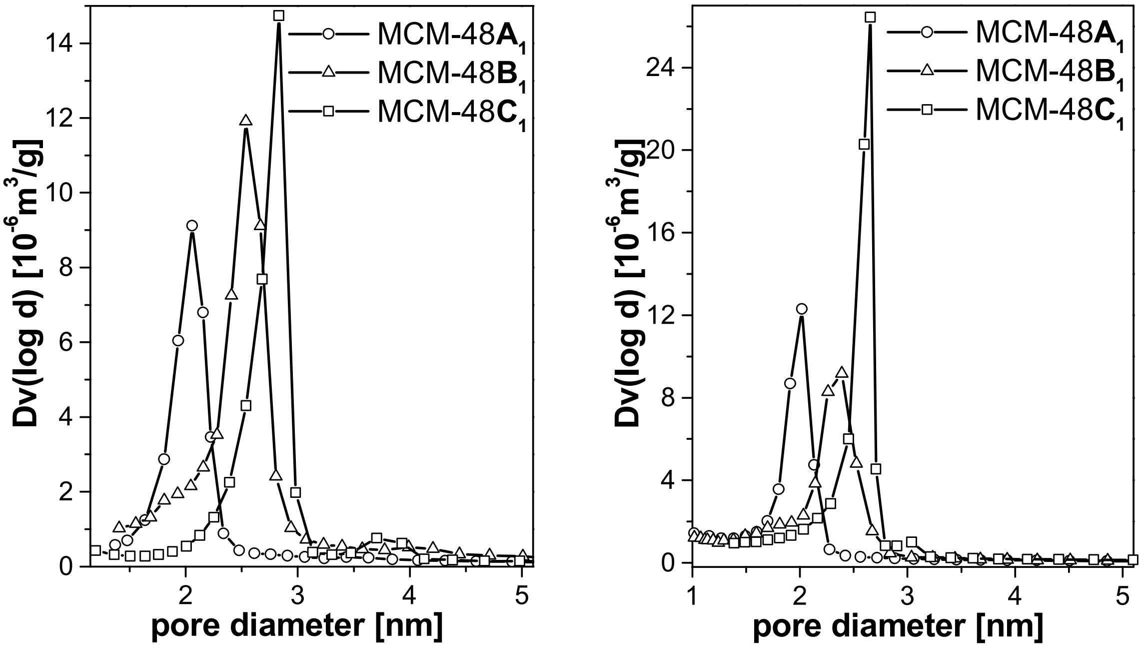

Figure 4-3: BJH pore diameter distributions (Dv(log d) ≡ dV/d(log D)) for pristine MCM-48 silica phases ***A_1****, **B_1**, and **C_1** obtained from: (left) N_2 physisorption isotherms (77 K, Figure 4-1); (right) Ar physisorption isotherms (87 K, Figure 4-2).*

materials investigated are highly ordered.

Pore volumes were calculated from the measured adsorbed gas volume by assuming the density of the capillary fluid to be equal to the density of liquid bulk nitrogen at the same temperature (Gurvich method [86]). Using the values of the pore volumes allows the determination of the average pore diameter for the primary mesopore system of MCM-48 silica according to $D_h = 4V_p/A_s$. As indicated in Table 4-1 the obtained values for D_h are slightly higher than the BJH pore diameters. The average pore diameter D_h is defined for a mesopore structure which consists of open-ended non-intersecting cylinders and is based on the assumption that the specific surface area is confined to the cylindrical pore walls. These conditions should be fulfilled in the case of the one-dimensional channel system of the MCM-41 silica phase. However, even if MCM-48 silica comprises of two three-dimensional pore systems the D_h pore diameters are still in reasonable good agreement with the BJH values.

In addition, the Saito-Foley (SF) method, which is an extension of the original Horvath-Kawazoe (HK) method [178] for slit-pore geometry (i.e., nitrogen/carbon system), was applied to the argon data at 87 K. The Saito-Foley method is based on a fundamental statistical analysis of a fluid (argon) confined to microporous cylindrical pores (zeolites) including details of the fluid-wall interaction. The HK and SF methods are widely used, and provide a better measure for micropore filling pressures than the macroscopic, classical methods of micropore analysis because they take into account details of the solid-fluid attractive forces in narrow pores. It is assumed that the filling of micropores takes place at a characteristic relative pressure which is directly related to the fluid-solid interaction energy and the effective pore radius. Thus, micropores can either be full or empty according to whether the pressure of the adsorptive is higher or lower than the value characteristic of a particular diameter, which is similar to the pore filling mechanism of pore condensation in the mesopore range. Hence, the SF method was also applied for pore size determination in narrow cylindrical mesopores of MCM-41 silica materials [124,179], and good agreement between pore diameters determined by the SF method and Kelvin-equation-based methods have been reported [179]. This is remarkable because the SF-method as described above is originally dedicated to microporous materials.

Within this context the SF method was applied to the argon physisorption isotherms of MCM-48 silica. As shown in Table 4-1 the SF values obtained for pore volumes are in good agreement with the (Gurvich) pore volumes obtained from the nitrogen isotherms at ca. $p/p_0 = 0.4$, which corresponds to the plateau of the physisorption isotherm after pore condensation has occurred in the primary mesopores of MCM-48 silica. In addition the SF pore diameters are still in the same range as the BJH and average pore diameters.

However, it should be noted that classical methods like BJH, which are based on macroscopic, thermodynamic assumptions, do not provide a reliable basis for the calculation for pore widths below 7-8 nm in case of porous carbon materials [104], and for pore diameters < ca. 3.5 nm in case of oxide materials [106]. These classical approaches are macroscopic in a sense that they do not start from a well-defined molecular model, so that a connection between molecular behavior and macroscopic properties (like the surface tension or densities of coexisting phases) is not defined. In narrow pores attractive fluid-wall interactions become dominant, so that the concept of a smooth liquid-vapor interface and bulk-like core fluid cannot realistically be applied. In contrast, DFT and molecular simulation (Monte Carlo and Molecular Dynamics) provide more accurate methods based on an accurate molecular theory. Hence, pore sizes obtained by application of the BJH method should be regarded as apparent rather than real pore sizes, although a number of studies revealed that pore sizes calculated with the BJH approach are probably still in the right range [87]. Compared with new methods that rely on microscopic descriptions like the density functional theory (DFT) and Monte Carlo computer simulation (MC), the macroscopic thermodynamic methods underestimate the calculated pore diameter by ca. 1 nm [106,122,180]. However, it should be noted that a new method, combining the Kelvin equation with an improved model of the statistical adsorbed film thickness has very recently been proposed [181]. The pore filling pressures obtained with this method are in good agreement with DFT results, except for narrow micropores.

4.1.2 Pore condensation and hysteresis in MCM-48 silica and CPG

4.1.2.1 Comparison of MCM-48 silica $\mathbf{A_1}$, $\mathbf{B_1}$, and $\mathbf{C_1}$

As already described in section 4.1.1, nitrogen isotherms at 77 K ($T/T_c = 0.61$, where $T_c = 126.20$ K is the critical temperature of the bulk fluid; $T/T_r = 1.22$, where $T_r = 63.15$ K is the triple point temperature of the bulk fluid) show for all physisorption isotherms pore condensation without hysteresis (Figure 4-1). The argon isotherms at 87 K ($T/T_c = 0.58$; $T_c = 150.66$ K; $T/T_r = 1.04$; Figure 4-2) also reveal reversible pore

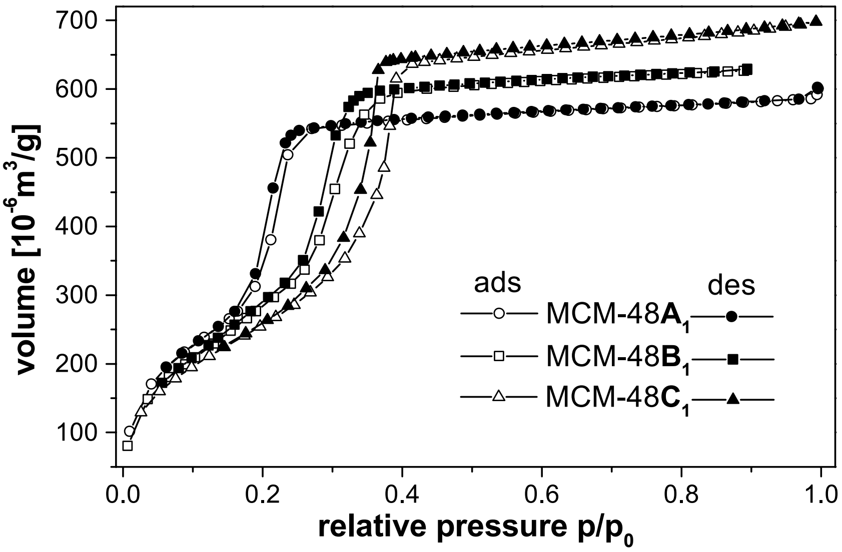

Figure 4-4: Argon physisorption isotherms (77 K) for pristine MCM-48 silica phases ***A₁*, *B₁***, *and* ***C₁***.

condensation for MCM-48**A₁** and **B₁**, but in case of MCM-48**C₁** a small hysteresis loop is detected. With increasing pore size the occurrence of pore condensation is shifted to higher relative pressures as expected from classical theories of pore condensation. In contrast to the nitrogen isotherms at 77 K and argon physisorption isotherms at 87 K the argon isotherms at 77 K ($T/T_c = 0.51$; $T/T_R = 0.92$; $T_R - T = 6.8$ K, where $T_R = 83.81$ K is the triple point temperature of the bulk fluid) reveal pore condensation accompanied by hysteresis for all MCM-48 silica studied here (Figure 4-4). A qualitatively similar pore condensation and hysteresis behavior of argon physisorption at 77 K and 87 K has recently also been observed for MCM-41 silica phases [124]. As shown in Figure 4-4, the widths of the hysteresis loops of the physisorption isotherms decrease with decreasing pore width, indicating that the fluid confined to the pores in MCM-48**A₁** may be closer to pore criticality than the fluid confined in the pores of MCM-48**C₁** at 77 K ($T_c - T = 73.3$ K). According to theoretical predictions [89,102] it is expected that at constant temperature pore criticality can be approached by reducing the pore diameter.

In all cases the pore condensation steps of the argon isotherms are much sharper than the corresponding nitrogen isotherms and the adsorbed amount after the pores are filled is higher. This is due to the smaller size of the argon molecule and the higher density of liquid argon ($\rho_l = 1.396$ g·cm^{-3} at 87.29 K) as compared to liquid nitrogen ($\rho_l = 0.870$ g·cm^{-3} at 77.35 K). However, it should be noted that also the argon pore condensation steps are smeared out over a finite pressure range for two reasons: (i) the not vanishing width of the pore size distribution of the present material (cf. Figure 4-2); (ii) intrinsic feature of phase transitions in systems of small size [102], i.e. in small cylindrical pores a rounding of the first order phase transition caused by finite size effects is to be expected.

The reversible pore condensation at $p/p_0 < 0.4$ observed for nitrogen physisorption at 77 K in the MCM-48 silica used in this study was also observed in MCM-41 silica materials of pore diameters 2-4 nm [115-124]. These observations are in accordance with the expectation that the lower closure point for nitrogen physisorption hysteresis at 77 K is around $p/p_0 = 0.42$, which was originally considered the limit of thermodynamic stability of the liquid nitrogen meniscus. Recent theoretical studies [182] and computer simulations [183] indicate that pore wall roughness and details of the fluid-wall interaction may also be significant for the disappearance of nitrogen physisorption hysteresis in M41S materials.

In a comprehensive discussion on the lack of hysteresis in N_2 isotherms at 77 K in MCM-41 silica [121] it was assumed, that the absence of experimental hysteresis of samples with mean pore size of ca. 4 nm cannot be explained by the capillary critical temperature for a given pore size being achieved. Pore condensation without hysteresis was also observed for SF_6 confined to CPG [99] and in novel ceramic silica materials of mean pore sizes < 3.5 nm [184] in a temperature range from the triple point up to the pore critical temperature. Accordingly, one would expect that physisorption hysteresis

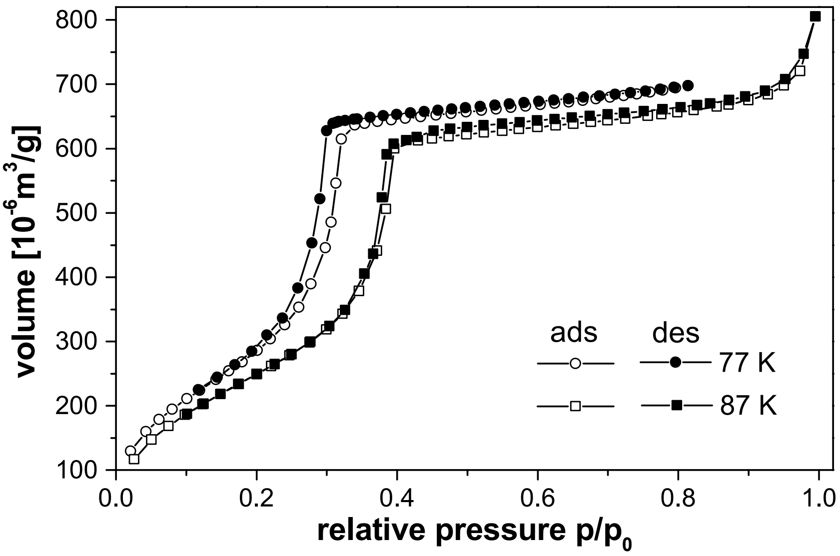

Figure 4-5: Comparison of Ar physisorption isotherms (87 K and 77 K) for MCM-48 silica phase C_1. Here, the saturation pressure of undercooled liquid Ar is chosen as p_0 for the correspondent physisorption isotherm at 77 K.

disappears already in a certain temperature range below the pore critical temperature. The observed disappearance of physisorption hysteresis in the temperature range from 77 K to 87 K for argon physisorption in the MCM-48 silica $\mathbf{A_1}$ and $\mathbf{B_1}$ is consistent with this picture and so is the decrease of the width of hysteresis loop for the mesoporous silica $\mathbf{C_1}$ as shown in Figure 4-5. For the comparison of the temperature dependence of the hysteresis and pore condensation behavior of MCM-48$\mathbf{C_1}$ the saturation pressure of the undercooled liquid ($p_{0,liquid} = 229.1$ Torr) [185] was chosen as p_0 in case of the 77 K physisorption isotherm, also because it can be assumed that the capillary phase at this temperature is still liquid [122,123]. However, in general the choice of the supercooled liquid p_0 as a reference state is not straightforward because $T < T_R$. As also discussed in context with the results shown in the Figure 4-6 to Figure 4-9; there are arguments to choose the saturation pressure of the solid instead [86,87]. The disappearance of hysteresis for argon physisorption isotherms at 87 K in the pore diameter (D_p,N_2 (BJH)) range from 2.81 nm (MCM-48$\mathbf{C_1}$) to 2.52 nm (MCM-48$\mathbf{B_1}$) is again in agreement with the expectation that for a given temperature pore criticality is approached with decreasing pore diameter [102]. The difference in the occurrence of hysteresis for nitrogen and argon at 77 K can be explained as a consequence of the lower reduced temperature of argon ($T/T_c = 0.51$) as compared to nitrogen ($T/T_c = 0.61$).

4.1.2.2 Comparison of MCM-48$\mathbf{A_1}$ and $\mathbf{C_1}$ silica with CPG

In order to compare the physisorption behavior of fluids in the small mesopores of MCM-48 silica with the pore condensation and hysteresis behavior in much larger silica pores the physisorption behavior of nitrogen and argon at 87 K and 77 K in controlled-pore glasses of mode diameters 10 nm (CPG (10nm)) and 16 nm (CPG (16nm)), which were supplied by Quantachrome Corporation, USA and BAM, Germany, was also studied. In Figure 4-6 nitrogen physisorption isotherms and in Figure 4-7 the corresponding BJH pore size distributions (obtained from the desorption branch) are compared to the MCM-48$\mathbf{A_1}$ and MCM-48$\mathbf{C_1}$ silica phases (see Table 4-1). Controlled-pore glasses also consist of an interconnected pore system, but with a much wider pores size distribution as compared to MCM-48 silica materials. As expected nitrogen physisorption hysteresis is not observed in the MCM-48 silica samples of pore diameters < 4 nm.

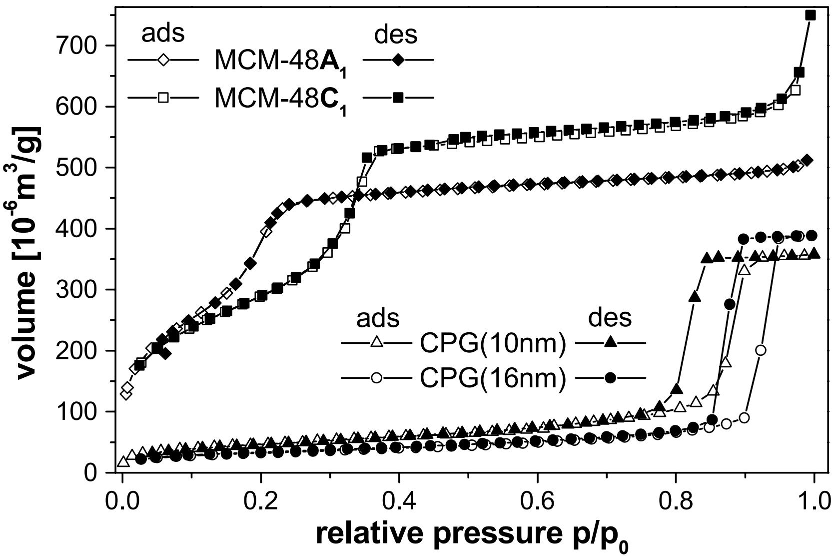

Figure 4-6: Nitrogen adsorption and desorption isotherms at 77 K for MCM-48A_1 and C_1 silica and CPG (10 and 16nm).

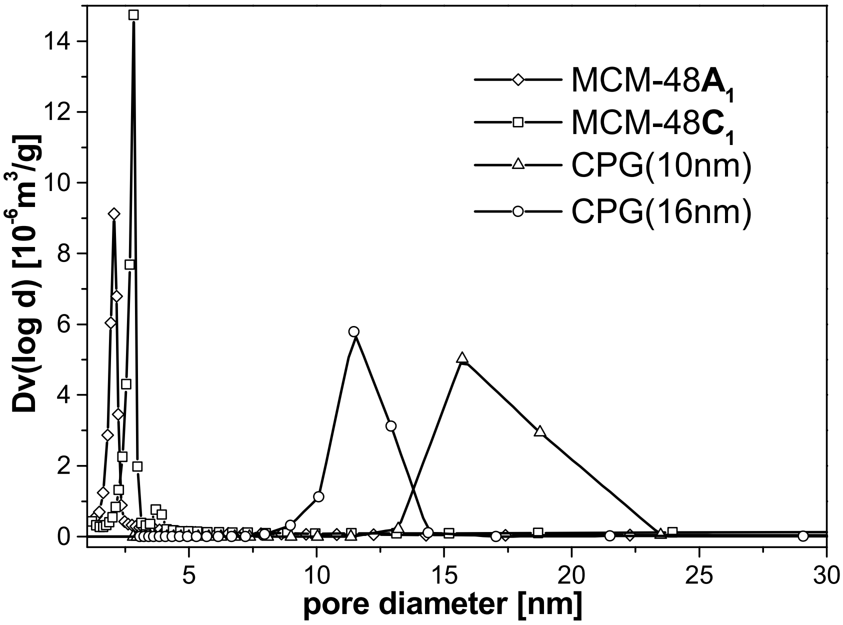

Figure 4-7: BJH pore diameter distribution for MCM-48A_1 and C_1 silica and CPG (10 and 16nm) obtained from the desorption branch of the N_2 physisorption isotherms.

Figure 4-8 shows the argon physisorption isotherms at 87 K (i.e. 3.5 K above the bulk triple point temperature $T_R = 83.8$ K). The physisorption isotherms reveal reversible pore condensation for argon in the MCM-48**A**$_1$ silica, which is, however, accompanied by hysteresis of type H1 (IUPAC classification) for argon confined to the pores of MCM-48**C**$_1$ silica and the controlled-pore glass samples. From the described experiments it can be concluded, that for MCM-48 silica materials the critical pore

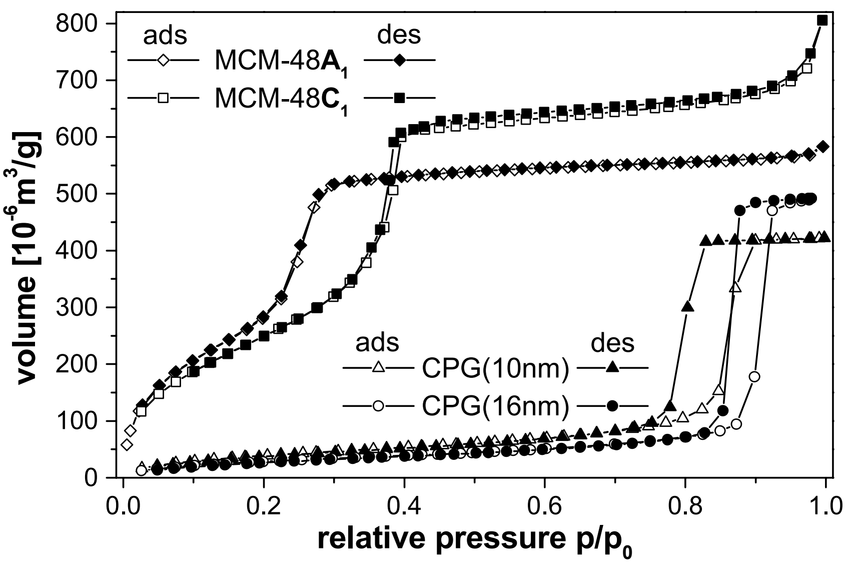

Figure 4-8: Argon adsorption and desorption isotherms at 87 K for MCM-48 $\boldsymbol{A_1}$ *and* $\boldsymbol{C_1}$ *silica and CPG (10 and 16 nm).*

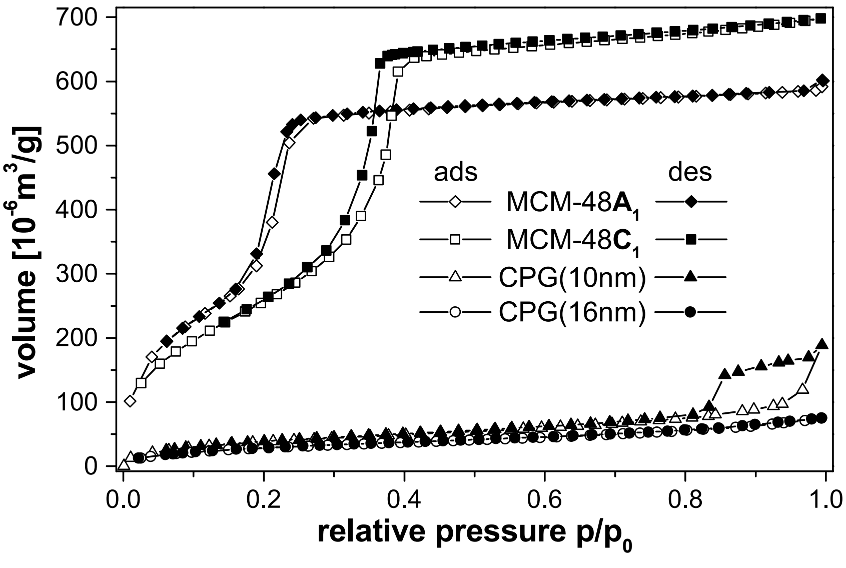

Figure 4-9: Argon adsorption and desorption isotherms at 77 K for MCM-48$\boldsymbol{A_1}$ *and* $\boldsymbol{C_1}$ *silica and CPG (10 and 16 nm).*

diameter for the occurrence of argon physisorption hysteresis is located between BJH pore diameters of 2.52 nm and 2.81 nm (i.e. NLDFT: 3.53 – 4.09 nm) for 87 K and for 77 K between BJH pore diameters of 1.74 and 2.05 nm (i.e. NLDFT: 2.70 - 3.18 nm) [12].

Figure 4-9 shows the physisorption and phase behavior of argon in these materials at 77 K, i.e. 6.8 K below the bulk triple point temperature. In contrast to the physisorption behavior at 87 K, a hysteresis loop is now also observed for MCM-48$\mathbf{A_1}$ silica and the hysteresis loop of MCM-48$\mathbf{C_1}$ silica is more pronounced. A small pore condensation step associated with a broad hysteresis loop is still observed for the argon physisorption isotherm in CPG (10nm), but the adsorbed amount is much lower as compared to the adsorption at 87 K, indicating a partial filling of the CPG pores. However, a pore condensation step is not observed anymore for argon physisorption in CPG (16nm). The observed differences in the physisorption and pore condensation behavior for the systems argon/MCM-48 and argon/CPG at 87 K and 77 K reflect that for a given temperature the thermodynamic state of the confined fluid is different in the narrow pores of MCM-48 silica as compared to the much larger pores of CPG.

Figure 4-8 and Figure 4-9 also show that the adsorbed amount of fluid in MCM-48 silica is much higher in comparison to controlled-pore glass, which is due to the much higher specific surface area and pore volume of MCM-48 silica. This physisorption behavior underlines the unique texture of MCM-48 silica and its potential for several practical applications in comparison with other well-defined mesoporous materials.

Phase transitions of the pore fluid were also observed for krypton in MCM-48 silica materials at 87 K ($T/T_c = 0.42$, $T_c = 209.4$ K) which is 28.5 K below the bulk triple point temperature ($T_R = 115.8$ K). The physisorption isotherm at 87 K for MCM-48**A**$_1$ and MCM-48**C**$_1$, presented in Figure 4-10, both exhibit a hysteresis loop of type H1, which is much broader for MCM-48**C**$_1$ as compared to MCM-48**A**$_1$, i.e. as in case of the argon isotherms at 77 K the width of the hysteresis loop decreases with decreasing pore width, indicating that at a certain pore width the occurrence of a first order phase transition is

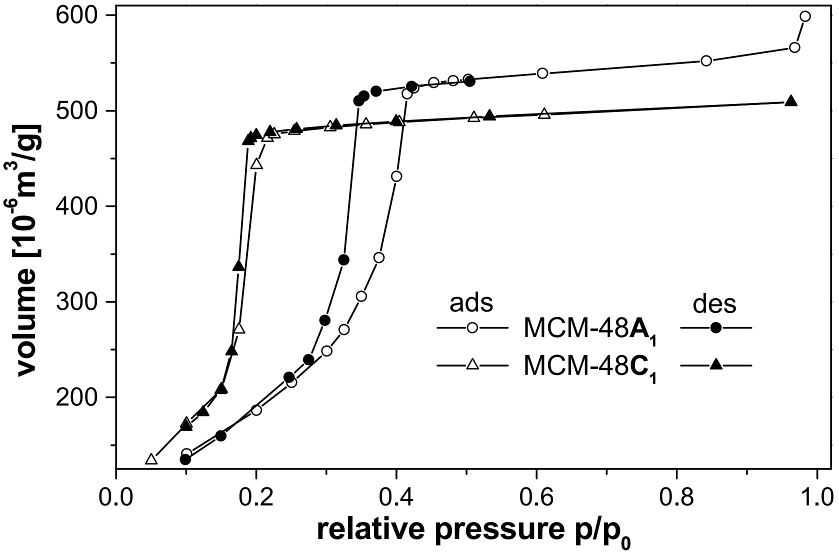

Figure 4-10: Krypton physisorption (87 K) for pristine MCM-48 silica materials ***A***$_1$ *and* ***C***$_1$*. The chosen* p_0*-value is the saturation pressure of solid Kr at 87 K.*

not possible anymore. In order to explain the observed pore size dependence of the physisorption hysteresis, it might be argued that, as in case of the argon isotherms at 77 K, the pore fluid of MCM-48**A₁** (D_p,N_2 = 2.05 nm) is much closer to pore criticality than the confined fluid in MCM-48**C₁** (D_p,N_2 = 2.81 nm). However, the nature of the observed phase transitions, ca. 122 K below the bulk critical temperature and 28.5 K below the bulk triple point, is not clear. In a recent paper the observation of a solidification of the krypton capillary phase at 77 K [177] in the pores of MCM-41 silica (mean pore diameter ca. 4 nm) was reported by employing microcalorimetric techniques, neutron diffraction and physisorption measurements. In addition, a systematic study of physisorption hysteresis of different gases (CO_2, Xe, N_2) in porous vycor glass (mean pore diameter ca. 6 nm) in a temperature range from well below the bulk triple point temperature up to the critical temperature revealed the disappearance of physisorption hysteresis on approaching the bulk critical temperature and in a temperature range below the bulk triple point, indicating a critical point shift to lower temperature and a closure of the (hysteresis) phase diagram of the pore fluid below the triple point temperature of the bulk fluid [186].

In order to discuss the described different physisorption and phase behaviors of krypton and argon in MCM-48 silica and controlled-pore glass at temperatures below the bulk triple point temperature in more detail, an schematic (p-T) diagram (Figure 4-11) of a fluid confined to pores of different widths H_1 and H_2 ($H_1 > H_2$) together with

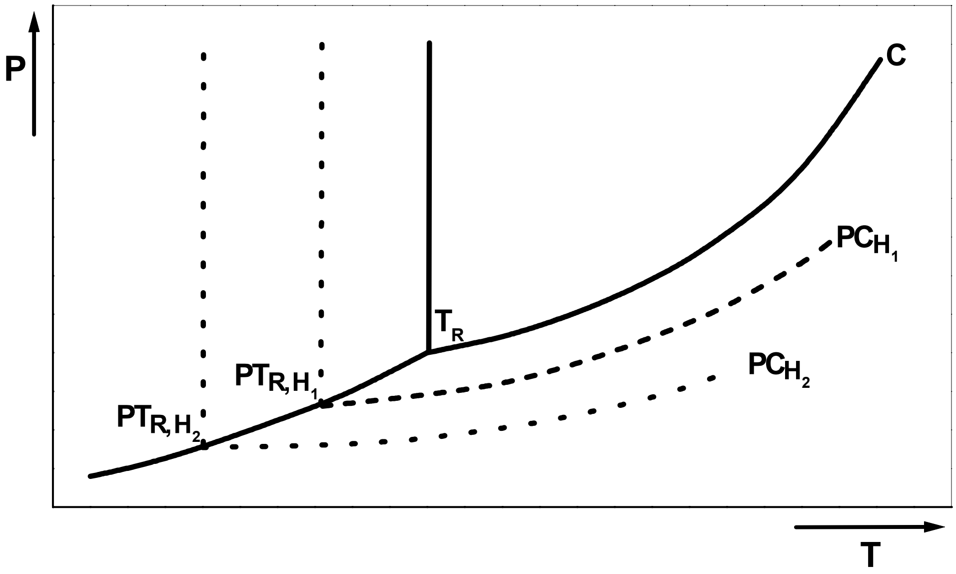

Figure 4-11: Schematic p-T diagram of a bulk fluid and pore fluid confined to different sized pores (width $H_1 > H_2$) [12].

the p-T diagram of the bulk fluid (bold lines) is employed. This schematic phase diagram is based on results obtained in theory, computer simulations and experiments in recent years [99,102,109-113]. The pore condensation line of a pore fluid, which defines the locus of states of the unsaturated vapor at which pore condensation will occur in pores of given size and shape, terminates in a pore critical point (PC_{H1} and PC_{H2}), which is shifted to lower temperature and pressure with respect to the bulk fluid. Moreover, the pore condensation lines are expected to extend down to an appropriate pore triple point ($PT_{R,H1}$ and $PT_{R,H2}$), which may also be shifted to lower temperature. In such a case the shift of the pore triple point temperature compared to the bulk value is expected to increase with decreasing pore width [109-111]. Unfortunately, in comparison with the relatively large number of publications in recent years dealing with pore criticality, not much work has been published so far concerning the details of the phase diagram of a pore fluid below the bulk triple point. As a consequence the locus (p-T) of the pore triple point in a general phase diagram is not very well known. Owing to this situation the pore condensation and freezing lines for the pore fluid in the low temperature region are shown as dashed lines indicating the speculative status of the low temperature region in the schematic phase diagram.

However, a similar phase diagram as shown in Figure 4-11 was indeed derived for CO_2 confined to porous vycor glass from positron and positronium annihilation experiments [110]. In these experiments it was found that the pore condensation line terminates in a (*quasi*) pore triple point, which is reduced both in temperature and pressure from that of the bulk. Similar results were obtained from a Monte-Carlo simulation of a Lennard Jones fluid confined to a slit pore [111]. In the light of these results the very different argon physisorption behavior observed for MCM-48 silica $\mathbf{A_1}$ and $\mathbf{C_1}$and controlled-pore glass at 87 K and 77 K described above may be discussed in the following way: At 87 K (Figure 4-8) pore condensation occurs for argon in CPG and MCM-48 silica, which indicates that in both cases the pore condensation line (see Figure 4-11) is crossed below the pore critical temperature. Hysteresis is observed for the Ar/CPG system but not in the narrow pores of MCM-48$\mathbf{A_1}$ silica, in accordance with theoretical expectations [102], that at a given temperature hysteresis should eventually disappear with decreasing pore size. The physisorption isotherms of Ar in MCM-48 silica still reveal pore condensation and physisorption hysteresis at 77 K, indicating that here, in contrast to the Ar/CPG system, the pore condensation line extends at least down to this temperature. This implies that the (*quasi*) triple point of the confined argon in

MCM-48 silica of pore diameter (D_p,N_2(BJH) ≤ ca. 4 nm) is shifted by more than ca. 6.5 K to lower temperature as compared to bulk argon. In contrast, the lack of pore condensation and hysteresis for argon at 77 K in CPG (16nm) indicates that there is no extension of the pore condensation line down to this temperature at pressures lower than the corresponding sublimation pressure of the bulk fluid. Only adsorption exists in the pores without any phase transition until solidification of the bulk fluid occurs (in case of Ar physisorption at 77 K the saturation pressure of Ar solidified in a special p_0-cell was measured simultaneously during the physisorption experiment; $p_{0,solid} \approx 195$ Torr). However, in case of CPG (10nm) pore condensation and a physisorption isotherm with a truncated hysteresis loop is observed. According to the pore size distribution curves shown in Figure 4-7, CPG (16nm) has no pores of diameters < 12 nm, whereas CPG (10nm) exhibits pores of diameters from ca. 8 nm up to ca. 16 nm. Accordingly, in the smaller pores of CPG (10nm) pore condensation can still occur, whereas in the pores > 12 nm no phase transition occurs, leading to a partially filled CPG (10nm). In contrast, MCM-48 silica where all pores have pore diameters < 4 nm, the complete pore system can be filled by pore condensation as also revealed by the plateau values of the physisorption isotherms.

It is often argued [86,87] that instead of the saturation pressure of solid argon at 77 K – as used in this study – the saturation pressure of supercooled liquid argon should be employed. In this case it might be concluded that it is not possible to measure a complete argon isotherm at 77 K as bulk solidification occurs before the saturation pressure for liquid argon is achieved, which would lead to a truncated isotherm without capillary condensation and hysteresis for argon in CPG at this temperature. However, this would mean that for 77 K ($T_R - T \approx 6.5$ K) the pore condensation pressure would be higher than the corresponding sublimation pressure of the bulk fluid, indicating that for the system Ar/CPG the pore condensation line would cross the bulk sublimation line somewhere below the bulk triple point temperature but above 77 K. However, this is not to be expected from a theoretical point of view: For instance, in a recent free-energy study [111] the complete phase diagram for weakly attractive and repulsive forces was calculated; these results did not show any indication for such a crossing of the bulk sublimation line by the pore condensation line. Hence, it must be concluded that pore condensation of argon in the pores of CPG does not occur at 77 K, because this temperature seems to be already lower than the (*quasi*) pore triple point temperature of the confined argon.

4.2 Physisorption and pore condensation in M41S silica

In order to compare the physisorption and phase behavior of pure fluids in a well-defined three-dimensional pore network with the behavior in a pseudo one-dimensional geometry, physisorption isotherms of nitrogen and argon at 77 K and 87 K were measured on MCM-48**C**$_2$ and MCM-41**C** silica samples. The nitrogen physisorption isotherms at 77 K are shown in Figure 4-12. Both physisorption isotherms reveal reversible pore condensation without hysteresis loop. The slope of the pore condensation steps is similar and the isotherms exhibit very similar pore condensation pressures and are therefore expected to have comparable pore size and pore size distribution curves as shown in Figure 4-13. A comprehensive summary of surface and pore size properties is given in Table 4-2. Since the pore volumes obtained from nitrogen and argon adsorption isotherms (Figure 4-14) are almost equal, these differences are due to the observed significant deviations between argon and nitrogen specific surface areas. The BET surface areas were determined from nitrogen isotherms at 77 K (Figure 4-12) in a range of relative pressures p/p_0 prior to the occurrence of pore condensation for each sample MCM-48**C**$_2$: 0.05-0.3, MCM-41**C**: 0.05-0.3) by assuming the cross-sectional area of N_2 to be 0.162 nm^2 [86]. In addition BET surface areas were also calculated from argon physisorption isotherms (see Figure 4-14) in the above stated relative pressure ranges by assuming a cross-sectional area of Ar to be 0.138 nm^2 [86]. As also reported by other groups [187] the BET specific surface areas derived from nitrogen isotherms are significantly higher than the BET surface areas obtained form

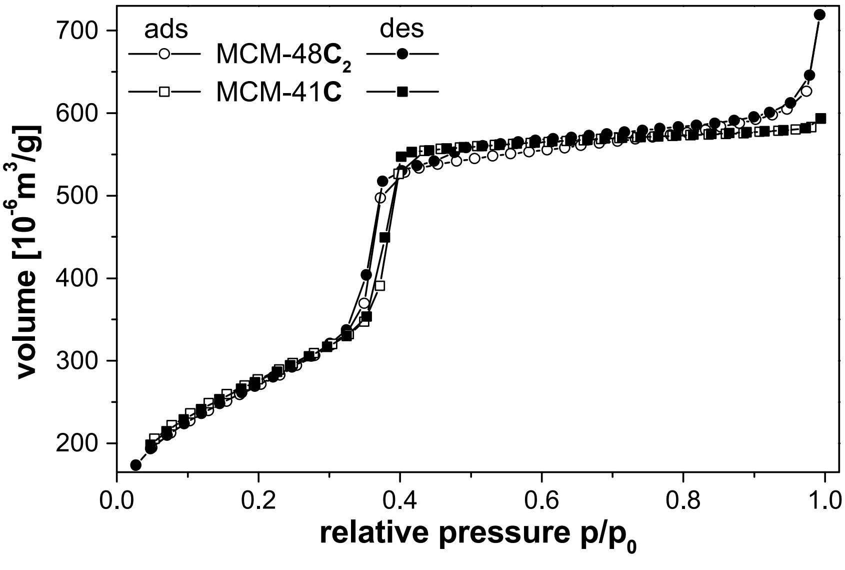

*Figure 4-12: Nitrogen adsorption and desorption isotherms at 77 K in MCM-48**C**$_2$ and MCM-41**C** silica.*

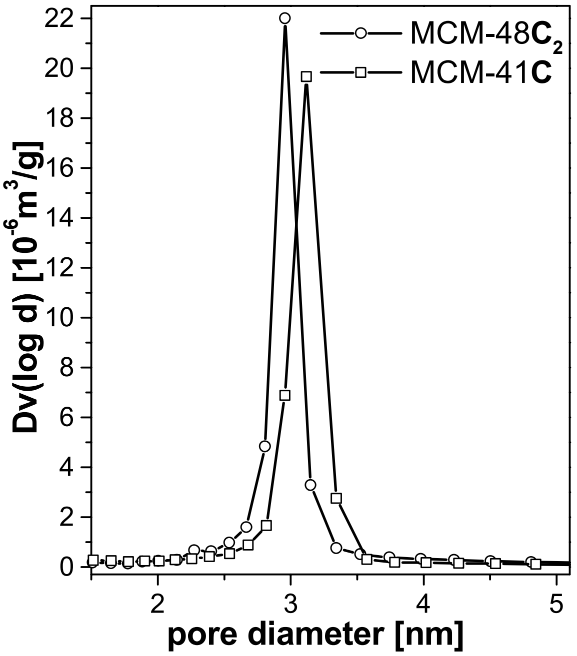

*Figure 4-13: BJH pore size distribution for MCM-48**C**$_2$ and MCM-41**C** silica.*

*Table 4-2: Characterization of MCM-48**C**$_2$ and MCM-41**C** silica by nitrogen (77 K) and argon (87 K) physisorption measurements.*

Ads.	MCM-48**C**$_2$	MCM-41**C**
A$_s$,N$_2$ (BET) [m^2/g]	994	996
A$_s$,Ar (BET) [m^2/g]	800	833
D$_p$,N$_2$(BJH) [nm]	2.92	3.15
D$_p$,N$_2$(NLDFT) [nm]	4.25	4.41
D$_h$,N$_2$ [nm]	3.34	3.45
D$_h$,Ar [nm]	3.95	3.98
V$_p$,N$_2$ [10^{-6}m^3/g]	0.83 ($p/p_0 = 0.43$)	0.86 ($p/p_0 = 0.46$)
V$_p$,Ar [10^{-6}m^3/g]	0.79 ($p/p_0 = 0.48$)	0.83 ($p/p_0 = 0.48$)

A_s(BET): BET specific surface area; D_p(BJH): BJH mode pore diameter; D_p(NLDFT): NLDFT mode pore diameter; $D_h = 4V_p/A_s$: average pore diameter; V_p: pore volume.

argon physisorption isotherms at 87 K (see Table 4-2), although the specific pore volumes obtained from argon and nitrogen physisorption isotherms are in good agreement. Apparently the BET method is inaccurate for estimating the surface area for MCM-48 and MCM-41 silica materials of pore widths < 4 nm, because pore condensation also occurs within the relative pressure range $p/p_0 = 0.05\text{-}0.3$, where the BET theory is usually considered to be valid. Thus pore filling is observed at pressures very close to the pressure range where monolayer-multilayer formation on the pore walls occurs which may lead to a significant overestimation of the monolayer capacity in case of an BET analysis [84,187]. In addition, there is some doubt, that the commonly assumed cross-sectional area of 0.162 nm^2 is incorrect for hydroxylated silica surfaces. Recently a value of 0.135 nm^2 was proposed, which was obtained by measuring the volume of N_2 adsorbed on silica spheres of known diameter [179]. By using 0.135 nm^2 as cross sectional area, the BET areas obtained from nitrogen adsorption are in good agreement with the values obtained from argon adsorption i.e., MCM-48**C₂**: A_s,N_2 = 828 m^2/g and MCM-41**C**: A_s,N_2 = 830 m^2/g. These surface areas lead to average pore diameters D_h for MCM-48**C₂** (4 nm) and MCM-41**C** (4.2 nm) silica, which are in good agreement with the NLDFT pore size results and the average pore diameters obtained from argon adsorption.

In Figure 4-14 physisorption isotherms of argon in MCM-48**C₂** and MCM-41**C** silica at 87 K and Figure 4-15 at 77 K are shown for comparison. The argon physisorption isotherms at 87 K reveal hysteresis for both materials, although the hysteresis loop for MCM-48 silica is much narrower compared to MCM-41 silica. In case of MCM-41**C** silica the hysteresis loop at 87 K is of triangular shape due to the fact that the desorption branch is slightly steeper than the adsorption branch. According to the triangular shape of the physisorption isotherm the steepness of the desorption branch may result from the proximity to a lower limit of pressure at which hysteresis loops can be observed [187]. This may also explain why, although pore condensation occurs for MCM-41**C** silica at a higher relative pressure compared to MCM-48**C₂** silica, the capillary evaporation (desorption branch of hysteresis loop) occurs for both materials at the same relative pressures (p/p_0 ca. 0.38). The width of the hysteresis loops are expected to increase with decreasing temperature, hence pronounced hysteresis (now with parallel adsorption and desorption branches) is observed at 77 K for both materials. The width of the physisorption hysteresis loops observed in MCM-48**C₂** is again smaller as compared to MCM-41**C** silica and are located within the broad hysteresis loops of MCM-41**C** silica.

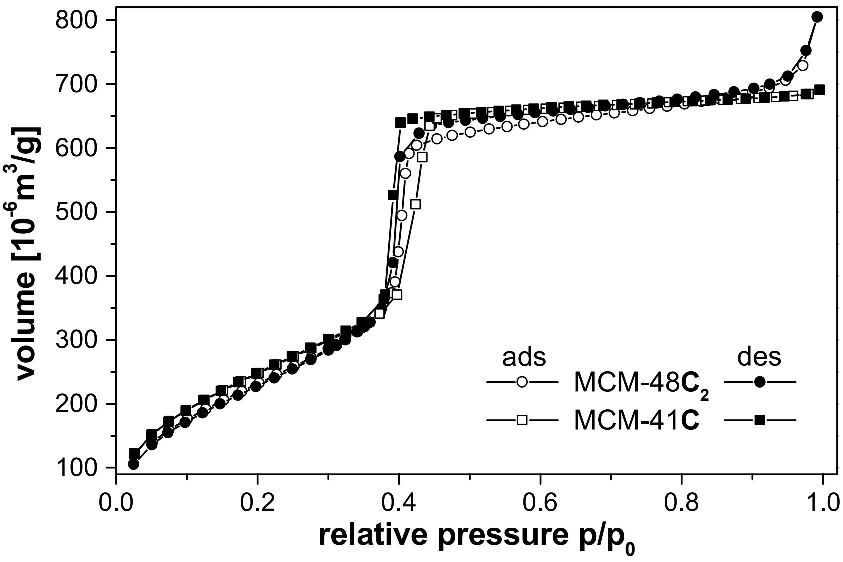

*Figure 4-14: Argon adsorption and desorption isotherms at 87 K in MCM-48$\mathbf{C}_2$ and MCM-41**C** silica.*

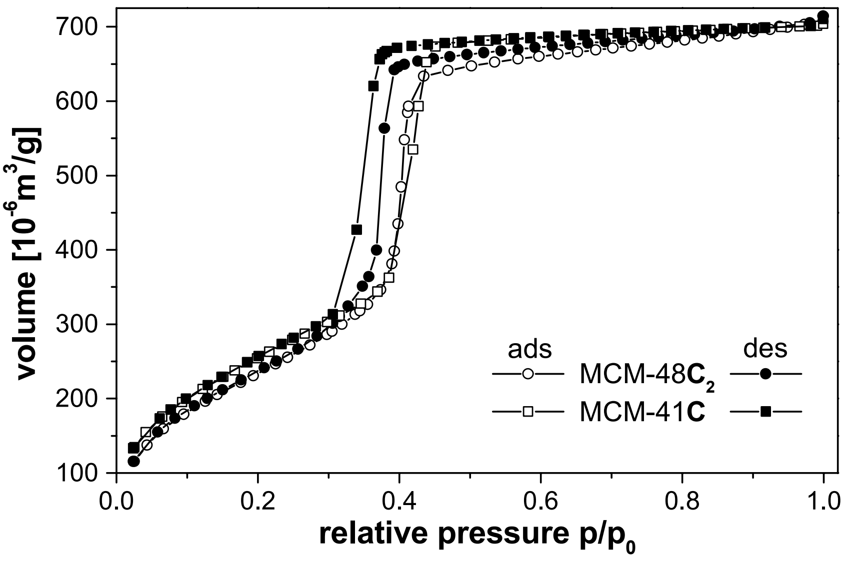

*Figure 4-15: Argon adsorption and desorption isotherms at 77 K in MCM-48$\mathbf{C}_2$ and MCM-41**C** silica.*

The broad hysteresis loops for MCM-41 silica may have different reasons: The pore diameter of MCM-41 silica is slightly higher (see Table 4-2); an increase of the width of the hysteresis loop with increasing pore diameter was observed for MCM-41 [84] and MCM-48 silica [12]. Small differences in the width of the pore size distribution may also play a role. However, it cannot be excluded that differences in the porous structure of MCM-48 and MCM-41 silica are also of importance with regard to the observed significant difference in the width of hysteresis loops. The occurrence of hysteresis in isolated cylindrical pores of MCM-41 silica indicates that hysteresis may be considered as an intrinsic property of a phase transition in a single pore, reflecting the existence of metastable gas states associated with a first order gas-liquid phase transition. Phase transition of fluids confined to narrow pores is expected to be affected by the dimensionality of the confined pore space. For instance, phase transitions in narrow pseudo one-dimensional geometric pores (e.g., isolated cylindrical pores of pore diameters $< 20\ \sigma$, where σ is the molecular diameter) are expected to be rounded due to finite size effects and the shape of the coexistence curve of a confined fluid is expected to be different for a pseudo one-dimensional geometry as compared to a three-dimensional system [113]. Further experimental and theoretical work is necessary in order to investigate whether in isolated cylindrical pores (as in MCM-41 silica) metastable states associated with pore condensation extend over a larger relative pressure range as compared to a three-dimensional network of cylindrical pores (as in MCM-48 silica) and, thus, lead to broader hysteresis loops of physisorption isotherms in MCM-41 compared to MCM-48 silica of the same pore diameter.

4.3 Pore diameter estimation: Adsorption versus desorption

As indicated before, the nitrogen physisorption isotherms do not show any physisorption hysteresis for all MCM-48 and MCM-41 silica materials presented in this work. This is observed even in case of the mesoporous MCM-48**D** silica with a mode pore diameter of ca. 4.6 nm (see Table 3-3, page 30). Figure 4-16 shows the comparison of the nitrogen and argon isotherms of the MCM-48**D** silica phase.

In contrast to the 77 K nitrogen physisorption isotherm the 87 K argon physisorption isotherm shows a distinct hysteresis loop. Whereas the pore filling step observed in the reversible nitrogen isotherms represents the equilibration transition, it is not clear whether a hysteresis loop is present as in case of argon physisorption at 87 K.

Hence, it is interesting to compare the NLDFT pore size distribution curves obtained from nitrogen adsorption/desorption and argon adsorption/desorption data (Figure 4-17). As clearly shown in Figure 4-17 the pore size distribution obtained from the argon desorption branch is in perfect agreement with the results obtained from the adsorption/desorption branch of the fully reversible nitrogen isotherm, whereas large

deviations are observed if the adsorption branch is chosen for the pore size analysis. This confirms, that although the MCM-48 silica material consists of an interconnected pore structure, i.e. two unconnected, well defined three-dimensional pore systems, the

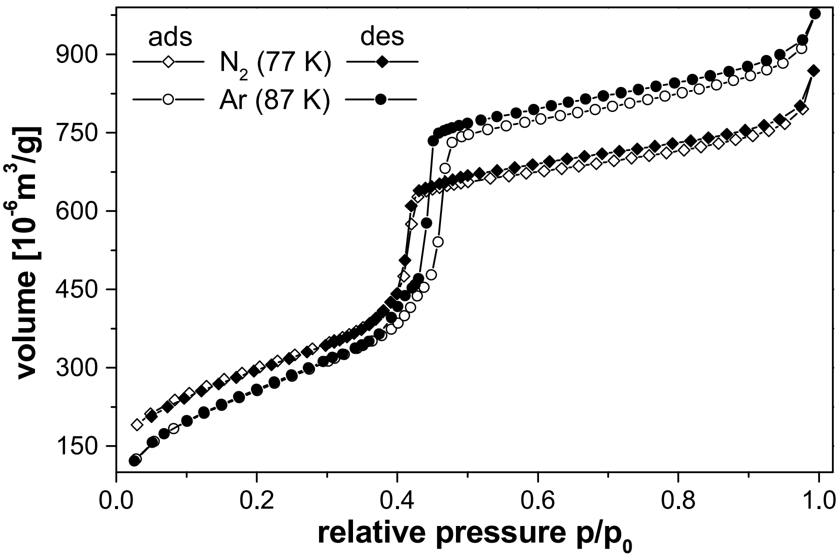

*Figure 4-16: Nitrogen (77 K) and argon (87 K) adsorption and desorption isotherms obtained on MCM-48**D** silica.*

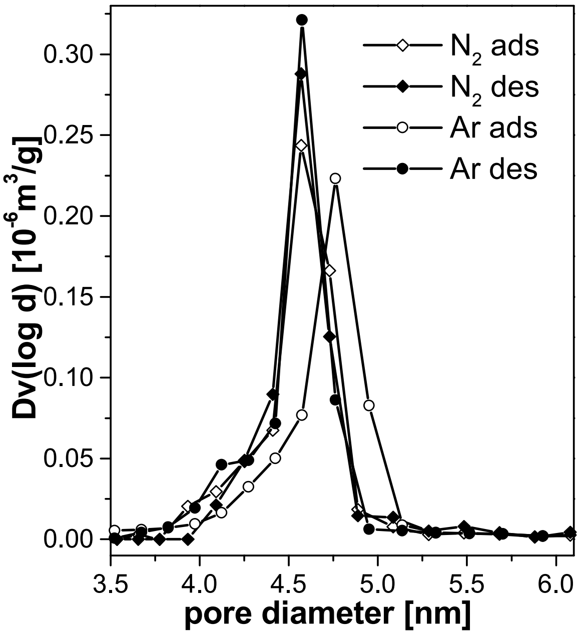

*Figure 4-17: NLDFT pore size distributions curves from N_2 (77 K) and Ar (87 K) physisorption data of MCM-48**D** silica.*

desorption branch of the hysteresis loop reflects the equilibrium phase transition. This observation confirms that hysteresis even in interconnected pore systems is in fact associated with the development of metastable fluid states associated with the pore condensation process. Similar results were obtained for MCM-41 silica materials, but contrary to MCM-48 silica, these materials consist of independent cylindrical pores [123].

4.4 Physisorption studies on a selected host/guest compound

Apart from the interest in the MCM-48 silica material as model adsorbent there is another point of interest due to the utilization of this system as a host for the incorporation of transition metal oxides, as will be discussed in the next chapter.

In order to investigate whether the loading of iron oxide into the mesopores leads to differences in the physisorption properties a comparative study on pristine MCM-48**B_1** silica (see section 4.1.1) and the **B_1-Fe_2O_3*** material was performed. Different methods were used to analyze nitrogen (77 K) and argon physisorption (87 K) isotherms to obtain precise information about surface and pore size characteristics for these materials. The results for the MCM-48**B_1** silica are shown in Table 4-1 (page 38). The corresponding data for the **B_1-Fe_2O_3** material are given in Table 4-3.

*Table 4-3: Characterization of **B_1-Fe_2O_3** with respect to specific surface area, pore size and pore volume using various methods (see Table 4-1).*

	B_1-Fe_2O_3
A_s(BET) [m^2/g]	695
V_p,N_2 [$10^{-6}m^3/g$]	0.40 (p/p_0=0.40) 0.45 (p/p_0=0.95)
D_p,N_2(BJH) [nm]	2.23
D_h,N_2 [nm]	2.31
D_p,Ar(BJH) [nm]	2.16
D_p,Ar(SF) [nm]	2.61
V_p,Ar(SF) [$10^{-6}m^3/g$]	0.38

A_s(BET): BET specific surface area; D_p(BJH): BJH mode pore diameter; $D_h = 4V_p/A_s$: average pore diameter; V_p: pore volume.

---

* The material **B_1-Fe2O3** was prepared by the same procedure as *Fe*-**8A-1** with MCM-48**B_1** as host system (for further detail refer to Chapter 2.3.1, page 17).

The in-situ formation of iron(III) oxide within the pores of the pristine MCM-48 silica phase results in a decrease of specific surface area, pore volume and pore diameter. A direct comparison of BJH pore size distribution curves obtained from nitrogen isotherms (77 K) and argon physisorption isotherms (87 K) for MCM-48**B_1** and **B_1-Fe_2O_3** is shown in Figure 4-18 (the appropriate physisorption isotherms are shown in Figure 4-1, Figure 4-2, Figure 4-20 and Figure 4-21, respectively). Argon and nitrogen BJH curves reveal both a decrease in the BJH mode diameter of phase **B_1-Fe_2O_3**, whereas the width of the pore size distribution is similar in both cases. In all cases the pore diameter of the impregnated MCM-48 silica phase was lowered of about 0.2-0.3 nm compared to the pristine MCM-48**B_1**, although the absolute values obtained for the BJH and SF (Ar, 87 K) pore diameter are slightly different. A similar shift of the pore diameter was obtained by calculating the average pore diameter according to $D_h = 4V_p/A_s$, by assuming cylindrical pores.

A NLDFT pore size analysis for iron coated mesoporous silica phases is not applicable by now, as no software application allows the calculation of the forces between an iron oxide surface and nitrogen or argon.

The nitrogen physisorption isotherms at 77 K and 87 K on **B_1-Fe_2O_3** depicted in Figure 4-19 reveal a small step due to pore condensation but no hysteresis. Figure 4-19 shows the temperature dependence of the pore filling step of nitrogen isotherms. At

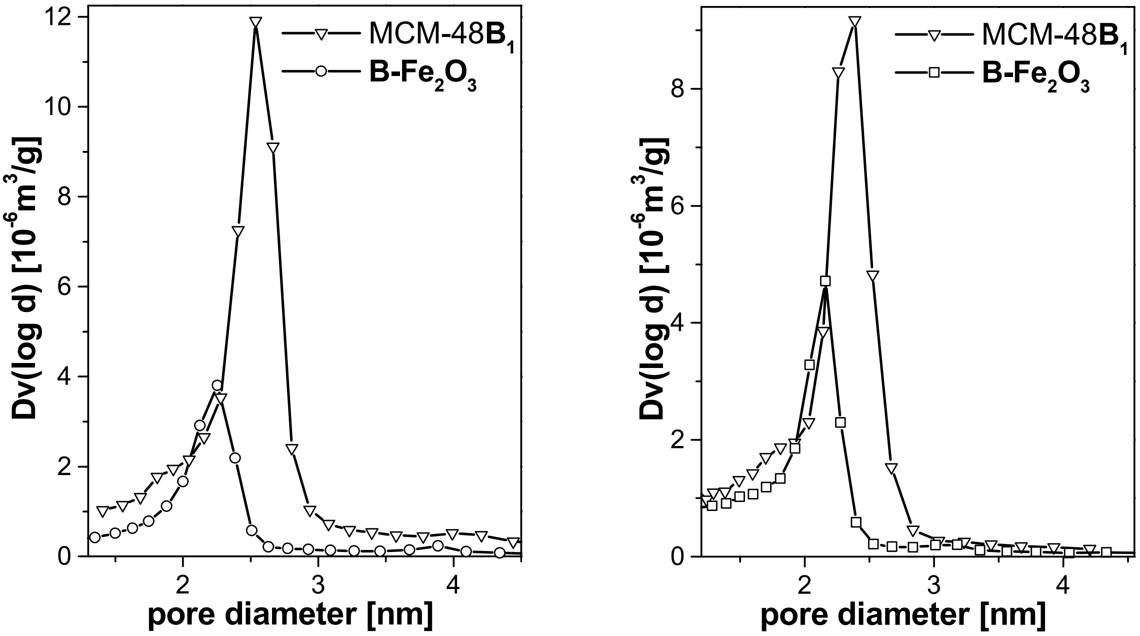

*Figure 4-18: BJH pore diameter distributions (Dv(logd) ≡ dV/d(log D)) for: (left) host-guest compound **B_1-Fe_2O_3** and pristine MCM-48**B_1** silica; (right) host-guest compound **B_1-Fe_2O_3** and pristine MCM-48**B_1** silica.*

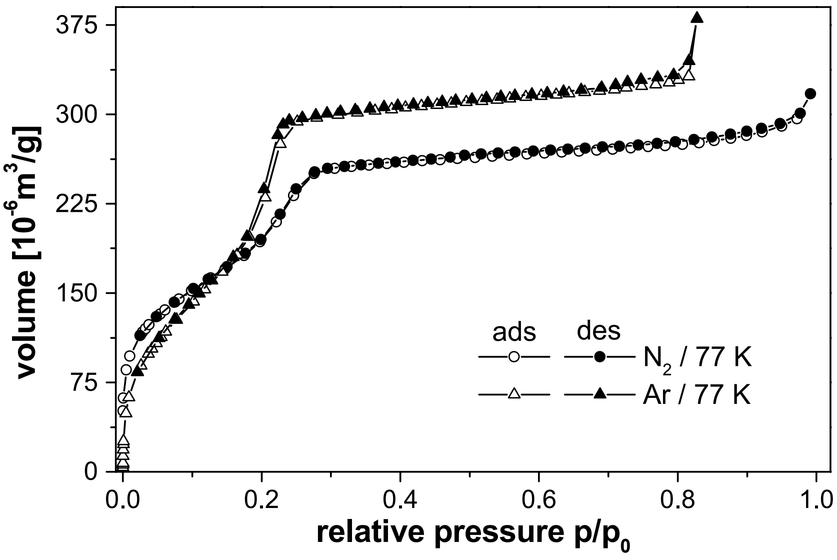

*Figure 4-19: Nitrogen physisorption in the host-guest compound **B_1-Fe_2O_3** at 77 K and 87 K (Enlargement of the physisorption isotherm up to relative pressure of ca. 0.4).*

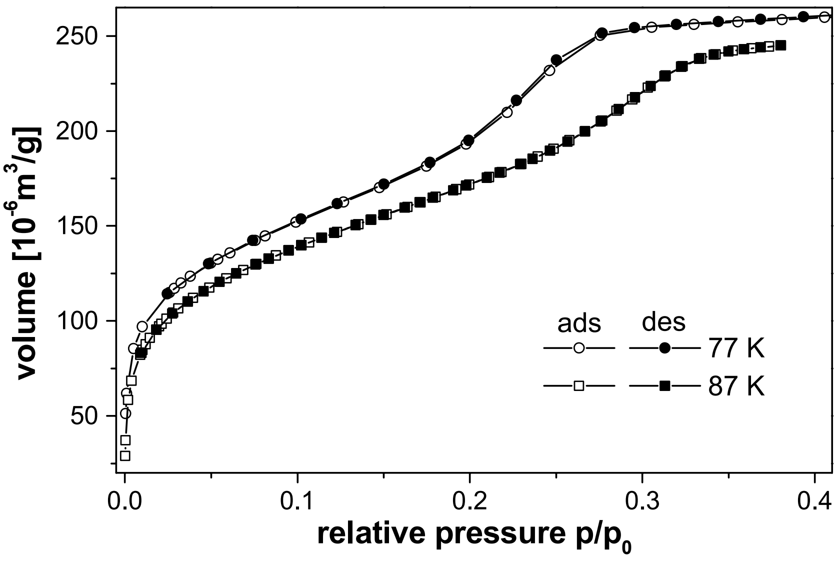

*Figure 4-20: Comparison of nitrogen and argon physisorption behavior (77 K) in the host-guest compound **B_1-Fe_2O_3**. In case of the Ar isotherm p_0 represents the saturation pressure of the undercooled liquid argon.*

higher temperature (87 K) the relative pressure for pore filling is shifted to higher values and the adsorbed amount is smaller in comparison to 77 K. This behavior is expected from classical theories of pore condensation and from the fact that the density of the capillary liquid decreases slightly with increasing temperature.

A comparison between the physisorption and pore condensation behavior of argon and nitrogen in **B_1-Fe_2O_3** at 77 K is made in Figure 4-20. For the argon isotherm at

77 K the saturation pressure of the undercooled liquid was taken as a reference (instead of the solid) in order to compare with the nitrogen isotherm at 77 K. Figure 4-20 shows that the adsorbed amount for nitrogen is higher at lower pressures, but then the physisorption isotherms cross at a relative pressure p/p_0 ca. 0.15 due to the onset of pore condensation for the Ar/**B_1-Fe_2O_3** system. The pore filling step for N_2/**B_1-Fe_2O_3** occurs at a slightly higher relative pressure. The argon isotherm reveals a much more pronounced pore condensation step and the adsorbed amount corresponding to the plateau of the physisorption isotherm is higher than for the nitrogen isotherm, due to the smaller molecule size and the higher liquid density of argon as compared to nitrogen. For the argon physisorption isotherm at 77 K even a small hysteresis loop is resolved, which disappears at 87 K, as shown in Figure 4-21, where argon and nitrogen physisorption behavior at 87.4 K is shown up to a relative pressure of ca. 0.4. Similar to the isotherms at 77 K the argon isotherms reveal a much sharper pore filling step; a crossing of the nitrogen and argon physisorption isotherms occurs at a relative pressure of p/p_0 = ca. 0.22.

While for argon and nitrogen physisorption isotherms at 87 K hysteresis is not observed anymore, the appropriate krypton physisorption isotherm on **B_1-Fe_2O_3** (Figure 4-22) reveals a clear hysteresis loop in agreement with the krypton isotherms measured at the same temperature for pristine MCM-48 silica materials. The steep increase of the

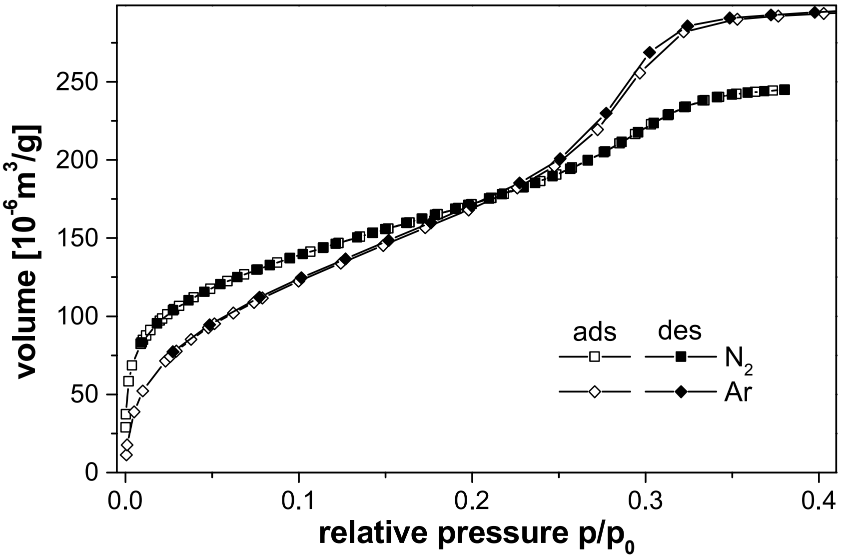

*Figure 4-21: Comparison of nitrogen and argon physisorption behavior (87 K) in the host-guest compound **B_1-Fe_2O_3** (enlargement of the physisorption isotherm up to relative pressure region of ca. 0.4).*

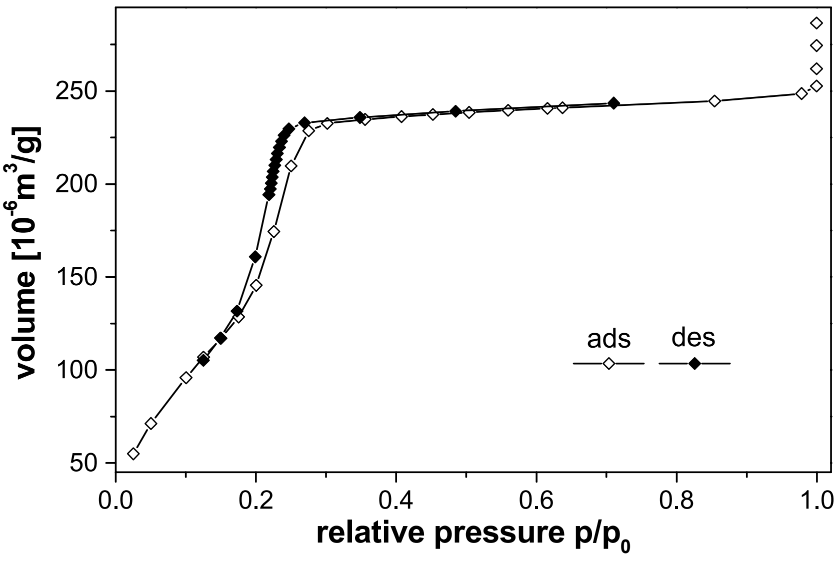

Figure 4-22: Krypton physisorption (87 K) in the host-guest compound $\boldsymbol{B_1\text{-}Fe_2O_3}$*. The chosen* p_0*-value is the saturation pressure of solid krypton at 87 K.*

krypton physisorption isotherm at p/p_0 ca. 1 (p_0 is the saturation pressure of solid krypton) indicates the solidification of bulk krypton.

As discussed in section 3.1.2 the different behavior of nitrogen, argon and krypton at 87 K reflects different thermodynamic states of the pore fluid compared to the bulk fluid. In summary, it can be stated that the physisorption and phase behavior of nitrogen, argon and krypton in MCM-48 silica/iron(III) oxide host compound is qualitatively similar to the behavior observed in pristine MCM-48 silica materials. The results indicate that the mesoporous host-structure is still intact in $\mathbf{B_1\text{-}Fe_2O_3}$, accompanied by a reduction of the pore width, which, together with results from HRTEM, EDS and XAS, is a good indication for a coating of the inner surface of the silica walls.

4.5 Conclusions

Physisorption with various adsorptives at different temperatures is a very powerful tool for the investigation of mesoporous materials of MCM-41 and MCM-48 silica type and surface modified nanostructured host/guest compounds.

A systematic study on the physisorption and phase behavior of nitrogen, argon and krypton at 77 K and 87 K was performed for different, highly ordered pristine mesoporous MCM-48 silica materials and for a MCM-48 silica/iron(III) oxide host-guest compound with pore diameter < 4 nm. Different methods (BJH, SF, Gurvich) were applied for pore size analysis of pristine MCM-48 silica; the obtained values for the pore volumes and diameters are in reasonable good agreement with each other.

Pore condensation is found to be more pronounced for argon physisorption isotherms obtained at 87 K as compared to nitrogen physisorption isotherms at 77 K on the same MCM-48 silica material. Hence, the argon physisorption at 87 K data may be better suited for pore size analysis of M41S materials, which consist of relatively small mesopores.

Although an appropriate pore model exists for the MCM-48 silica material with respect to cylindrical pores – which is comparable to the model for the MCM-41 type adsorbents – the calculation of pore size distributions with the NLDFT method is still not established. Taking this into account, it is reasonable to apply the BJH formula to our mesoporous M41S phases, knowing that this well-established method underestimates the pore size by ~ 1.0 nm. Nevertheless, it allows the determination of relative changes of pore size distributions. The application of other methods which correct this underestimation does not seem to be appropriate as these methods (see also Chapter 1.2.1) give no advantage in the estimation of an absolute value in comparison to the BJH method. All these methods only allow to compare mesoporous materials to each other, but the BJH method can be applied by all commercially available physisorption computer programs.

The physisorption results on the mesoporous MCM-48 silica and the controlled-pore glass indicate that for silica materials argon pore condensation at 77 K ($T - T_R = -6.5$ K) can only be observed in pores of diameters < ca.12 nm. Accordingly argon physisorption isotherms at liquid nitrogen temperature can only be used for mesopore size analysis, as long as all pores of the porous material are smaller than ca. 12 nm.

In MCM-48 silica phases the occurrence of physisorption hysteresis depends on temperature and pore size, i.e. the thermodynamic states of pore fluid and bulk fluid. Nitrogen physisorption isotherms at 77 K on all materials do not reveal any physisorption hysteresis, whereas in case of argon physisorption at 87 K a small hysteresis loop could be detected for a pore diameter D_p,N_2(BJH) of ca. 2.8 nm (MCM-48$\mathbf{C_1}$), but not for pores smaller than 2.52 nm. For argon adsorption at 77 K pore condensation and hysteresis is resolved for all MCM-48 silica materials studied here, even for a pore diameter of ca. 2.1 nm (MCM-48$\mathbf{A_1}$). The width of hysteresis loops decreases with decreasing pore diameter, in accordance with the expectation that the fluid confined to the smaller pores of MCM-48$\mathbf{A_1}$ silica may be closer to pore criticality as the fluid in the wider pores of MCM-48**C$_1$** silica.

Argon physisorption isotherms at 77 K and 87 K in MCM-48**C$_1$** silica also show that the width of the hysteresis loop decreases for a given material with increasing temperature as expected from theoretical predictions [89]. The difference in the occurrence of hysteresis for nitrogen and argon at 77 K can also be explained as a consequence of the lower reduced temperature T/T_c of argon compared to nitrogen, where T_c is the critical temperature of the bulk fluid (T/T_c(Ar) = 0.51; T/T_c(N_2) = 0.61). The observed argon physisorption hysteresis loops in MCM-48 silica materials are of type H1, indicating that network effects are not dominant for physisorption hysteresis in the MCM-48 silica studied here, despite the fact that MCM-48 silica consists of a unique three-dimensional pore network.

The occurrence of pore condensation and hysteresis in argon physisorption isotherms at 77 K for MCM-48 silica with BJH pore diameter < 3 nm reveals that the (*quasi*) triple point of the pore fluid is shifted by at least 6.5 K to lower temperature as compared to the triple point temperature of the bulk fluid. In contrast, argon physisorption isotherms at 77 K in the much wider pores of controlled-pore glass (16nm) do not show any pore condensation and hysteresis, indicating that in such wide pores the pore condensation line does not extend down to this temperature for pressures up to the corresponding bulk sublimation pressure.

Phase transitions and pronounced physisorption hysteresis of type H1 are also found for krypton physisorption at 87 K in MCM-48 silica, i.e. ca 28.5 K below the bulk triple point temperature. As in case of argon physisorption (77 K) the width of the hysteresis loop decreases with decreasing pore diameter, but is still observable for a BJH pore diameter as small as 2.1 nm.

The physisorption and pore condensation behavior of nitrogen and argon within the mesopores of MCM-48 and MCM-41 silica were investigated. Both materials show reversible pore condensation without hysteresis in the nitrogen physisorption. The pore size distribution and mean pore diameters for the MCM-48 and MCM-41 silica are comparable in sharpness and size. The argon physisorption data obtained for 87 K and 77 K exhibit pore condensation with hysteresis. For both temperatures the hysteresis loop obtained for the MCM-48 silica material is significantly smaller in comparison to the hysteresis loop of the MCM-41 silica material.

For the first time the NLDFT pore size calculation for nitrogen and argon physisorption isotherms was applied to highly ordered mesoporous MCM-48

(MCM-48**D**) silica with BJH pore diameters above 3 nm. Although the MCM-48 silica phase consists of an interconnected pore structure, the results show clearly that the desorption branch of the hysteresis loop reflects the equilibrium phase transition. This observation confirms that hysteresis even in interconnected pore systems is indeed associated with the development of metastable fluid states associated with the pore condensation process.

The analysis of nitrogen and argon physisorption isotherms at 77 K and 87 K indicates that the impregnation of a pristine MCM-48 silica phase with iron(III) oxide has indeed led to a coating of the inner pore walls. In addition, the observed physisorption and pore condensation behavior of nitrogen, argon and krypton in MCM-48 silica/iron(III) oxide was found to be qualitatively similar as for pristine MCM-48 silica materials, which indicates that the mesoporous host structure is still intact.

5 Nanostructured host/guest compounds

5.1 Iron oxide within mesoporous silica

5.1.1 Series *Fe*-8A

Three impregnation/calcination cycles were performed in this series to yield higher loadings of iron oxide within the mesoporous MCM-48 silica host. The amount of iron oxide loaded into the channels of the mesoporous host is given in Table 5.1.

5.1.1.1 Powder X-ray diffraction

With every impregnation/calcination cycle the intensity of the X-ray reflections decreases accompanied by a slight shift to larger values 2 θ and smaller *d* spacings, respectively (Figure 5-1). The latter effect can be attributed to the influence of the

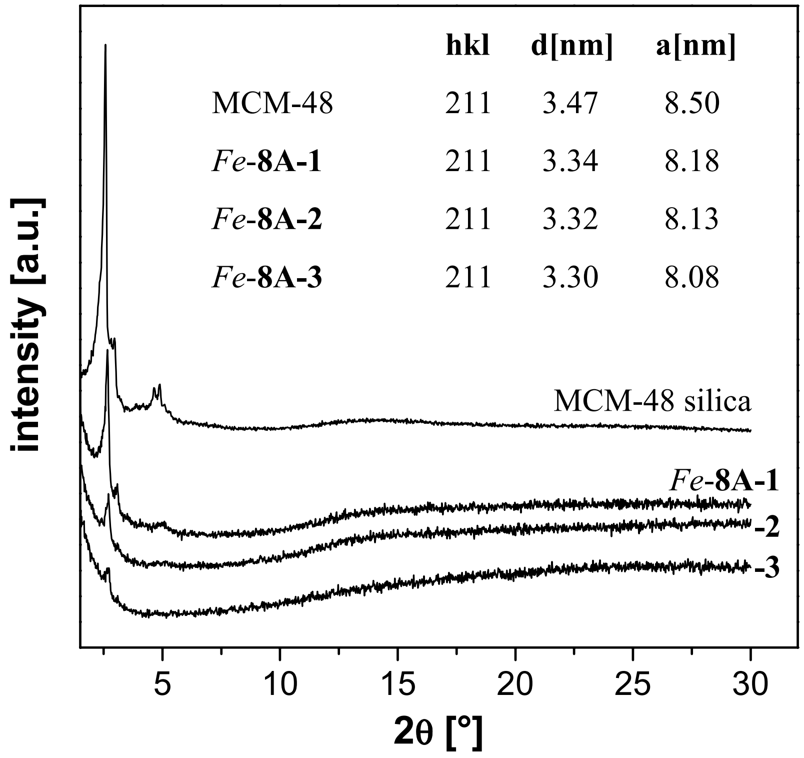

	hkl	d[nm]	a[nm]
MCM-48	211	3.47	8.50
Fe-**8A-1**	211	3.34	8.18
Fe-**8A-2**	211	3.32	8.13
Fe-**8A-3**	211	3.30	8.08

*Figure 5-1: P-XRD patterns of MCM-48 silica material and the respective host/guest compounds Fe-**8A-1**, **-2**, and **-3**. The d spacing of the (211) peak is listed together with the corresponding lattice constant a.*

impregnation/calcination cycles, which probably increase the degree of connectivity within the silica walls. As a result, this leads to a small contraction of the overall host structure, which is consistent with literature reports that the mesoporous structure contracts upon calcination or treatment in acidic solutions [188]. The strong reduction of the X-ray peak intensities corresponds to increasing destructive interferences by subsequent filling of the pores with the iron oxide. After each treatment with the iron(III) nitrate solution, all *hkl* reflections are extinct, but reappear after drying and in-situ formation of the haematite in the course of calcination. In general, the introduction of scattering material into the pores leads to an increased phase cancellation between scattering from the wall and the pore regions and therefore to reduced scattering intensities for the Bragg reflections [189-191]. First theoretical models have shown that this phase relationship is very sensitive and that the degree of cancellation is mainly determined by the scattering contrast between the framework walls and the pores [192]. This effect corresponds to the raised intensities of the M41S phases after the removal of the structure-directing agent (see Chapter 3.1). Apart from the typical MCM-48 silica reflections, no additional peaks are observed, indicating that no crystalline iron oxide phase has been formed outside the pore structure. With an average pore diameter of 2.8 nm iron oxide particles synthesized within the pores would be too small to give X-ray reflections. The drying procedure has to be considered as the most sensitive step in the synthesis of the host/guest compound. Best results are obtained by running the drying process at room temperature under vacuum. Every attempt to use elevated temperatures (above 373 K) under ambient pressure leads to the premature formation of haematite outside the pores as proved by XRD (not shown).

5.1.1.2 Nitrogen Physisorption

Figure 5-3 shows the amount of nitrogen physisorbed at 77 K versus the relative pressure for the parent MCM-48 silica material as well as for the host/guest compounds received after the first to third impregnation/calcination cycle. All isotherms are of type IV, typical of mesoporous materials [3] A well-defined step occurs at approximately $p/p_0 = 0.2\text{-}0.3$, associated with the filling of the mesopores due to capillary condensation. Depending on the number of impregnation/calcination cycles, the amount of physisorbed nitrogen decreases accompanied with a shift of the inflection point of the step to smaller values of p/p_0. Both effects can be attributed to the introduction of the iron oxide nanoparticles into the mesopores. The reduced amount of physisorbed

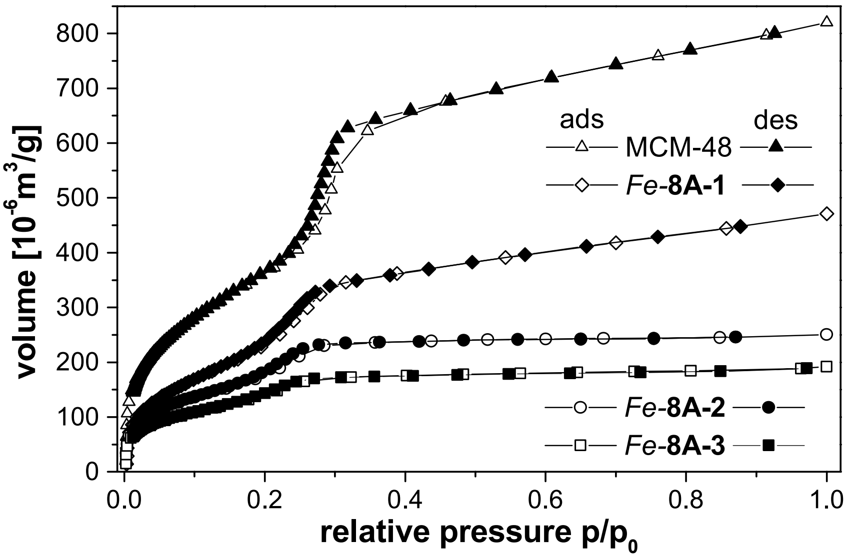

*Figure 5-2: Nitrogen physisorption isotherms of MCM-48 silica and the host/guest compounds Fe-**8A-1**, **-2**, and **-3**.*

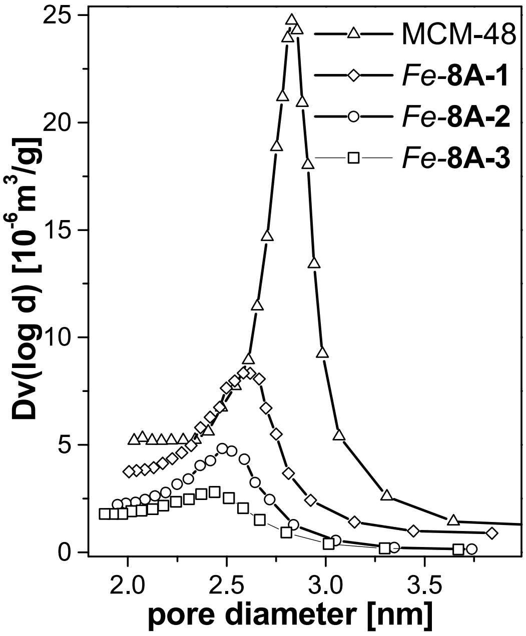

*Figure 5-3: BJH pore size distributions of the compounds Fe-**8A-1**, **-2**, and **-3**.*

nitrogen is caused by a smaller surface area, while the occurrence of the step at lower relative pressure is indicative of smaller pore sizes. At this point it must be kept in mind that the introduction of the heavy iron oxide itself already leads to a reduction of the surface area of the mesoporous silica matrix (molecular weight: Fe_2O_3, 159.69; SiO_2, 60.08). The determined BET surface, the content of Fe_2O_3 together with the intrinsic reduction of the specific surface due to the inserted Fe_2O_3, as well as the calculated mean pore radius are listed in Table 5-1. Due to a better mobility of iron nitrate within

*Table 5-1: Iron content, BET surface area, reduction of the BET surface due to the introduction of iron oxide and mean value of the pore diameter distribution of the samples of the series Fe-**8A**.*

sample	Fe_2O_3 content [weight %]	A_s(BET) / reduction by F_2O_3 weight [m^2/g]	mean pore diameter [nm]
MCM-48 silica	-	1376 / -	2.82
Fe-**8A-1**	19.6	866 / 270	2.62
Fe-**8A-2**	32.1	681 / 442	2.52
Fe-**8A-3**	42.5	509 / 585	2.44

the pores at the beginning, the largest reduction of the specific surface as well as of the pore radius occurs with the first impregnation/calcination cycle. With the in-situ formation of the iron oxide, the step of the isotherms at $p/p_0 = 0.2\text{-}0.3$ is slightly broadening, representing a less uniform remaining pore size, which is probably caused by a small inhomogeneous filling of the pores. Nevertheless, all samples still show mesoporosity, which is indicative of a coating of the inner surface of MCM-48 silica rather than a complete filling of the pores.

5.1.1.3 X-ray Absorption Spectroscopy

X-ray absorption spectroscopic measurements at the Fe K-edge were carried out in order to obtain structural information on the iron coordination within the iron oxide nanoparticles. The energy position of the absorption edge of the nanocomposites of the *Fe*-**8A** series appear at the same position as that of haematite, indicating a valence shift characteristic of iron(III); no iron(II) is formed during the calcination procedure. In contrast to crystalline haematite, the XANES (X-ray absorption near-edge structure) of the nanostructured iron oxide samples are more smeared out and broadened (see Figure 5-4), an effect well-known from nanostructured materials with some kind of structural disorder [193]. All spectra show a small pre-edge peak caused by dipole-allowed electronic transitions. The relatively small intensity is an indication of octahedrally coordinated iron, which is expected in case of haematite nanoparticles within the pores. The introduction of iron into the silica wall would basically lead to a tetrahedral coordination and, as a result, to a much higher peak intensity [146]. In the following the focus is set on the analysis of the EXAFS (extended X-ray absorption fine structure) region. After conventional data analyses, i.e. energy calibration, background subtraction, and normalization of the edge-jump, the k^3-weighted data were Fourier transformed using a Bessel window ranging from $k = 3$ to 15 $Å^{-1}$. Figure 5-5 and Figure 5-6 show the EXAFS oscillations $\chi(k)\cdot k^3$ and the corresponding Fourier transforms (FTs). In case of Figure 5-5, the amplitude of the EXAFS oscillation of bulk haematite is multiplied by a factor of 0.3, which already indicates the strong intensity reduction in the back-scattering amplitudes for the host/guest compounds due to the small particle sizes and the occurrence of a certain degree of structural disorder. The loss of long-range order becomes even more visible in the FTs. While the radial distribution function of the haematite shows peaks at distances up to 7 Å, the FTs of the iron oxide nanoparticles indicate only the Fe-O and Fe-Fe coordination shells up to 3.6 Å, which are divided into subshells due to distortion of the FeO_6 octahedra and different ways they are linked together [194]. While the Fe-O shells are almost unchanged, the Fe-Fe shells (> 2 Å) are slightly shrunk and strongly reduced in intensity which is caused by the reasons mentioned above. The further investigations were concentrated on the Fe-Fe shells to obtain information on the range of structural order within the iron oxide nanoparticles.

Bulk haematite, which is isostructural with corundum, can be described as consisting of hcp arrays of oxygen ions with two-thirds of the octahedral sites being filled with

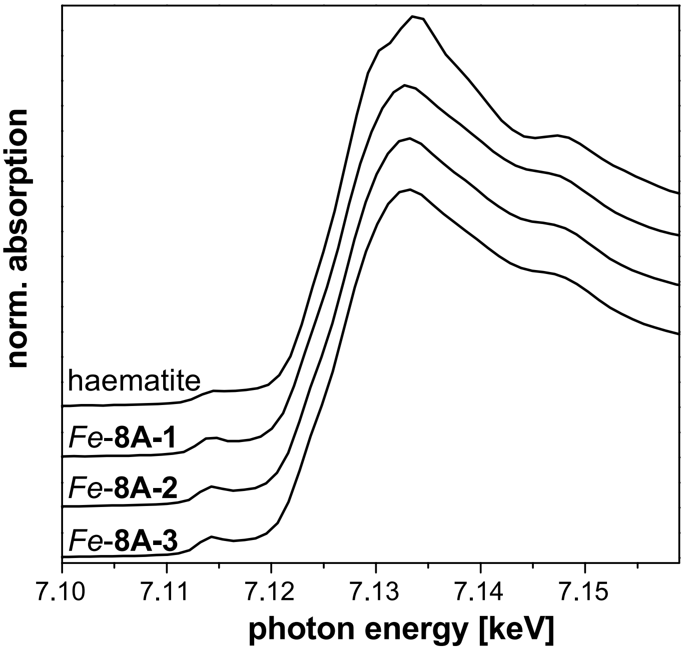

*Figure 5-4: Normalized Fe K-XANES spectra of the three Fe-**8A** host/guest compounds and of a bulk sample of haematite.*

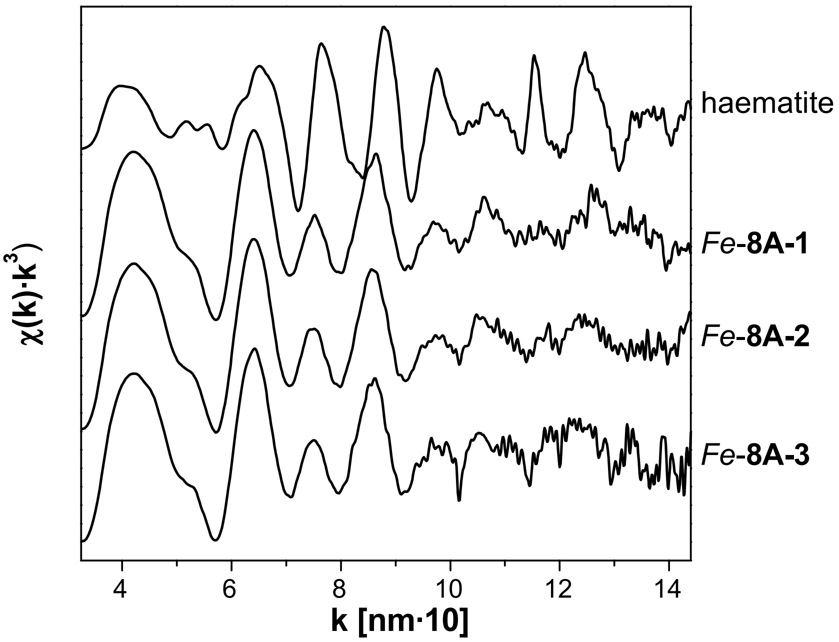

*Figure 5-5: Fe K-edge EXAFS oscillations $\chi(k)\cdot k^3$ of the three Fe-**8A** host/guest compounds and of bulk haematite. In case of haematite the amplitude is multiplied by a factor of 0.3.*

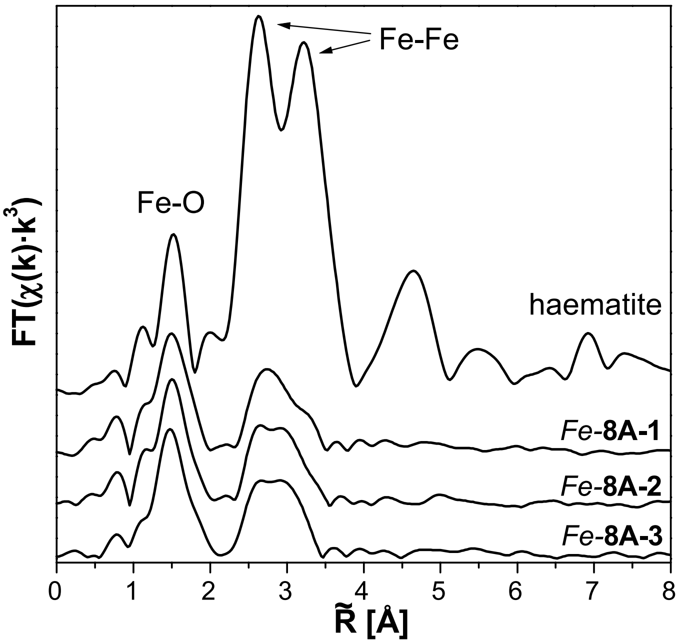

*Figure 5-6: Fourier transforms of the Fe K-edge EXAFS oscillations $\chi(k)\cdot k^3$ of the three Fe-**8A** host/guest compounds and bulk haematite.*

Fe(III) [195]. The arrangement of cations produces pairs of FeO_6 octahedra. Each octahedron shares edges with three neighboring octahedra in the same plane and one face with an octahedron in an adjacent plane. Apart from the face-shared octahedra, additional corner-shared octahedra exist between the layers. Depending on the type of linkage between the octahedra, the Fe-Fe distances differ in the following sequence: face-shared < edge-shared < corner-shared. In case of crystalline haematite [196] four different Fe-Fe coordination shells exist within the range of 2.9-3.7 Å (Table 5-2). While the nearest (2.90 Å) and next-nearest (2.97 Å) neighbor shells are formed by face- and edge-shared octahedra, respectively, the other two (3.36 and 3.71 Å) are due to a corner-shared linkage. For further data analyses the Fe-Fe coordination shells were extracted by Fourier filtering using a Bessel window ranging from $R = 2.3\text{-}3.5$ Å. Refined structure parameters were obtained by fitting the obtained backtransforms (BTs) in *k*-space within the range of $k = 3.0\text{-}14.8$ Å^{-1} using three shells representing three different Fe-Fe linkages. In case of bulk haematite, four shells were used. To keep the number of independent parameters as low as possible during the refinements, some conditions with respect to the variables had to be made: (1) the amplitude reduction

*Table 5-2: Refined structure parameters of the Fe-Fe coordination shells, extracted from the Fe K-EXAFS of series Fe-**8A** host/guest compounds, and bulk haematite.*

sample:	*Fe*-**8A-1** ($\Delta E_0 = 3.5$)	*Fe*-**8A-2** ($\Delta E_0 = 3.9$)	*Fe*-**8A-3** ($\Delta E_0 = 3.2$)	haematite ($\Delta E_0 = -1.6$)	haematite (s.c.) [196]
N	-	-	-	0.91	1
R [Å]	-	-	-	2.91	2.90
$\Delta\sigma^2$ [Å^2]	-	-	-	0.0025	-
N	0.91	0.98	1.11	2.95	3
R [Å]	3.00	2.99	2.99	2.97	2.97
$\Delta\sigma^2$ [Å^2]	0.004	0.003	0.004	0.0039	-
N	0.87	1.12	1.19	2.80	3
R [Å]	3.12	3.13	3.12	3.37	3.36
$\Delta\sigma^2$ [Å^2]	0.0036	0.003	0.004	0.0034	-
N	0.45	0.51	0.50	3.12	6
R [Å]	3.48	3.46	3.44	3.70	3.71
$\Delta\sigma^2$ [Å^2]	0.0034	0.004	0.0036	0.002	-

Abbreviations: N = coordination number; R = bond length; $\Delta\sigma^2$ = Debye-Waller factor; ΔE_0 = energy shift; s.c. = single-crystal data.

factor was always kept constantly one; (2) the energy shift ΔE_0 was the same for each shell; (3) the Debye-Waller factors were constrained within the range of 0.002-0.0045 Å^2.

In general, the number of independent degrees of freedom in a spectrum is given by $N_{ind} = (2\Delta k \Delta R/\pi)+2$ [197]. In all cases, the number of parameters used in the fits was significantly smaller than the calculated value of N_{ind}.

To check the accuracy of the least-squares refinements, the data of bulk haematite were fitted too. The data were treated in the same way as the data of the samples *Fe*-**8A-1** to *Fe*-**8A-3**. The received results are in good agreement with the values obtained from single-crystal XRD data as listed in Table 5-2 (page73). Comparison of

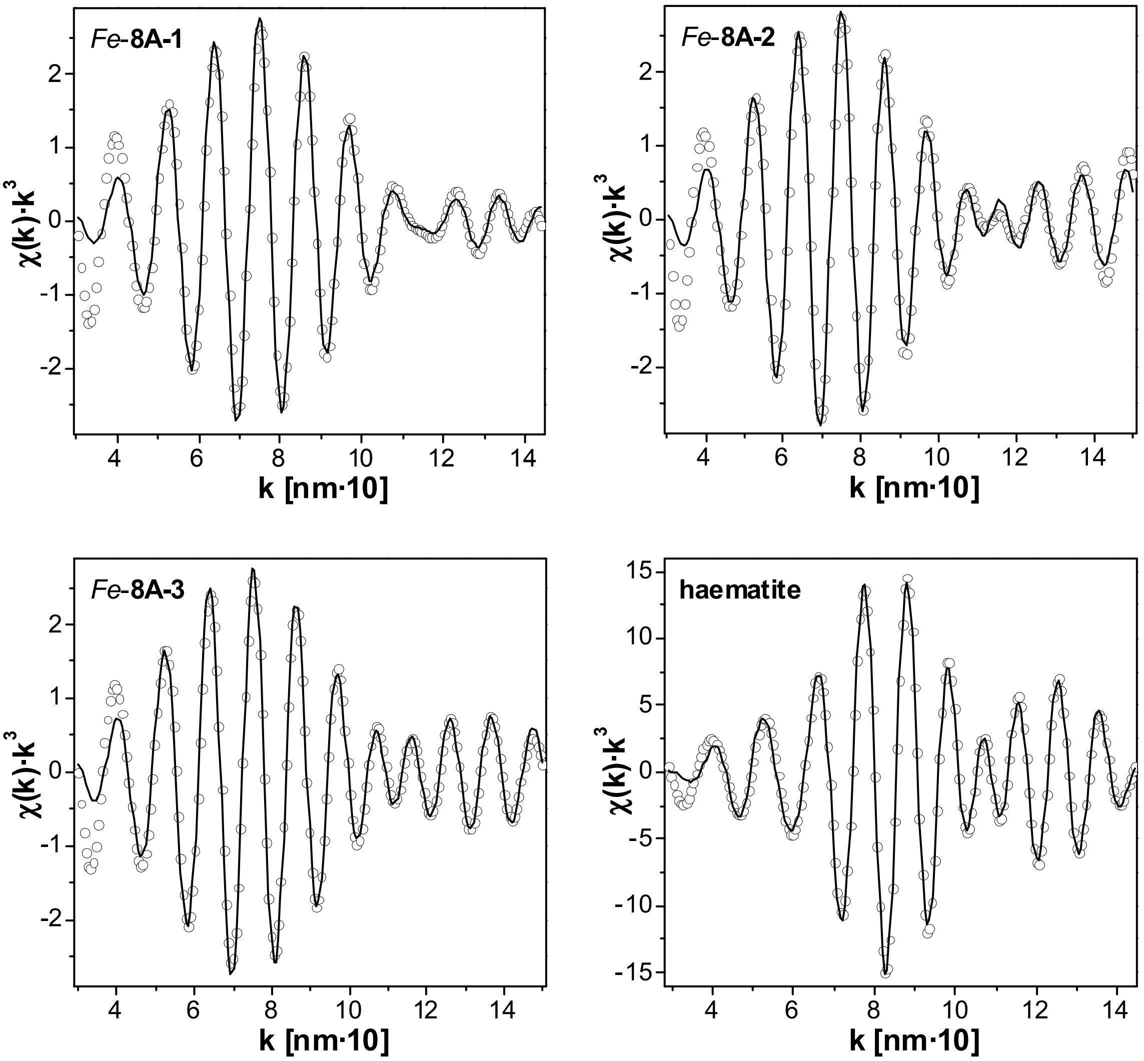

*Figure 5-7: Back-transforms (circles) of the Fe-Fe coordination shells (ΔR = 2.3-3.5 Å) shown in Figure 5-6 and the results of the least-squares refinements (solid lines) of the three Fe-**8A** host/guest compounds and of a bulk sample of haematite.*

the X-ray absorption spectroscopic data of the three samples of the *Fe*-**8A** series with goethite (α-FeOOH, not depicted)– which is strongly related to haematite – excludes the major formation of the latter corresponding oxide hydroxide [194,195]. The reduced coordination number of the Fe-Fe shell at 3.71 Å is probably caused by a slight structural disorder. Figure 5-7 shows the described BTs (Fe-Fe coordination shells) of each compound together with the results of the least-squares refinements. The differences between the experimental and fitted data are marginal. Small deviations at low k-values can probably be attributed to the restricted parameter of the energy shift ΔE_0 (see above). This parameter has its strongest influence at low *k*-values [198]. In contrast to bulk haematite, the first Fe-Fe shell of the nanoparticles appears at 3 Å, a distance which can only be formed by edge-shared octahedra. Even after three impregnation/calcination cycles, the host/guest compound does not contain any face-shared FeO_6 octahedra. In addition, the other two Fe-Fe shells of the nanoparticles occur at distances of ~ 3.12 and 3.46 Å, which corresponds to an edge- and corner-shared linkage. With an increasing number of impregnation/calcination cycles, the third Fe-Fe shell becomes shorter, a phenomenon which can probably be attributed to a tempering effect due to the multiple heat treatments. The coordination numbers for each shell are relatively small as compared to those in haematite, indicating the small size of the iron oxide nanoparticles within the mesopores of MCM-48 silica.

5.1.1.4 Electron Microscopy

The *Fe*-**8A-2** compound (two impregnation/ calcination cycles) was studied by electron diffraction (ED), high-resolution transmission electron microscopy (HRTEM) and energy dispersive qualitative microanalysis (EDS). The results are compared to the corresponding original MCM-48 silica material which was discussed in Chapter 3.2.

Very similar selected area electron diffraction patterns as those observed for the pristine MCM-48 silica material are obtained for the iron oxide-doped material. The zone axis patterns ⟨100⟩, ⟨111⟩, and ⟨110⟩ are presented in Figure 5-8. The forbidden reflections such as {200} and {110}, which appear due to multiple diffraction, are the same, but are less visible than in the undoped material (see Figure 3-10). The space group of the structure is still $I4_1/a\bar{3}2/d$, and there is no significant change in the lattice parameter. However, the fact that the diffraction patterns are less well-pronounced and that higher order reflections are less prominent points to some disorder in the structure.

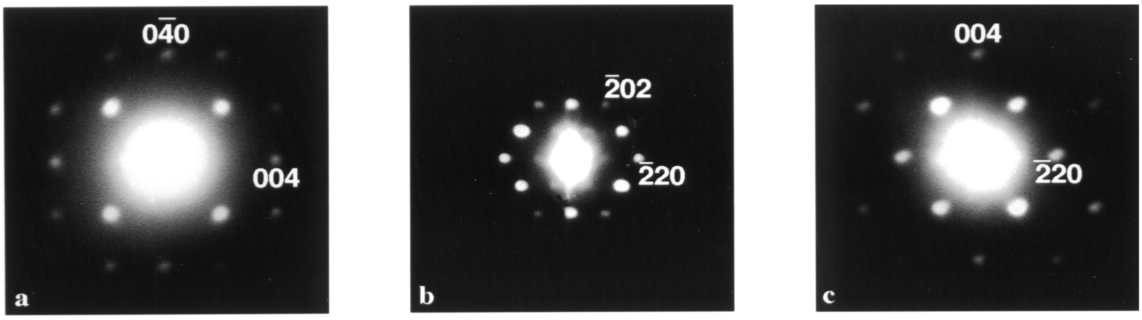

*Figure 5-8: Selected area electron diffraction patterns (SAED) the host/guest compound Fe-**8A-2**: (a) ⟨100⟩, (b) ⟨111⟩, and (c) ⟨110⟩ zone axis patterns.*

EDS measurements indicate that most of the iron oxide has indeed been incorporated into the mesoporous silica phase. However, since no superstructure reflections or any extra diffuse intensity out of the Bragg reflections are observed (see above), it can be assumed that the iron oxide is randomly distributed within the structure.

High-resolution images corresponding to the ⟨111⟩ and ⟨110⟩ zone axis are shown Figure 5-9 and Figure 5-10, respectively. At first sight, the high-resolution images look very similar to the ones recorded for the pristine material (see Figure 3-11b and c). However, closer inspection reveals intensity deviations and extra bright intensity within the pores (indicated by the arrows in Figure 5-10). However, not all pores show this contrast, indicating that the degree of iron oxide filling is not equivalent in all pores. Also, the filling of the pores is random, without any large structural order, eventual ordering would be readily observed by electron diffraction. This confirms the results obtained from the adsorption/desorption measurements. The intensity deviations and extra intensity within the pores are particularly visible on the images corresponding to the ⟨111⟩ and ⟨110⟩ zone axes and much weaker along other zone axes. A direct comparison between the ⟨111⟩ image corresponding to the MCM-48 pristine material (Figure 3-11b) and the one corresponding to the doped material (Figure 5-9) may be made since the defoci of both images are very similar. Extra intensity modulations have never been observed for the pristine material; together with the detection of Fe and O within the crystallites, this is very strong evidence for the hypothesis that the extra intensity is associated with the Fe_2O_3 doping.

The EDS analysis shows, apart from the presence of Si, O, C, Fe, and sometimes traces of Pt. The amount of Fe varies from one grain to the other, indicating that the Fe content is inhomogeneous. It should be noted that precipitation of Fe-O particles has also been detected, but only as small impurities. After three impregnation/calcination cycles the general aspect remains but more Fe-O precipitation is observed.

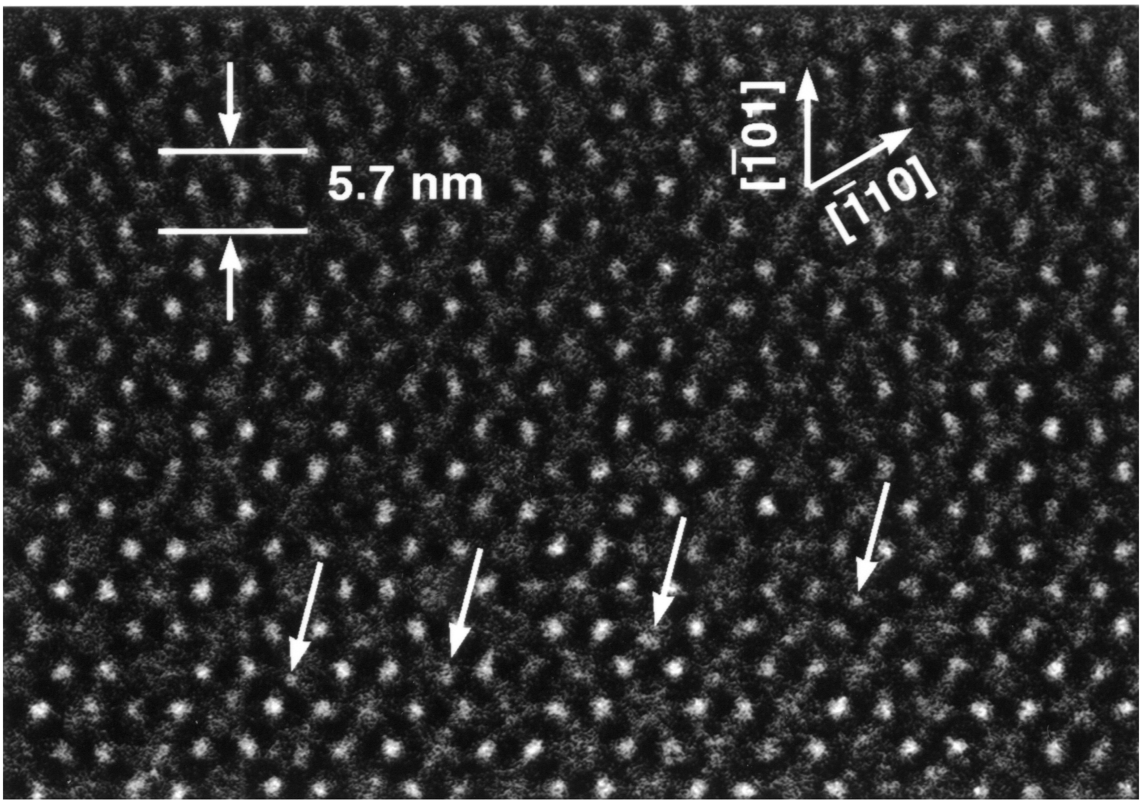

*Figure 5-9: HRTEM of Fe-**8A-2** corresponding to the ⟨111⟩ zone axis.*

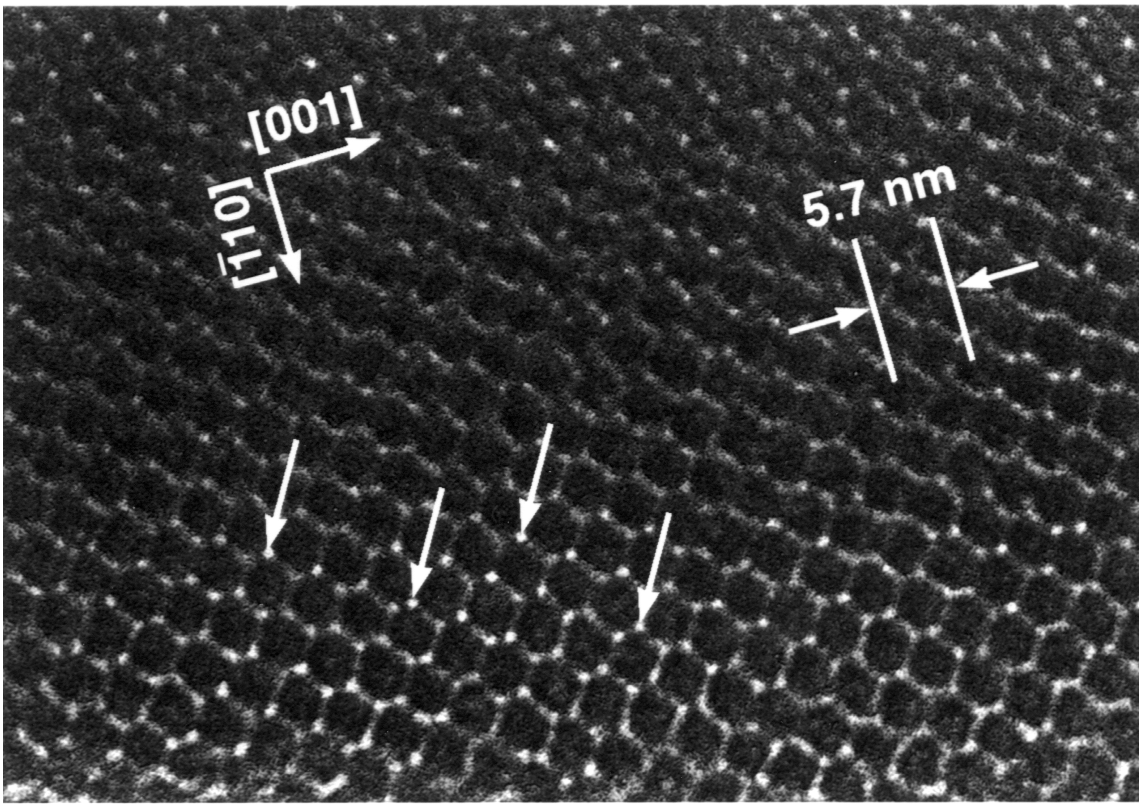

*Figure 5-10: HRTEM of Fe-**8A-2** corresponding to the ⟨110⟩ zone axis.*

5.1.2 Series *Fe*-**8B** and *Fe*-**1A**

In contrast to the synthesis procedure described for the *Fe*-**8A** series (cf. section 5.1.1) the *Fe*-**8B** and *Fe*-**1A** series were synthesized by one single impregnation and calcination procedure. Various iron contents were achieved by impregnation with iron nitrate solution of different concentrations: 0.07 mol/l: *Fe*-**8B-1** / *Fe*-**1A-1**, 0.37 mol/l: *Fe*-**8B-2** / *Fe*-**1A-2**, 1.18 mol/l: *Fe*-**8B-3** / *Fe*-**1A-3**, and 4.87 mol/l: *Fe* **8B-4** / *Fe*-**1A-4**. The synthesis method was applied parallel on MCM-48 and MCM-41 silica to verify that it is practicable for both materials. The materials with the highest loading of iron oxide (*Fe*-**8B-4** and *Fe*-**1A-4**) were chemically reduced in order to investigate their reduction behavior and the changes of their magnetic properties.

5.1.2.1 Powder X-ray diffraction

Figure 5-11 and Figure 5-12 show the reduction of the typical X-ray reflections of the MCM-48 and MCM-41 silica materials after the impregnation with iron nitrate solutions and calcination. Increasing destructive interference by pore filling with rising amounts of iron oxide is visible (cf. section 5.1.1.1, page 67). A comparable reduction due to the filling of the mesopores with iron oxide is observed for the MCM-48 and MCM-41 host systems. While the *Fe*-**8B-1** and *Fe*-**1A-1** samples still show all reflections that were detected for the corresponding pristine silica (not depicted) the reduction grows significantly with increasing loading.

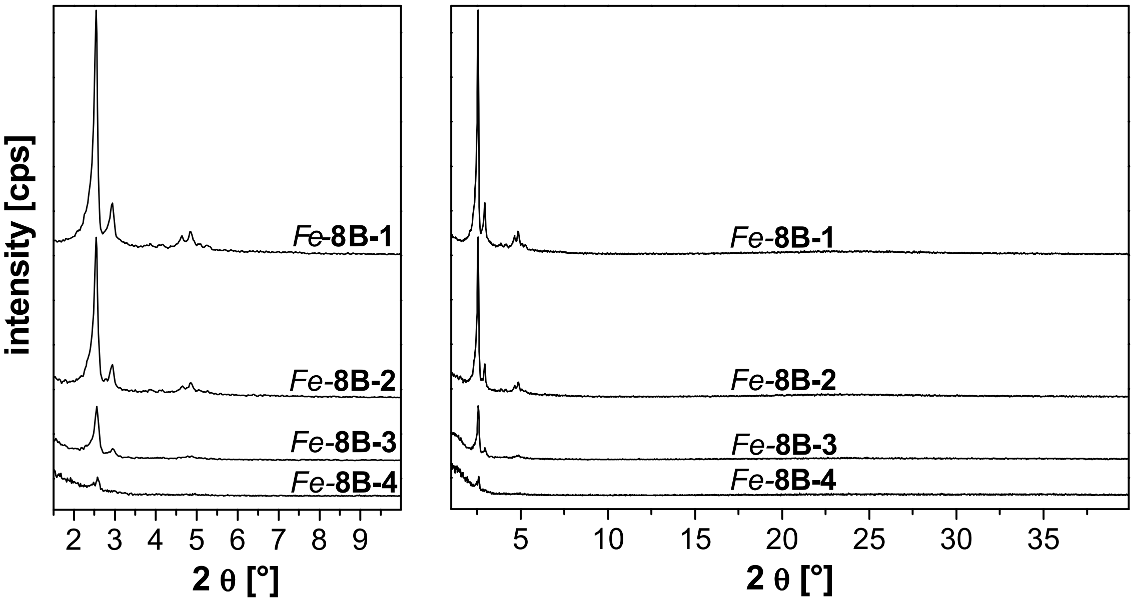

*Figure 5-11: P-XRD patterns of the nanostructured host/guest compounds of the Fe-**8B** series for the low angle region (left) and up to 40° 2 θ (right).*

Table 5-3 gives a comparison of the observed reflections for the pristine MCM-48 and MCM-41 silica and the corresponding host/guest compounds of the *Fe*-**8B** and *Fe*-**1A** series. For the materials with the highest loading of iron oxide (*Fe*-**8B-4** and *Fe*-**1A-4**) only the most intense reflection is left. Since more than one reflection is necessary to distinguish the phase correctly other methods have to be applied to prove that the structure of the mesoporous host systems are still intact (see 5.1.2.2).

Besides the typical MCM-48 and MCM-41 silica reflections, no additional peaks are observed in the higher 2θ range (Figure 5-11, right; Figure 5-12, right). This indicates that no crystalline iron oxide phase (e.g. haematite $d_{012}(30\%) = 3.69$ Å; $d_{104}(100\%) = 2.71$ Å; $d_{110}(70\%) = 2.52$ Å corresponding to $2\theta_{012} = 24.1°$; $2\theta_{104} = 33.0°$; $2\theta_{110} = 35.6°$) has been formed outside the pore structure. The results obtained from powder X-ray diffraction are the same as those obtained for the *Fe*-**8A** series (cf. section 5.1.1.1).

*Table 5-3: Observed P-XRD hkl-reflections as d-values [nm] for the pristine MCM-48 and MCM-41 silica materials and the corresponding iron oxide M41S host/guest compounds of the Fe-**8B** and the Fe-**1A** series.*

hkl-reflections	d_{211}	d_{220}	d_{321}	d_{400}	d_{420}	d_{332}	d_{422}	d_{431}
MCM-48 silica	3.49	3.02	2.29	2.15	1.92	1.83	1.75	1.69
Fe-**8B-1**	3.49	3.02	2.27	2.13	1.91	1.82	1.74	1.68
Fe-**8B-2**	3.48	3.01	2.29	2.14	1.89	1.82	-	-
Fe-**8B-3**	3.45	3.00	-	-	-	-	-	-
Fe-**8B-4**	3.41	-	-	-	-	-	-	-

hkl-reflections	d_{100}	d_{110}	d_{200}	d_{210}	d_{300}
MCM-41 silica	4.32	2.49	2.15	1.63	1.43
Fe-**1A -1**	4.26	2.46	2.13	1.61	-
Fe-**1A -2**	4.28	2.47	2.14	1.62	-
Fe-**1A -3**	4.22	2.44	2.12	1.60	-
Fe-**1A-4**	4.14	2.39	2.07	-	-

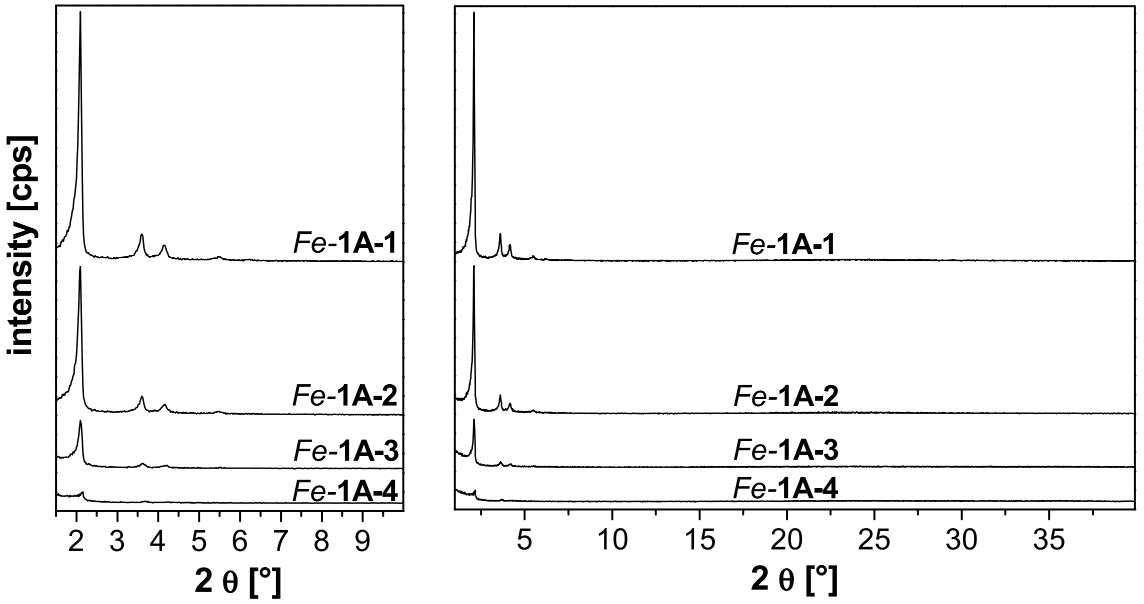

*Figure 5-12: P-XRD patterns of the nanostructured host/guest compounds of the Fe-**1A** series for the low angle region (left) and up to 2 θ = 40° (right).*

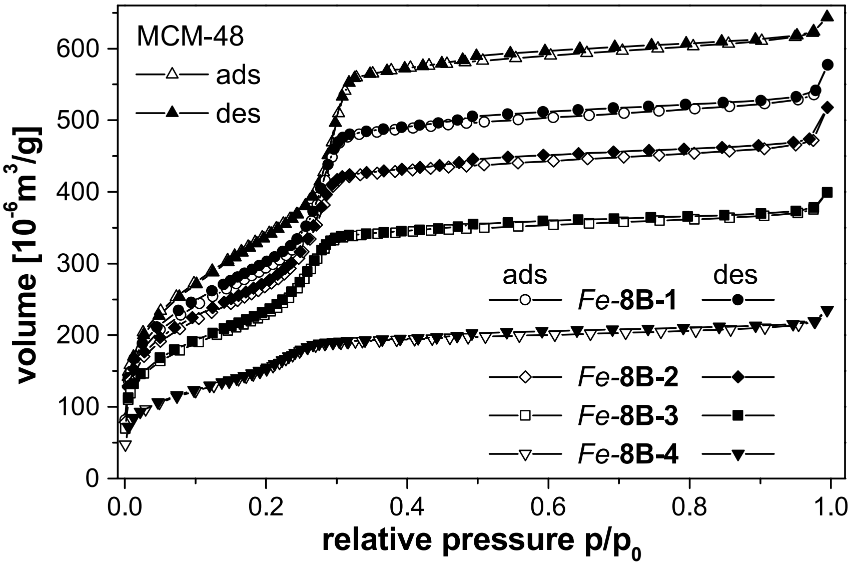

*Figure 5-13: Nitrogen adsorption/desorption isotherms (77 K) of the pristine MCM-48 silica material and the host/guest materials Fe-**8B-1**, **-2**, **-3**, and **–4**.*

5.1.2.2 Nitrogen physisorption

Figure 5-13and Figure 5-14 show the adsorption/desorption branches of the pristine MCM-48 and MCM-41 silica materials and the corresponding host/guest compounds of the *Fe*-**8B** and *Fe*-**1A** series. All materials show typical type IV isotherms (IUPAC classification [3]) as is expected for mesoporous systems. Between p/p_0 = 0.2-0.3 a well-defined step occurs, representing the spontaneous filling of the mesopores due to capillary condensation. The amount of physisorbed nitrogen decreases with increased amounts of iron oxide loaded within the mesopores. The inflection point of the respective steps is shifted to lower values of p/p_0 as expected for smaller pores.

The reduction of the mean pore diameter is also observed in the pore diameter distribution as depicted in Figure 5-15 for the *Fe*-**8B** series (left), the *Fe*-**1A** series (right) together with the corresponding pristine MCM-48 and MCM-41 silica. Besides

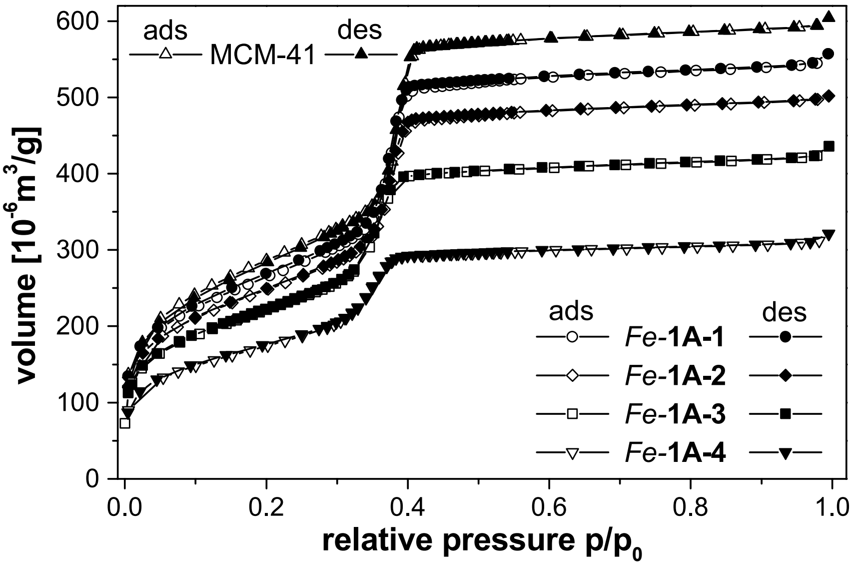

*Figure 5-14: Nitrogen adsorption/desorption isotherms (77 K) of the pristine MCM-41 silica material and the host/guest materials Fe-**1A-1**, **-2**, **-3**, and –**4**.*

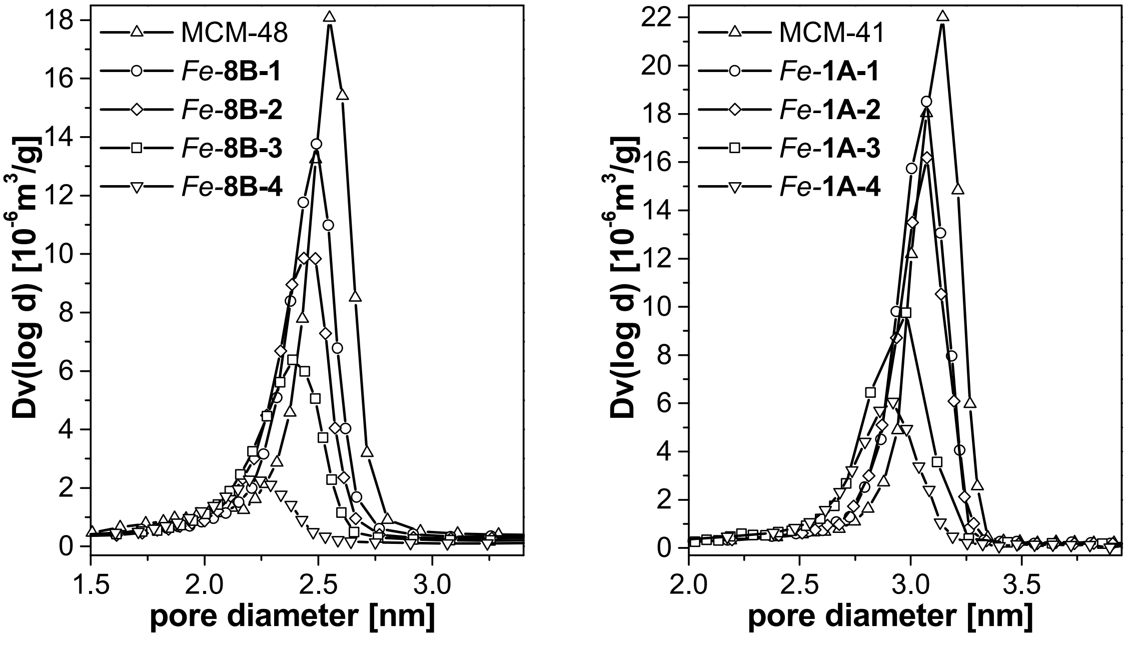

*Figure 5-15: Pore diameter distributions of pristine MCM-48 silica material and the host/guest materials Fe-**8B-1**, **-2**, **-3**, and –**4** (left); pristine MCM-41 silica material and the host/guest materials Fe-**1A-1**, **-2**, **-3**, and –**4** (right).*

the reduction of the mean pore diameter a slight broadening of the distribution is apparent. This is probably due to a slightly inhomogeneous filling/coating of the mesopores as it was also found for the *Fe*-**8A** series by the EDS analysis (cf. section 5.1.1.4, page 76).

A summary of the reduction of the specific surface areas A_s(BET) and the mean pore diameters D_p,N$_2$(BJH) from the pristine MCM-48 and MCM-41 silica and the respective host/guest compounds is given in Table 5-4. The reduction of the surface area and the pore diameter is comparable for the both silica systems although the total decrease is larger for the three-dimensional pore system of the MCM-48 silica material. The total pore volume for the pristine MCM-48 silica is $V_p(p/p_0 = 0.35) = 0.87 \cdot 10^{-6}\text{m}^3/\text{g}$ and for the pristine MCM-41 silica $V_p(p/p_0 = 0.43) = 0.88 \cdot 10^{-6}\text{m}^3/\text{g}$. Since the volumes are comparable and the concentrations of the impregnation solutions were identical the larger decrease in case of the MCM-48 silica material must be due to the differences in the pore diameter or the pore structure itself. Figure 5-16 shows the decrease in the specific surface area A_s due to the concentration of the iron nitrate solution used for the impregnation of MCM-48 and MCM-41 silica materials. The exponential fits for both series intersect at a concentration of 2 mol/l. This shows the strongly reduced capacity for the iron uptake of the MCM-41 silica in comparison to the MCM-48 silica material. However, this effect may be caused by the vulnerability of the MCM-41 silica material

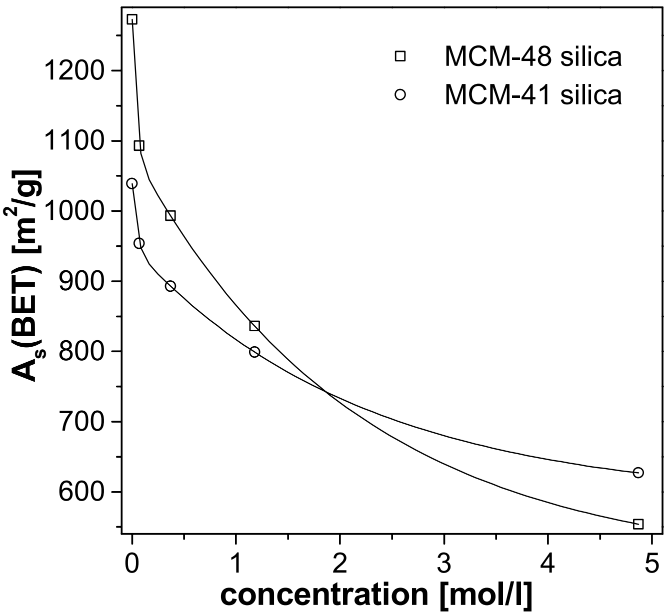

Figure 5-16: Comparison of the surface area reduction due to the used concentration of iron nitrate solution for the synthesis of iron oxide host/guest MCM-48 and MCM-41 silica materials.

*Table 5-4: Nitrogen physisorption data for pristine MCM-48 and MCM-41 silica materials and the corresponding iron oxide containing M41S host/guest compounds of the Fe-**8B** and the Fe-**1A** series. (The percentage decrease with respect to the pristine silica materials is given in brackets.)*

sample	A_s(BET) [m^2/g]	D_p,N_2 (BJH) [nm]
MCM-48 silica	1273	2.55
MCM-41 silica	1039	3.11
Fe-**8B-1**	1093 (86%)	2.47 (97%)
Fe-**1A-1**	954 (92%)	3.06 (98%)
Fe-**8B-2**	993 (78%)	2.43 (95%)
Fe-**1A-2**	893 (86%)	3.04 (98%)
Fe-**8B-3**	836 (66%)	2.37 (93%)
Fe-**1A-3**	799 (77%)	2.94 (95%)
Fe-**8B-4**	554 (44%)	2.19 (86%)
Fe-**1A-4**	627 (60%)	2.89 (93%)

A_s(BET): BET specific surface area; D_p(BJH): BJH mode pore diameter

for pore blocking effects due to its one-dimensional pore system. A comparable situation has been postulated for catalysis on MCM-48 and MCM-41 silica materials [52].

The results of the presented nitrogen physisorption measurements confirm that the mesoporous structure of the MCM-48 and the MCM-41 is maintained even for the highest loading of iron oxide into the mesopores (*Fe*-**8B-4** and *Fe*-**1A-4**).

5.1.2.3 Thermal behavior of *Fe*-**8B-4** and *Fe*-**1A-4**

Thermogravimetric analyses of the redox stability of the transition metal oxide nanoparticles were carried out in comparison to their corresponding bulk phases. Bulk haematite can be easily reduced to magnetite at 673 K by a mixture of 5% hydrogen in 95% nitrogen. In contrast, nanostructured iron(III) oxide within the mesopores of the MCM-48 silica cannot be reduced under the same conditions. Raising the temperature above 700 K results in a reduction of iron(III) to iron(II) but at expense of the formation of the iron silica oxide fayalite (Fe_2SiO_4).

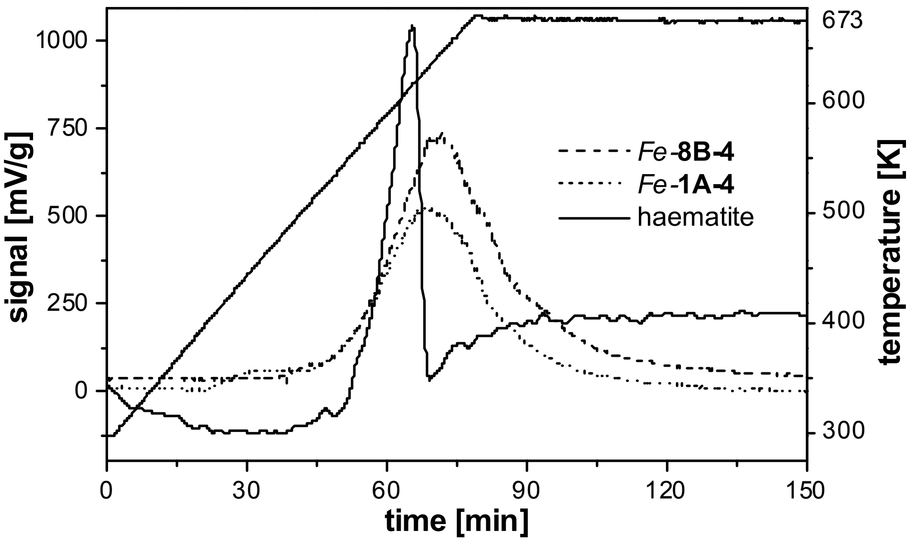

*Figure 5-17: Temperature programmed reduction of bulk haematite, Fe-**8B-4**, and Fe-**1A-4** with a mixture of 35% hydrogen in nitrogen.*

In order to achieve a reduction of the iron oxide within the mesopores the hydrogen concentration was raised up to 35% in 65% nitrogen in a temperature-programmed reduction up to 673 K. Under these conditions a reduction to the products *Fe*-**8B-4-R** and *Fe*-**1A-4-R** was achieved. Figure 5-17 depicts the pathway for the reduction of bulk haematite, *Fe*-**8B-4**, and *Fe*-**1A-4.**

The reduction starts at ca. 530 K and in case of the bulk haematite material it is completed at ca. 630 K with a maximum in the reduction rate at 615 K. In contrast, the reduction of the iron oxide host guest compounds has its maximum at 645 K and is not finished until the constant temperature segment starts. P-XRD patterns of the reduced haematite exhibit only bulk iron metal reflections. In case of the reduced host/guest compounds *Fe*-**8B-4-R** and *Fe*-**1A-4-R** no changes in the P-XRD are observed in comparison to the original *Fe*-**8B-4** and *Fe*-**1A-4** compounds. The brown color of the host/guest compounds changes due to the reduction to very dark brown, almost black.

5.1.2.4 X-ray Absorption Spectroscopy

X-ray absorption spectroscopy was performed at the Fe K-edge of the *Fe*-**8B-4** and the *Fe*-**8B-4-R** material in order to obtain structural information on the iron coordination within the iron oxide nanoparticles and changes due to the reduction. The product of the bulk haematite reduction under the same conditions was used as an iron metal reference. Figure 5-18 shows the normalized Fe K-edge of iron and the two host/guest compounds *Fe*-**8B-4** and *Fe*-**8B-4-R**. The corresponding Fourier transforms

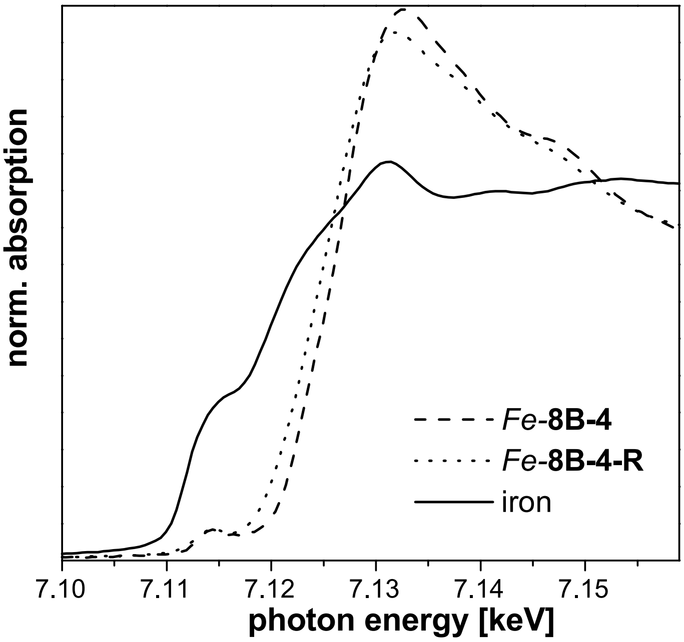

*Figure 5-18: Normalized Fe K-edge XANES spectra of the two host/guest compounds Fe-**8B-4**, Fe-**8B-4-R** and bulk iron from the reduction of haematite.*

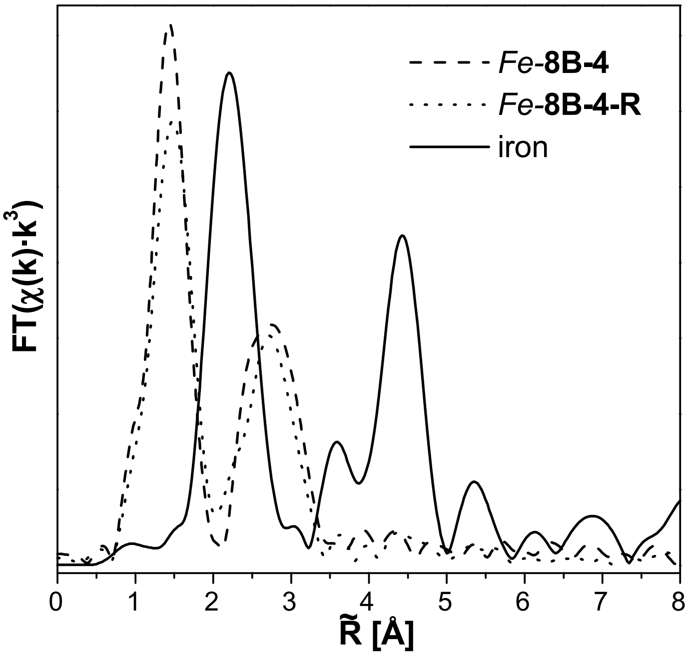

*Figure 5-19: Fourier transforms of the Fe K-edge EXAFS oscillations $\chi(k)\cdot k^3$ of the two host/guest compounds Fe-**8B-4**, Fe-**8B-4-R** and bulk iron.*

of the Fe K-edge EXAFS oscillations $\chi(k)\cdot k^3$ (not phase-corrected) are depicted in Figure 5-19.

The energy position of the absorption edge (second inflection point) of the nanocomposite *Fe*-**8B-4** is comparable to the nanocomposites of the *Fe*-**8A** series (cf.

section 5.1.1.3, page 71), showing a valence shift characteristic of iron(III). In comparison to *Fe*-**8B-4** the energy position of the reduced material *Fe*-**8B-4-R** is shifted to lower energies by 1.5 eV. This reduction can be explained by a partial reduction of iron(III) to iron(II).

The Fourier transformations for the host/guest compounds *Fe*-**8B-4** and *Fe*-**8B-4-R** depicted in Figure 5-19 show the strong decrease of the Fe-Fe metal shells comparable to the results found for the *Fe*-**8A** series (cf. section 5.1.1.3, page 72). The reduced material *Fe*-**8B-4-R** does not show the formation of bulk iron, which is in agreement with the small decrease in the edge position in the XANES region. The main difference between *Fe*-**8B-4** and *Fe*-**8B-4-R** is the reduction of the Fe-O shell by 20% which is due to the partial reduction of iron(III) to iron(II) also in agreement with the XANES results.

The results of the X-ray absorption spectroscopy show a partial reduction of iron(III) in the *Fe*-**8B-4** material to iron(II) in the *Fe*-**8B-4-R** material as expected. In contrast to bulk haematite the reduction has not led to bulk iron metal or metal coatings within the mesoporous host system. Comparable results were obtained for the *Fe*-**1A-4** and *Fe*-**1A-4-R** host/guest compounds (not depicted).

5.1.2.5 Magnetic properties

The magnetic behavior of the *Fe*-**8B-4** and the corresponding reduced *Fe*-**8B-4-R** material was investigated by SQUID measurements. Figure 5-20 shows the static magnetic (left) and the reciprocal static magnetic (right) susceptibility versus temperature for the nanostructured host/guest compound *Fe*-**8B-4**.

The magnetic properties of bulk haematite have been studied extensively both in bulk form and as ultrafine particles [199]. Even if many reports on haematite nanoparticles have been made, the magnetic properties of the small particles are still not understood in detail. Haematite has a rhombohedral crystal structure and is isomorphous to corundum. Bulk haematite orders antiferromagnetically below its Néel temperature $T_N \cong 955$ K. The reciprocal static magnetic susceptibility $1/\chi$ depicted in Figure 5-20 (right) shows a linear dependence in the lower temperature region. This Curie-like behavior $\chi \sim 1/T$ is typical of a paramagnetic material. The fact that now antiferromagnetism is found within the range of the measurement accuracy can be explained by the two-dimensional ordering of the iron coating within the mesopores which does not allow the formation of

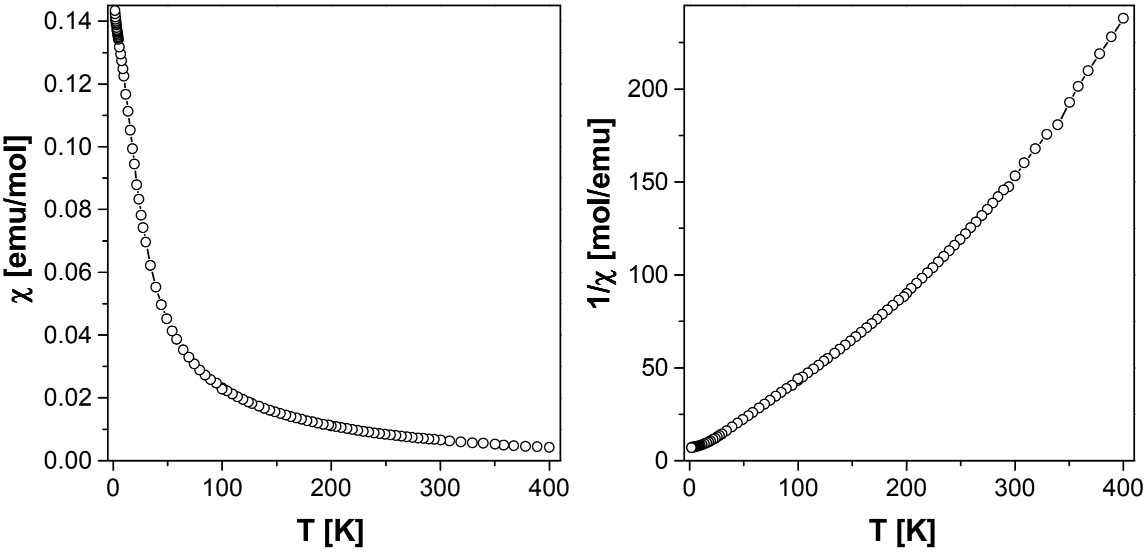

*Figure 5-20: Static magnetic susceptibility χ (left) and reciprocal static magnetic susceptibility $1/\chi$ (right) for the nanostructured host/guest compound Fe-**8B-4**.*

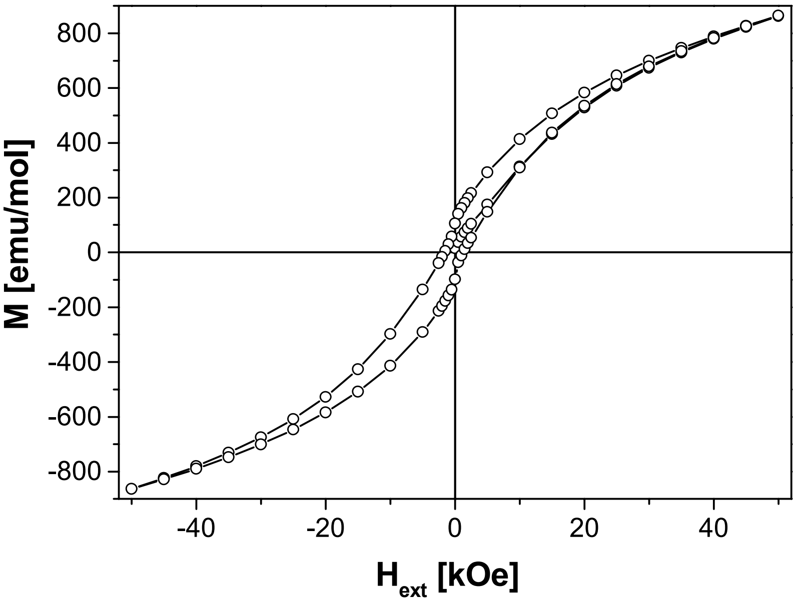

*Figure 5-21: dc-magnetization as a function of the applied field for the host/guest compound Fe-**8B-4** at 4 K.*

large antiferromagnetic domains. Two-dimensional magnetic systems do not exhibit long-range order at higher temperatures. This phenomenon was recently reported for comparable two-dimensional nanostructures of cadmium mangan sulfides within MCM-41 silica phases [200]. These results prove that no large haematite particles were formed during the synthesis within the whole sample. This is in total agreement with the results obtained by P-XRD, nitrogen physisorption, electron microscopy, and XAS (see sections above).

The saturation in the magnetic susceptibility at temperatures below 10 K (see Figure 5-20 left) shows that some ordering effects appear in the nanostructured haematite-like material. These effects are also observed in the dc-magnetization curve at 4 K depicted in Figure 5-21 by the occurrence of a hysteresis, indicating a weak ferromagnetic moment. Figure 5-22 shows the corresponding measurement at 300 K and, as expected, for the paramagnetic *Fe*-**8B-4** compound no hysteresis is observed.

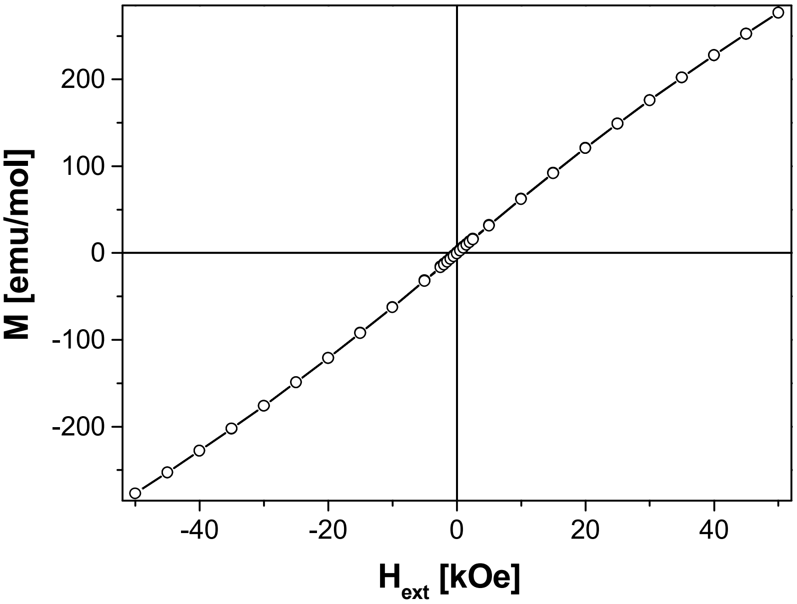

*Figure 5-22: dc-magnetization as a function of the applied field for the host/guest compound Fe-**8B-4** at 300 K.*

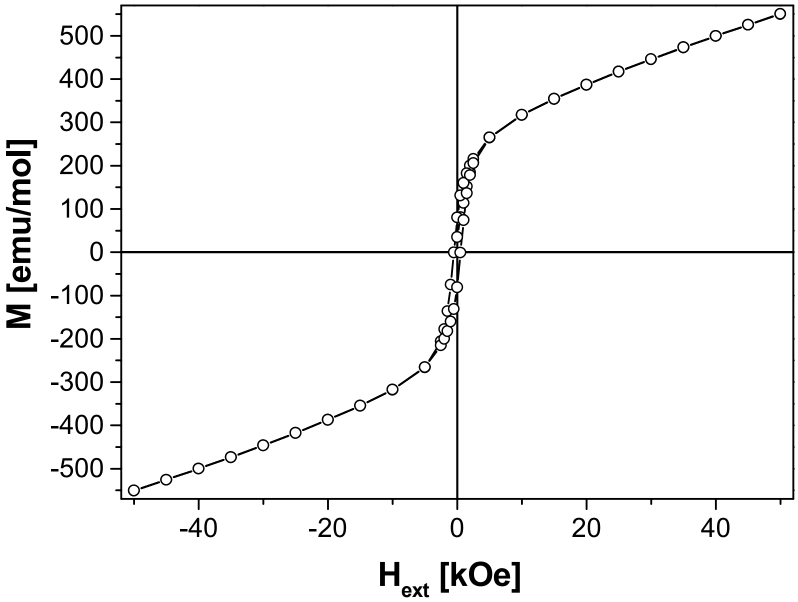

*Figure 5-23: dc-magnetization as a function of the applied field for the host/guest compound Fe-**8B-4-R** at 300 K.*

In contrast, the dc-magnetization curve at 300 K for the reduced host/guest compound *Fe*-**8B-4-R** exhibits a hysteresis and an increase in the total magnetization as shown in Figure 5-23. This spontaneous magnetization at 300 K shows that a magnetic phase was formed by the partial reduction of some iron(III) to iron(II). A broadening of the hysteresis and an increase in the total magnetization is observed for the measurement at 2 K as depicted in Figure 5-24.

Figure 5-25 shows the static magnetic susceptibility χ (left) and the reciprocal static susceptibility $1/\chi$ (right) versus temperature for the nanostructured host/guest compound

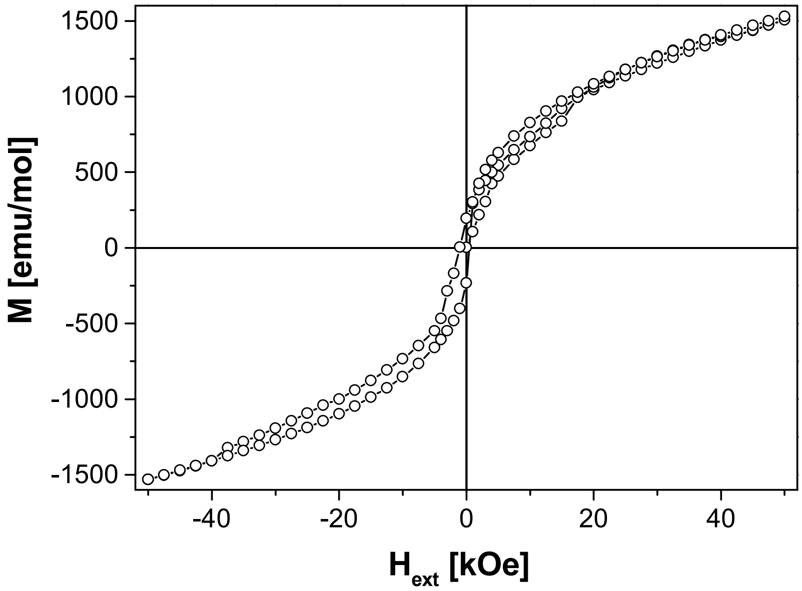

*Figure 5-24: dc-magnetization as a function of the applied field for the host/guest compound Fe-**8B-4-R** at 2 K.*

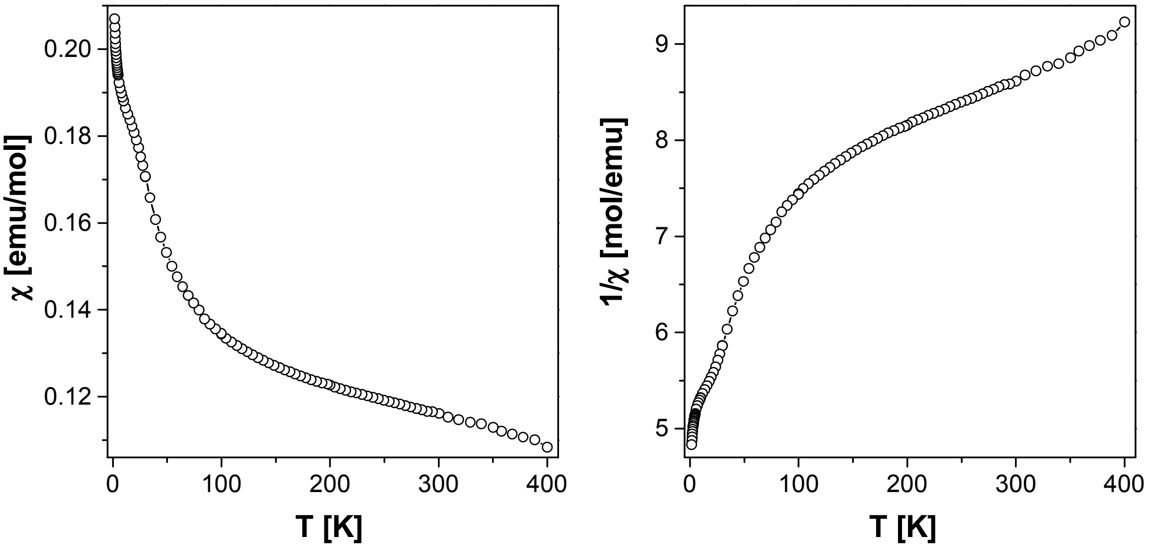

*Figure 5-25: Static magnetic susceptibility χ (left) and reciprocal static magnetic susceptibility $1/\chi$ for the nanostructured host/guest compound Fe-**8B-4-R**.*

Fe-**8B-4-R**. A comparison of the static susceptibility χ of the *Fe*-**8B-4** (Figure 5-20 left) and its reduced product *Fe*-**8B-4-R** (Figure 5-25 left) shows a large additive offset of 0.11 emu/mol due to the new ferromagnetic phase in the reduced product. This phase also shows the loss of the Curie-like behavior in the reciprocal static susceptibility as depicted in Figure 5-25, right.

A brief calculation of the amount of the ferromagnetic phase which is supposed to be magnetite-like leads to 10% within 90% of paramagnetic iron(III) oxide within *Fe*-**8B-4-R**. This low amount of the magnetic phase is due to the instability of the iron(II) species within the mesostructured iron oxide phase. In contrast to bulk haematite which is easily reduced to magnetite or bulk iron, the mesostructured haematite-like structure can less conveniently be reduced. High hydrogen concentrations are necessary and the product is only partially reduced to iron(II). However, due to the thin coatings of this material within the mesopores it is easily reoxidized by air.

5.2 Cobalt iron oxide within mesoporous silica

Cobalt iron oxide within the mesopores is formed by impregnation with a 1:2 Co/Fe nitrate solution, which can generally lead to one of the following oxides: Fe_2O_3, Co_2O_3, Fe_3O_4, Co_3O_4 or $CoFe_2O_4$. As the calcination temperature for the formation of the oxides from the nitrates was 875 K, the formation of all oxyhydroxides of iron and cobalt can be excluded. A water uptake of the final products was not detected; post-synthetic formation of hydroxides can also be excluded. *CoFe₂*-**8A-1** was tempered after calcination in air for 72 hours at 873 K and *CoFe₂*-**8A-2** at 923 K.

5.2.1 Powder X-ray diffraction

The P-XRD patterns of the pristine MCM-48 silica and the host/guest compounds *CoFe₂*-**8A-1** and *CoFe₂*-**8A-2** show a reduction of the reflections relative to those of the pristine MCM-48 silica material as depicted in Figure 5-26.

After the treatment of the pristine MCM-48 silica phase with the aqueous solution of cobalt/iron nitrate and following drying, all hkl reflections have disappeared. They reappear during the transformation of the nitrate to the oxide in the course of calcination as reported in section 5.1.1.1, page 67 [16,18]. The increase of intensity of the reflections as a function of temperature may be interpreted as an annealing of the particles within the pores.

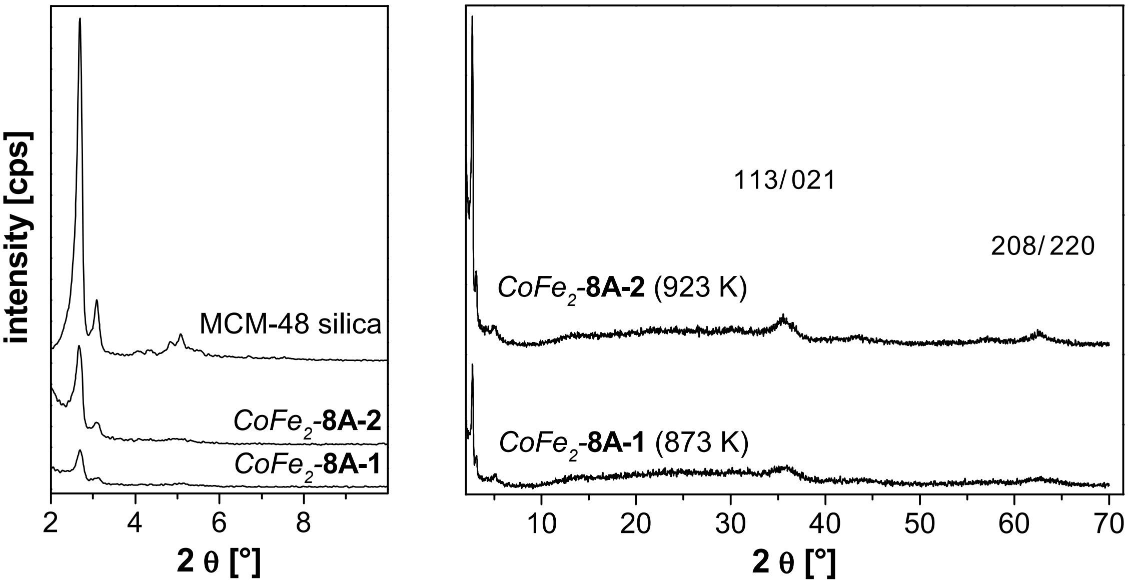

*Figure 5-26: P-XRD: low angle region of pristine MCM-48 silica and the host/guest compounds CoFe₂-**8A-1** and CoFe₂-**8A-2** (left); high-angle region P-XRD of CoFe₂-**8A-1** and CoFe₂-**8A-2** (right).*

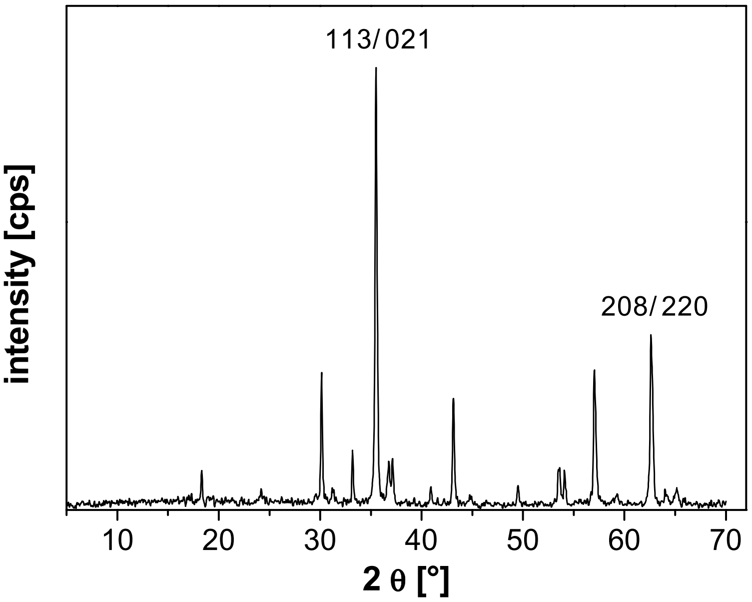

Figure 5-27: Powder X-ray diffractogram of the inverse spinel cobalt ferrite $CoFe_2O_4$.

*Table 5-5: d_{hkl}-values [nm] of P-XRD reflections for bulk $CoFe_2O_4$ and the host/guest compounds $CoFe_2$-**8A-1** and $CoFe_2$-**8A-2**.*

hkl	**intensity[%]**	**$CoFe_2O_4$**	*CoFe₂*-**8A-1**	*CoFe₂*-**8A-2**
003/101	11	0.49	-	-
104/110	30	0.30	-	-
113/021	100	0.25	0.25	0.25
006/202	8	0.24	-	-
024	21	0.21	-	-
214/300	8	0.17	-	-
125/033	28	0.16	-	-
208/220	36	0.15	0.15	0.15

The *d*-spacings of the 211 ($d = 3.31$ nm) and 220 ($d = 2.86$ nm) reflections of the pristine MCM-48 silica are observable in the host/guest compounds whereas the higher order reflections (2 θ: 4-6°) disappear. In addition, the 113/021 ($d = 0.25$ nm;

I = 100%) and 208/220 (*d* = 0.15 nm; *I* = 36%) reflections of the inverse cobalt iron structure appear in *CoFe₂*-**8A-1** and *CoFe₂*-**8A-2**. In contrast to the bulk material of $CoFe_2O_4$ (Figure 5-27) synthesized under exactly the same conditions as the *CoFe₂*-**8A-1** and *CoFe₂*-**8A-2**, the reflections of the host/guest compounds are much broader and weaker in intensity, indicating the occurrence of very small particles. Table 5-5 summarizes the d_{hkl}-values of the bulk and the nanostructured cobalt iron oxides for all reflections with intensities above 5% of the main 113/021 reflection.

Applying the Scherrer formula to the 113/021 reflections reveals an average particle size of approximately 5-6 nm. This size, which is larger than the mean pore diameter of the host structure, can either be attributed to elongated particles within the mesoporous network or to particles on the outer surface. The latter is unlikely as an undisturbed crystal growth of unconfined particles outside of the mesopores would lead to larger particle sizes and therefore to much higher peak intensities in the corresponding XRD pattern (compare Figure 5-26 and Figure 5-27).

The results obtained by powder X-ray diffraction show clearly that an inverse spinel structure has been formed. Among the phases listed above only Fe_3O_4 and $CoFe_2O_4$ are of this type, whereas Co_3O_4 forms a normal spinel structure.

5.2.2 Nitrogen physisorption

The nitrogen adsorption/desorption isotherms show typical type IV profiles (IUPAC classification [3]) for the pristine MCM-48 and the MCM-48 silica host/guest compounds *CoFe₂*-**8A-1** and *CoFe₂*-**8A-2** (Figure 5-28).

The sharp steps in the isotherms at a relative pressure of $p/p_0 = 0.28$ in case of the pristine MCM-48 silica and 0.23 for the transition-metal-containing silica reveal the high degree of structural order of the mesoporous systems. The hysteresis starting at a relative pressure of $p/p_0 = 0.47$ arises from pores between the mesoporous particles. By application of the BJH theory to the desorption isotherms of all three samples the pore diameter distributions can be calculated.

The pore diameter distribution of the pristine MCM-48 material shows a sharp maximum with a mean pore diameter of 2.49 nm (Figure 5-29). For the Co/Fe oxide-containing silica the mean pore diameter of the slightly broader distribution is decreased to 2.25 (*CoFe₂*-**8A-1**) and 2.24 nm (*CoFe₂*-**8A-2**).

The decrease of the adsorbed gas volume as well as the smaller mean pore diameter is an evidence that the Co/Fe oxide is located within the pores of the MCM-48. It is

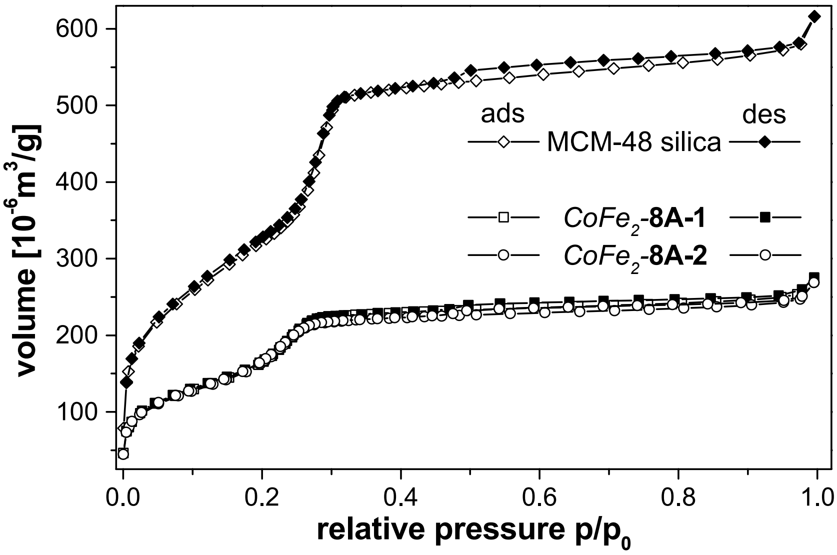

*Figure 5-28: Nitrogen physisorption isotherms (77 K) of the pristine MCM-48 silica phase and the host/guest compounds CoFe$_2$-**8A-1** (873 K) and CoFe$_2$-**8A-2** (923 K).*

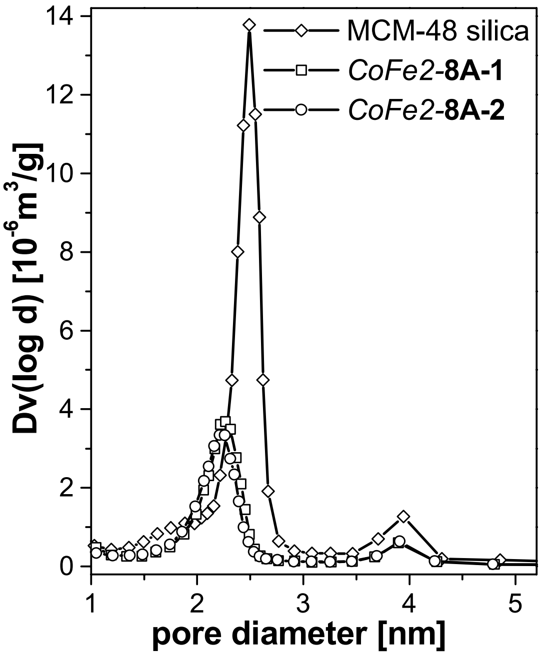

*Figure 5-29: Pore diameter distribution of pristine MCM-48 silica, CoFe$_2$-**8A-1** and CoFe$_2$-**8A-2**.*

remarkable that the different calcination temperatures do not affect the pore system. In contrast to the small changes in the XRD patterns the differences in the adsorption/desorption isotherms are marginal. To ensure that the Co/Fe oxide nanoparticles have been formed mainly within instead of outside the pores, the pore diameter was also determined by applying another method based on geometrical calculations. By assuming cylindrical pores the average pore diameter D_h can be calculated as $D_h = 4 \cdot V_p/A_s$(BET) (cf. Chapter 4.1.1, page 38). Table 5-6 shows the respective data of the pore diameters, the specific surface, and the pore volume for the pristine MCM-48 silica phase and the transition metal oxide containing phases *CoFe₂*-**8A-1** and *CoFe₂*-**8A-2**.

The decrease of the inner surface and pore volume is comparable to the decrease that is found for the incorporation of iron oxides within MCM-48 silica phases (cf. section 5.1.1.2, page 68). The pore diameters D_h are comparable to the BJH mode pore diameters and the reduction due to the formation of the cobalt iron oxide species within the mesopores is also of the same magnitude. This is strong evidence for the incorporation of the ternary transition metal oxide within the mesopores of the MCM-48 molecular sieve. If the oxide was located on the outer surface, the pore diameter D_p would not change for the transformation of the pristine MCM-48 to the impregnated products *CoFe₂*-**8A-1** and *CoFe₂*-**8A-2**. However, the calculated pore diameter D_h must change because the reduction of the inner surface and pore volume would still be observable. Both parameters are normalized to the mass.

*Table 5-6: Characterization of the pristine MCM-48 silica and the host/guest compound CoFe₂-**8A-1** and CoFe₂-**8A-2** with respect to specific surface area, pore volume and mean pore diameter.*

sample	**A_s(BET) [m^2/g]**	**V_p [$10^{-6}m^3/g$]**	**D_p,N_2(BJH) [nm]**	**D_h [nm]**
MCM-48	1217	0.81 (p/p_0=0.40)	2.49	2.66
CoFe₂-**8A-1**	569	0.35 (p/p_0=0.38)	2.25	2.46
CoFe₂-**8A-2**	564	0.34 (p/p_0=0.38)	2.24	2.41

A_s(BET): BET specific surface area; V_p: pore volume; D_p(BJH): BJH mode pore diameter; $D_h = 4V_p/A_s$: average pore diameter.

5.2.3 X-ray absorption spectroscopy

Powder X-ray diffraction has revealed that an inverse spinel structure is formed during the synthesis. Only Fe_3O_4, $CoFe_2O_4$ are of this type; Co_3O_4 forms a normal spinel structure and all other possible cobalt and iron oxides are of other structural types (cf. section 5.2.1, page 91). X-ray absorption spectroscopic (XAS) measurements were performed at the Fe K-edge and Co K-edge in order to obtain further information on the structure and oxidation state of Fe and Co within the transition metal oxide nanoparticles. Bulk α-Fe_2O_3 and $CoFe_2O_4$ were used as reference compounds for the Fe K-edge and Co_3O_4 and $CoFe_2O_4$ for the Co K-edge.

The XANES regions of the Fe K- and Co K-edges are depicted in Figure 5-30 and Figure 5-31. The energy position of the Fe K-edge (Figure 5-30) of the structured host/guest compounds appear at the same position as the bulk reference materials $CoFe_2O_4$ and α-Fe_2O_3, indicating a valence shift characteristic of iron(III). In addition, the overall shape, which can be regarded as a fingerprint of the structure, shows strong similarities to the XANES of $CoFe_2O_4$. All features are a little bit smeared out, which is typical of slightly disordered nanoparticles [18,193]. In contrast, the XANES of the Co K-edge (Figure 5-31) of the Co_3O_4 is much more complex as compared to the nanocomposites and the reference material $CoFe_2O_4$. The latter is an inverse spinel with only cobalt(II), whereas Co_3O_4 contains a 1:2 mixture of cobalt(II) and (III). Again, the

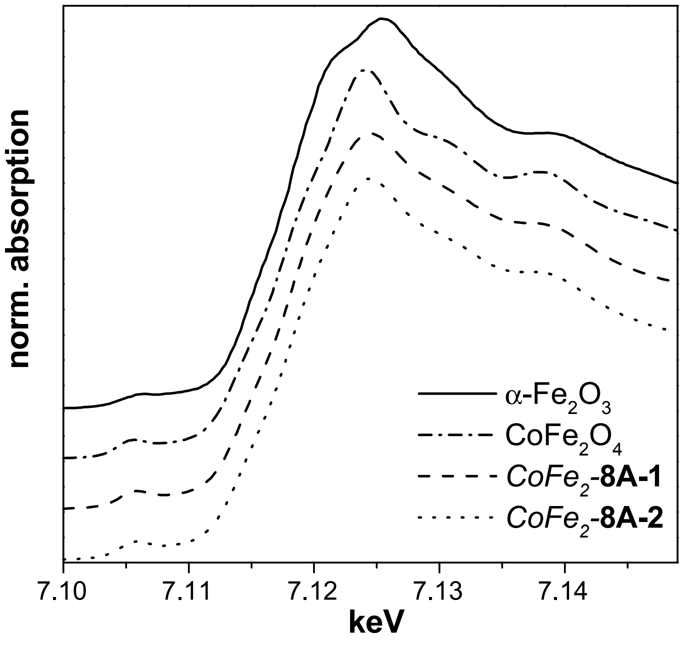

Figure 5-30: Fe K-edge XANES spectra of the nanostructured host/guest compounds CoFe$_2$*-**8A-1** and CoFe*$_2$*-**8A-2** and reference materials.*

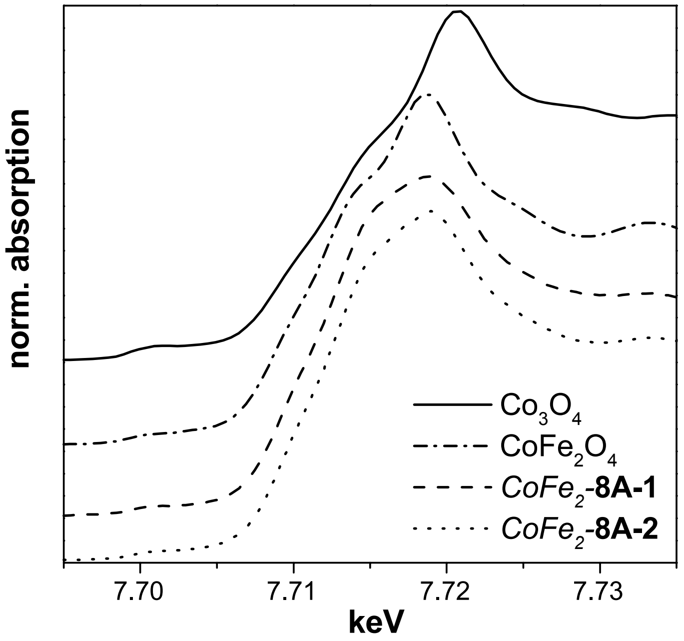

*Figure 5-31: Co K-edge XANES spectra of the nanostructured host/guest compounds $CoFe_2$-**8A-1** and $CoFe_2$-**8A-2** and reference materials.*

XANES of the host/guest compounds indicates the existence of only cobalt(II) and, therefore, $CoFe_2O_4$. CoO can be excluded because it requires a much higher synthesis temperature.

Figure 5-32 and Figure 5-33 show qualitative analyses of the Fourier transformations (FTs) of the respective EXAFS oscillations of the reference compounds and the incorporated transition metal oxides *$CoFe_2$*-**8A-1** and *$CoFe_2$*-**8A-2**. The reference compounds show peaks in the radial distribution up to 5.5 Å while the incorporated transition metal oxides *$CoFe_2$*-**8A-1** and *$CoFe_2$*-**8A-2** show only peaks up to 3.3 Å, respectively. A comparison of the first shell (oxygen shell) between 1 and 2 Å does not show any difference in the amplitude between the reference $CoFe_2O_4$ and the products *$CoFe_2$*-**8A-1** and *$CoFe_2$*-**8A-2**. In contrast, the amplitude of the first oxygen shell in the bulk Co_3O_4 is significantly more intense, due to the existence of the two Co sites. The amplitude of the higher shells, which represent the metal-metal distances, are strongly reduced for the host/guest compounds *$CoFe_2$*-**8A-1** and *$CoFe_2$*-**8A-2** as compared to the bulk reference compounds. This is observed within 2 – 5.5 Å in Figure 5-32 and Figure 5-33 and provides another indication for small particles within the mesopores.

The XAS results in combination with results obtained by nitrogen physisorption, powder X-ray diffraction, and microscopic investigations (not depicted) show that the ternary cobalt iron oxide $CoFe_2O_4$ was formed almost exclusively within the pores of the MCM-48 silica host material. The material is stable up to temperatures of 923 K and the particle size is almost 6 nm, which can be explained by crystalline particles or coatings along the channels of the mesoporous host system.

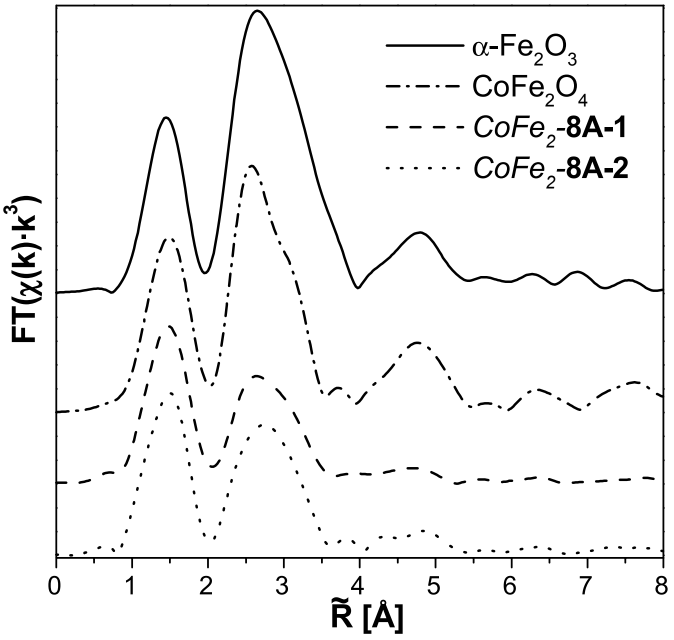

*Figure 5-32: Fe K-edge FTs of the nanostructured host/guest compounds CoFe$_2$-**8A-1**, CoFe$_2$-**8A-2**, and reference materials.*

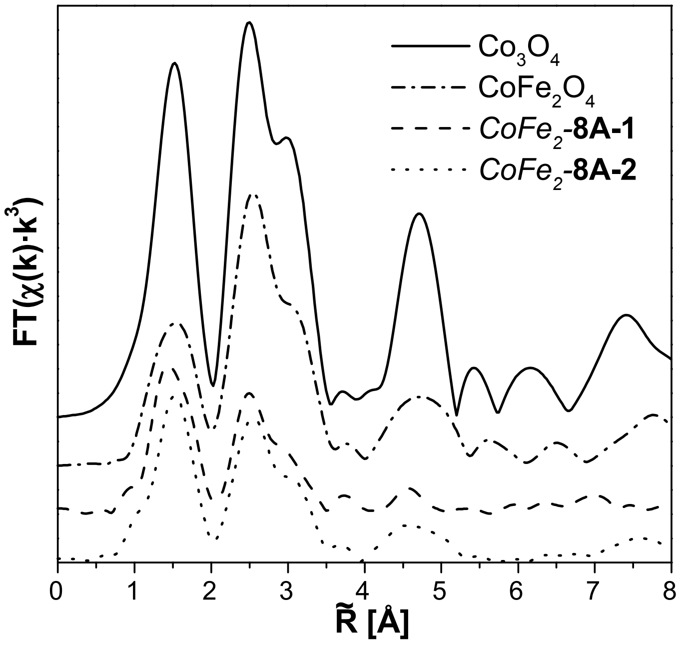

*Figure 5-33: Co K-edge FTs of the nanostructured host/guest compounds CoFe$_2$-**8A-1**, CoFe$_2$-**8A-2**, and reference materials.*

5.3 Cobalt oxide within mesoporous silica

Two different cobalt oxide coated mesoporous MCM-48 silica materials were synthesized for the investigation of their magnetic behavior due to reduction. The *Co*-**8A-1** material was synthesized with a 0.8 M and the *Co*-**8A-**2 with a 1.6 M cobalt nitrate solution. The reduction of the host/guest compound *Co*-**8A-2** to *Co*-**8A-2-R** was achieved by hydrogen at 873 K (cf. section 2.3.3 and 2.4.5).

5.3.1 Powder X-ray diffraction

The P-XRD patterns of the pristine MCM-48 silica and the host/guest compounds *Co*-**8A-1** and *Co*-**8A-2** show a decrease of the intensity of the reflections in comparison to the pristine MCM-48 silica material as depicted in Figure 5-34 (left), comparable to the iron cobalt coated materials (cf. section 5.2.1, page 91). Very broad high order Bragg reflections are observed above 2 $\theta = 30°$ as depicted in Figure 5-34 (right). These reflections can be attributed to nanoparticles of the Co_3O_4 spinel systems. A rough estimation of the crystallite size by applying the Scherrer formula leads to particles of ca. 5 - 6 nm in diameter. Table 5-7 gives a summary of the d_{hkl}-values and intensities for Co_3O_4 and the two cobalt oxide host/guest materials *Co*-**8A-1** and *Co*-**8A-2**. All reflections with intensities over 15% with reference to the 311 main reflection are observable for the host/guest compounds.

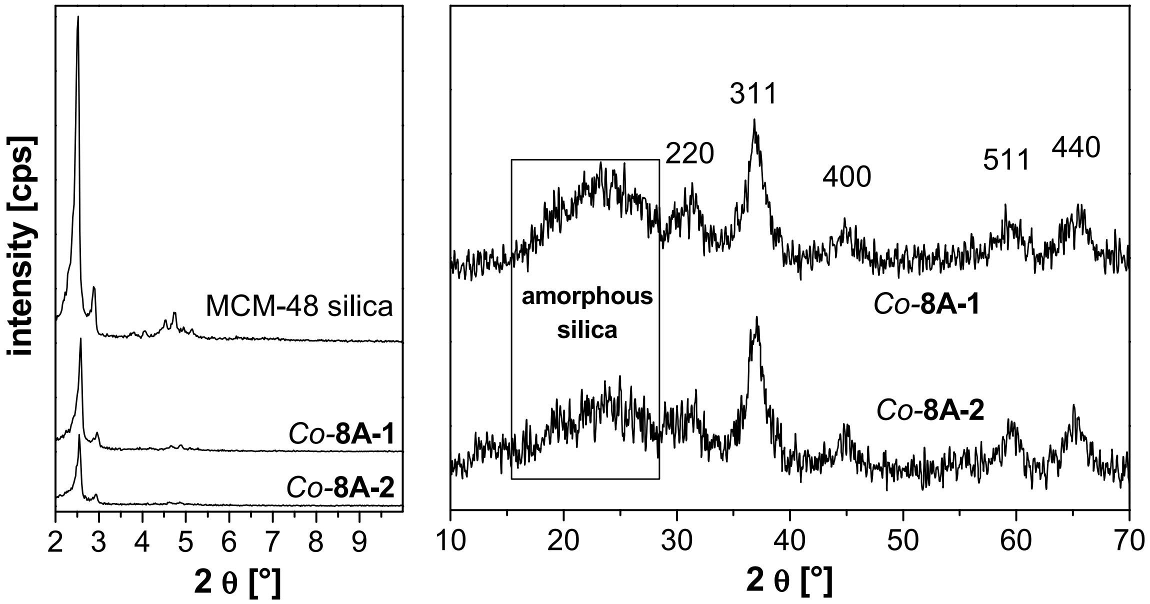

*Figure 5-34: P-XRD: low angle region of pristine MCM-48 silica and the host/guest compounds Co-**8A-1** and Co-**8A-2** (left); high-angle region P-XRD of Co-**8A-1** and Co-**8A-2** (right) (smoothed and enlarged by a factor of 100).*

Table 5-7: d_{hkl}-values [nm] of P-XRD reflections for Co_3O_4 [201] and the host/guest compounds Co-***8A-1*** *and* Co-***8A-2***.

hkl	**intensity[%]**	**Co_3O_4**	*Co*-**8A-1**	*Co*-**8A-2**
111	1	0.467	-	-
220	29	0.286	0.285	0.287
311	100	0.244	0.243	0.245
222	8	0.234	-	-
400	17	0.204	0.202	0.203
331	3	0.185	-	-
422	7	0.165	-	-
511	21	0.156	0.155	0.156
440	30	0.143	0.143	0.143
531	< 1	0.137	-	-
442	< 1	0.135	-	-
620	2	0.128	-	-
533	6	0.123	-	-
622	3	0.122	-	-
444	2	0.117	-	-

In the following sections the focus of the investigations is set on the *Co*-**8A-2** host/guest compound with the higher cobalt loading due to the fact that small Co_3O_4 nanoparticles appear independently of the used synthesis concentration of cobalt nitrate as proved by P-XRD.

5.3.2 Nitrogen physisorption

The nitrogen physisorption experiments at 77 K lead to a specific surface area $A_s = 707\ m^2/g$ and a mean pore diameter $D_p(BJH) = 2.39$ nm for the host/guest compound *Co*-**8A-2** and $A_s = 1107\ m^2/g$ and $D_p(BJH) = 2.64$ nm for the pristine MCM-48 silica material. The decrease of the inner surface and the pore diameter is of the same magnitude as reported in the previous sections for the iron oxide and cobalt

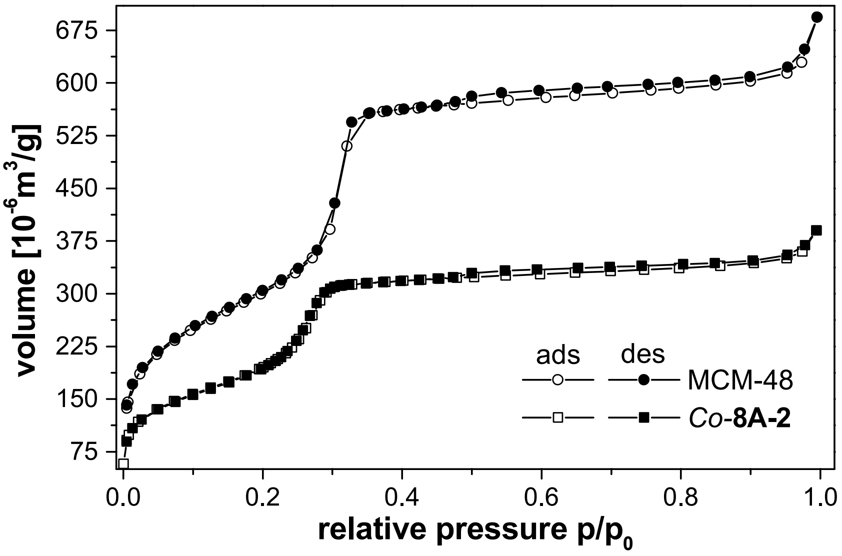

*Figure 5-35: Nitrogen physisorption isotherms (77 K) of the pristine MCM-48 silica phase and the host/guest compound Co-**8A-2**.*

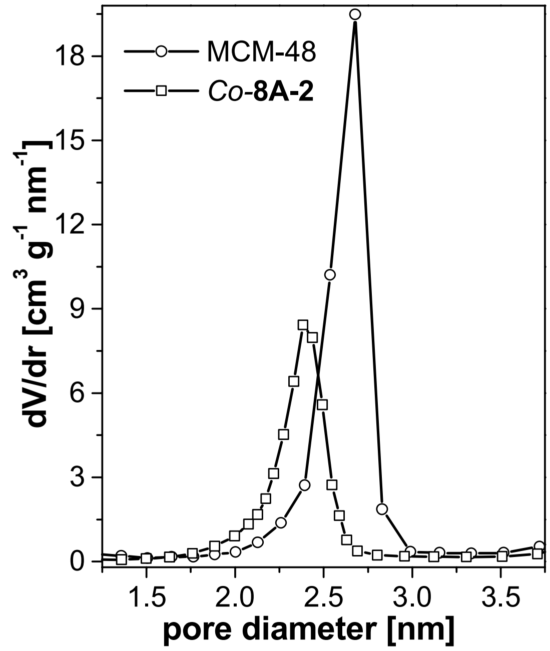

*Figure 5-36: Pore diameter distribution of pristine MCM-48 silica, CoFe$_2$-**8A-1** and CoFe$_2$-**8A-2**.*

iron oxide host/guest compounds (cf. section 5.1.1.2, page 68, section 5.1.2.2, page 80, and section 5.2.2, page 93).

Figure 5-35 and Figure 5-36 show the corresponding nitrogen physisorption isotherms and the pore diameter distribution curves, respectively. The physisorption isotherms for the nanostructured host/guest compound *Co*-**8A-2** are of type IV, as typical for mesoporous materials [3]. The pore diameter distribution reveals a shrinkage of at least 0.25 nm due to the introduction of the cobalt oxide into the mesoporous host system.

Although larger nanoparticles of at least 5-6 nm are formed as revealed by the P-XRD results (cf. section 5.2.1, page 91), a formation of any larger particles is not observed by the physisorption measurements as already discussed for the cobalt iron oxide nanostructures (cf. section 5.2.2, page 95). This may be due to the coating effect which leads to a two-dimensional decoration of the pore walls that extends over longer distances along the channel system without the formation of spherical particles.

5.3.3 X-ray Absorption Spectroscopy

X-ray absorption spectroscopy was performed at the Co K-edge in order to obtain further information on the structure and oxidation state of Co within host/guest compound *Co*-**8A-2** and its reduction product *Co*-**8A-2-R**. Figure 5-37 shows the normalized Co K-edge XANES spectra for both nanostructured compounds and a cobalt foil which was measured simultaneously as reference. All spectra show a small pre-edge shoulder caused by dipole-allowed electronic transitions. A shift of ca. 2 eV in the edge position to lower energy is observed for the compound *Co*-**8A-2-R** in comparison to

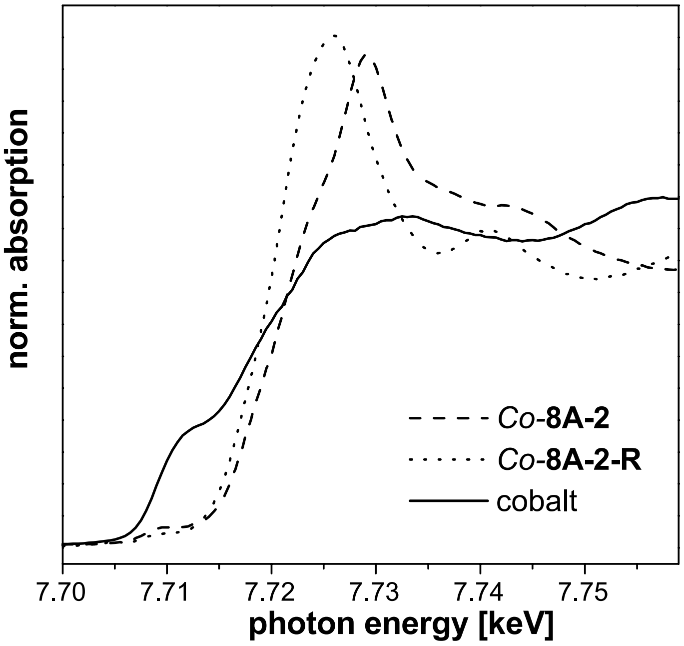

*Figure 5-37: Normalized Co K-XANES spectra of the host/guest compounds Co-**8A-2** and Co-**8A-2-R** and cobalt metal foil.*

its parent material *Co*-**8A-2**. The edge position (second turning-point)of the reduced compound *Co*-**8A-2-R** is almost at the same position as for the cobalt metal foil indicating a valence shift characteristic of cobalt(0) although its XANES region does not look similar to the cobalt metal. This is due to the fact that the cobalt within the mesopores is located on the silica surface and therefore it has still some oxygen atoms as nearest neighbors.

The results obtained by the analysis of the XANES region are confirmed by the EXAFS analysis shown in Figure 5-38 for cobalt metal and the host/guest compounds *Co*-**8A-2** and *Co*-**8A-2-R**.

For further data analyses the Co-O and the Co-Co coordination shells were extracted by Fourier filtering using a Bessel window ranging from $R = 1.1$ to 3.5 Å for *Co*-**8A-2** and $R = 1.5$ to 3.5 Å for *Co*-**8A-2-R**. Refined structure parameters were obtained by fitting the obtained backtransforms (BTs) in k-space within the range of $k = 3.6$-13.3 $Å^{-1}$ using the shells representing a Co-O shell and two different Co-Co shells. In case of bulk cobalt, one shells was used. To keep the number of independent parameters as low as possible during the refinements, some restrictions with respect to the variables had to be made: (1) The amplitude reduction factor was constrained between 0.8 and 1.0 and (2) the Debye-Waller factors were constrained within the range of 0.001-0.01 $Å^2$.

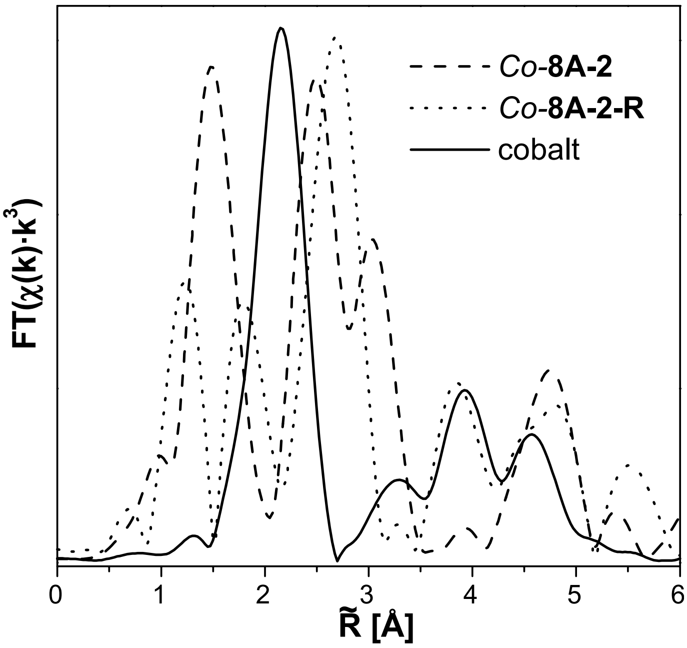

*Figure 5-38: Fourier transforms (not phase corrected) of the Co K-edge EXAFS oscillations $\chi(k)\cdot k^3$ of the host/guest compounds Co-**8A-2** and Co-**8A-2-R** and cobalt.*

*Table 5-8: Refined structure parameters of the Co-O and the Co-Co coordination shells, extracted from the Co K-EXAFS of the host/guest compounds Co-**8A-2** and Co-**8A-2-R** and cobalt.*

coordination shell	parameter	*Co*-**8A-2**	*Co*-**8A-2-R**	cobalt
Co-O	N	4.57	1.39	-
	R [Å]	1.91	2.14	-
	$\Delta\sigma^2$ [Å^2]	0.003	0.003	-
	ΔE_0 [eV]	-0.08	8.51	-
Co-Co	N	3.82	8.07	12.0
	R [Å]	2.86	3.00	2.49
	$\Delta\sigma^2$ [Å^2]	0.005	0.009	0.006
	ΔE_0 [eV]	0.73	1.62	2.43
Co-Co	N	9.19	-	-
	R [Å]	3.37	-	-
	$\Delta\sigma^2$ [Å^2]	0.001	-	-
	ΔE_0 [eV]	7.70	-	-

Abbreviations: N = coordination number; R = bond length; $\Delta\sigma^2$ = Debye-Waller factor; ΔE_0 = energy shift.

In general, the number of independent degrees of freedom in a spectrum is given by $N_{ind} = (2\Delta k\Delta R/\pi)+2$. In all cases, the number of parameters used in the fits was significantly smaller than the calculated value of N_{ind}. The results of the fits are given in Table 5-8.

The reduced host/guest compound *Co*-**8A-2-R** shows a strong decrease in the oxygen coordination number in comparison to the original *Co*-**8A-2** material. Besides this decrease the Co-O distance is increased significantly. The two Co-Co shells of the Co_3O_4 in the *Co*-**8A-2** have changed into one single shell in the reduced *Co*-**8A-2-R** material. These results show that the original oxygen coordination of cobalt is totally changed and that the two different Co-Co coordination shells do not exist in the reduced product anymore.

In comparison to the Co-Co shell in the cobalt metal foil the Co-Co distance in the

Co-**8A-2-R** materials is larger by 0.5 Å. This can be explained as the effect of a packing of Co atoms in an almost monomolecular two-dimensional layer within the mesopores.

5.3.4 Magnetic behavior of *Co*-8A-1 and *Co*-8A-2-R

The magnetic behavior of the cobalt oxide containing mesoporous silica *Co*-**8A-2** was investigated by SQUID measurements. The *Co*-**8A-2-R** material was transferred into the SQUID apparatus immediately after reduction.

The magnetic susceptibility was measured as a function of the temperature in a small external magnetic field of 100 Oe. The samples were demagnetized before the zero field cooling measurement was started. Figure 5-39 and Figure 5-40 show the magnetic and the reciprocal magnetic susceptibilities for the *Co*-**8A-2** and *Co*-**8A-2-R**, respectively.

The magnetic susceptibility of *Co*-**8A-2** (Figure 5-39) shows a Curie-like behavior in the zero field and the field cooling curve. The nanostructured Co_3O_4 shows a paramagnetic behavior as expected for bulk Co_3O_4 material [202]. In contrast to *Co*-**8A-2**, the reduced host/guest compound *Co*-**8A-2-R** shows significant differences in the zero field and the field cooling curves (Figure 5-40). With increasing temperature the magnetic susceptibility χ increases constantly, which shows that the increase of the temperature leads to an ordering of the magnetic moments within the sample. If the temperature is decreased again the magnetic field energy of the ordered moments is high enough to maintain the ordering down to the lowest temperatures. In contrast to

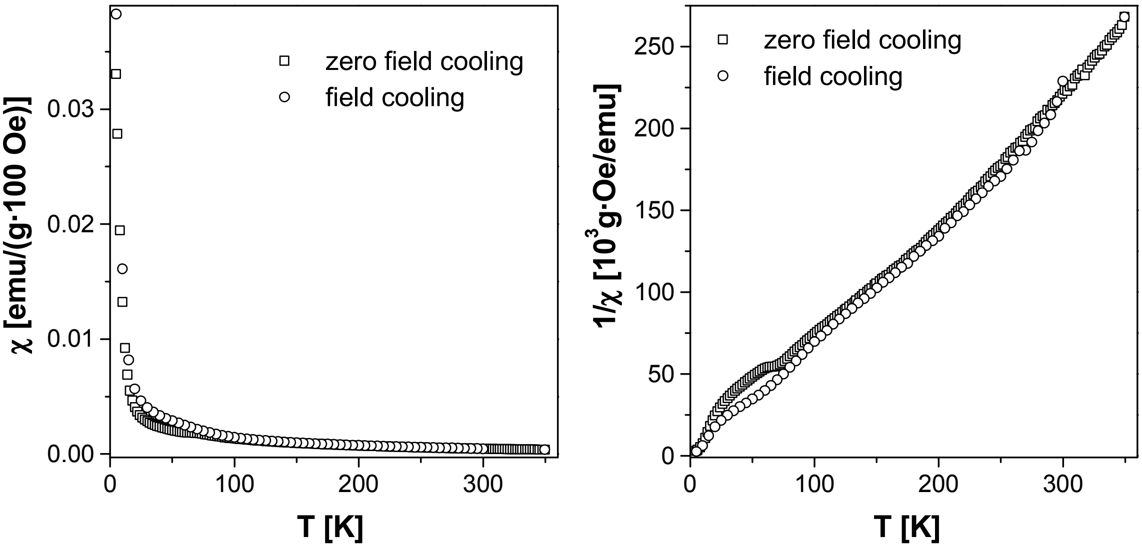

*Figure 5-39: Magnetic susceptibility χ (left) and reciprocal susceptibility $1/\chi$ (right) by zero field and field cooling for the nanostructured host/guest compound Co-**8A-2**.*

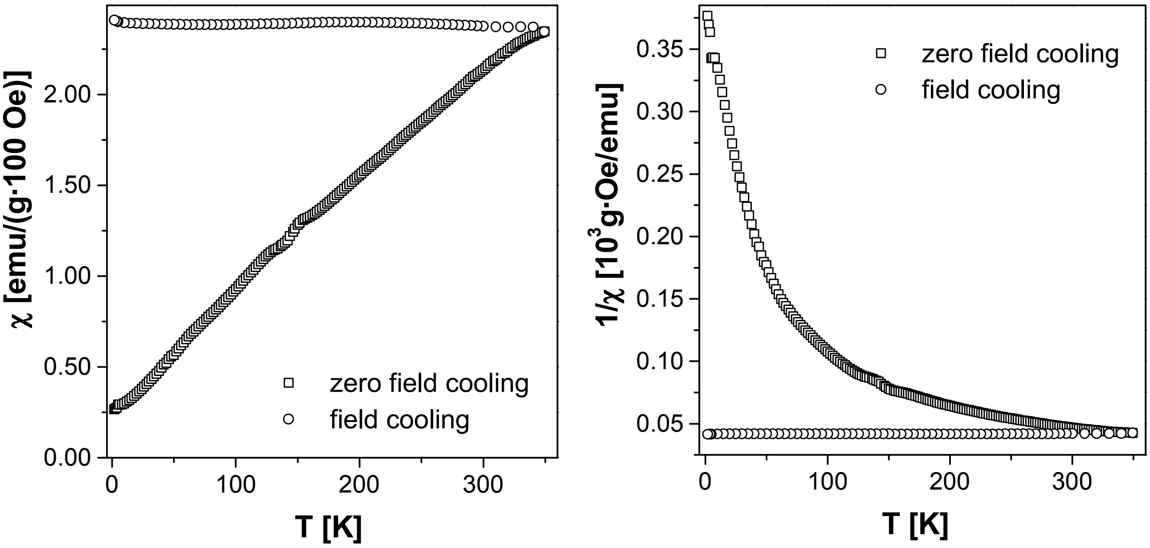

*Figure 5-40: Magnetic susceptibility χ (left) and reciprocal susceptibility 1/χ (right) by zero field and field cooling for the reduced nanostructured host/guest compound Co-**8A-2-R**.*

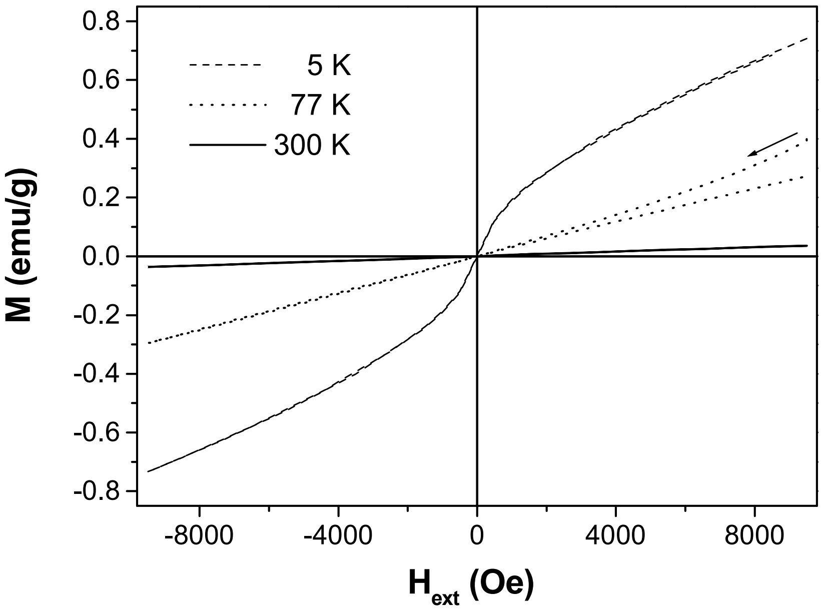

*Figure 5-41: dc-magnetization as a function of the applied field for the nanostructured host/guest compound Co-**8A-2** at 5, 77, and 300 K.*

spherical cobalt nanoparticles no superparamagnetic effects with decreasing temperature are found [203]. This is due to the coating of the mesopores with a thin cobalt film which has a long domain size along the channel direction.

Figure 5-41 shows the dependence of the dc-magnetization as a function of the applied magnetic field for 5, 77, and 300 K for *Co*-**8A-2**, respectively. The measurements do not show hysteresis, the coercivity is zero, and saturation is not achieved at high external fields. This is typical of a paramagnetic material.

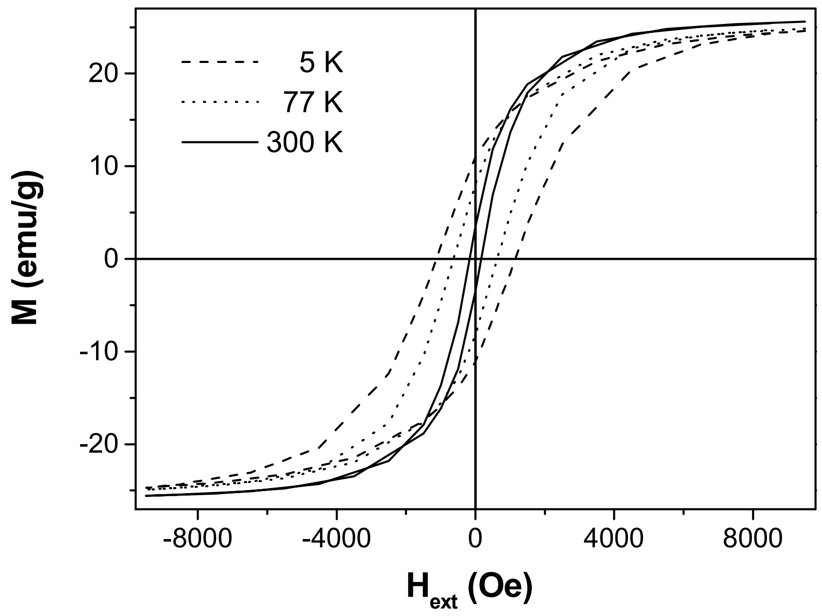

*Figure 5-42: dc-magnetization as a function of the applied field for the reduced nanostructured host/guest compound Co-**8A-2-R** at 5, 77, and 300 K.*

In contrast, the reduced form of *Co*-**8A-2-R** shows typical ferromagnetic behavior as it is shown in Figure 5-42. The reduction has led to a reduction of the cobalt oxide to the metal although the metal is still associated to oxygen on silica surface as shown by the XAS results (cf. section 5.3.3, page 102). A nearly temperature independent saturation of 25 emu/g is found. Hysteresis is observed up to room temperature and the coercivities increase with decreasing temperature.

5.4 Conclusions

The formation of nanostructured iron oxides, ternary cobalt iron oxides, and cobalt oxides located more or less exclusively within the mesoporous host structure of the MCM-48 silica material was proved by powder X-ray diffraction, nitrogen physisorption, and transmission electron microscopy. Information on the structure of the nanostructured oxides was obtained by X-ray absorption spectroscopy as an element-specific technique which provides qualitative and quantitative information on the local structure, which is not accessible by methods like P-XRD in case of these nanostructured host/guest compounds.

In a sequential combination of drying and calcination procedures haematite nanostructures were synthesized within the mesoporous silica host system. Various loadings with iron oxide were also achieved by impregnation with various iron nitrate concentrations. The typical P-XRD reflections of the mesoporous host system show a decrease in intensity with raising amounts of iron oxide incorporated into the mesoporous channel system due to destructive interferences. In the 2θ region above 20° the P-XRD diagrams do not exhibit any reflections that are indicative of bulk iron oxides. Nitrogen adsorption/desorption measurements still reveal mesoporosity for the host/guest compounds although a reduction of the BET surface area and the pore radius occurs, both being indications of a decoration/coating of the inner surface of the silica walls. The analysis of the XANES reveal the occurrence of iron(III) ions only. Comprehensive EXAFS analyses proved the existence of small slightly disordered iron oxide nanoparticles, in which FeO_6 octahedra are less strongly linked together than in bulk haematite. HRTEM investigations supported the synthesis of a host/guest compound by showing that the mesoporous host structure is still intact after the impregnation/calcination cycles. In addition, no diffuse intensity or superlattice reflections were observed by selected area electron diffraction, indicating that the iron is randomly distributed within the pore structure and not present in a crystalline state. Random intensity deviations and extra intensity modulations within the pores show that the iron oxide filling is not equivalent in all pores.

The reduction of the iron oxide host/guest compounds requires higher hydrogen concentrations in comparison to bulk haematite. While the reduction of bulk iron oxide leads to iron(0) the reduction of the host/guest compounds leads only to a partial reduction of iron(III) to iron(II). The so produced iron(II) iron(III) oxide exhibits a drastic change in the magnetic susceptibility and the dc-magnetization in comparison to the original paramagnetic iron(III) oxide; the reduced nanostructured material shows typical ferromagnetic behavior. The absence of antiferromagnetism in the original nanostructured iron(III) oxide prove that no large haematite particles were formed during the synthesis within the entire sample.

The first in-situ formation of a ternary transition metal oxide within the mesopores of MCM-48 silica was achieved with the cobalt iron oxide phase. XRD measurements showed the preservation of the host structure as well as the formation of 5-6 nm small particles. The analysis of nitrogen physisorption data revealed the existence of mesopores with smaller pore diameters and surface areas in comparison to the pristine silica phase, which can be attributed to the introduction of the Co/Fe/O phase into the mesopores. The XANES results show that only cobalt(II) and iron(III) are present in the nanostructured host/guest compounds. Together with the qualitative EXAFS analyses the formation of $CoFe_2O_4$ nanoparticles is confirmed.

Cobalt oxide nanoparticles were also formed within the mesopores of the MCM-48 silica phase. XRD measurements showed the preservation of the host structure as well as the formation of 5-6 nm small particles. In comparison to the pristine silica phase the formation of the cobalt nanostructures within the mesopores leads to smaller pore diameters and surface areas in the nitrogen physisorption analysis.

The formation of cobalt(0) within the mesoporous host system was achieved by the reduction of the nanostructured cobalt oxide host/guest compound. While the broad reflections in the P-XRD vanish due to the reduction of the cobalt oxide the XANES investigations indicate a reduction to cobalt(0). This is supported by the EXAFS analysis which exhibits a strong reduction of the Co-O shell. The two Co-Co shells that are characteristic of the Co_3O_4 merge together to one shell in the reduced compound with a 0.5 Å larger Co-Co distance in comparison to bulk cobalt(0). This indicates a strong disorder in this nanostructured coating of the mesoporous host system. The formation of the nanostructured Co(0) within the mesopores leads to a change from the paramagnetic behavior, which is found for the Co_3O_4 within the mesopores, to a typical ferromagnetic behavior as expected.

These results show that the combination of powder X-ray diffraction, X-ray absorption spectroscopy, high resolution electron microscopy and diffraction, and nitrogen adsorption/desorption measurements is very powerful; these techniques clearly demonstrate that highly dispersed transition metal oxide nanoparticles have been formed almost exclusively within the mesopores silica phases. The reduction of iron oxide and cobalt oxide leads to new nanostructured magnetic materials.

6 Summary

Over the last eight years ordered mesoporous molecular sieves (denoted as M41S) have expanded the range of uniform pore sizes from the micropore to the mesopore regime. From this development great attention arose for different fields of materials science, i.e. catalysis, nanostructured host-guest compounds, and physisorption materials. Originally, this family has been classified into three subgroups: A hexagonal (MCM-41), a cubic (MCM-48) and a lamellar phase (MCM-50). In contrast to the usually investigated hexagonal MCM-41 silica phase with its one-dimensional pore system this work focuses mainly on the cubic MCM-48 phase, which bears the great advantage of a three-dimensional pore system.

For the first time mesoporous MCM-48 silica phases with narrow pore size distributions were synthesized with pore diameters from 2.3 to 3.5 nm (BJH calculation), or 3.4 to 4.8 nm respectively (NLDFT calculation), with one surfactant species of tetraalkylammonium bromide type (cf. chapter 3). Rather than by investigation of a whole synthesis field the formation of the larger mesopores was achieved by the synthesis of commercially unavailable surfactants with various head groups. Apart from these MCM-48 silica materials, mesoporous MCM-41 silica materials with comparable narrow pore size distributions and pore diameters from 2.2 to 3.0 nm (BJH calculation), or 3.3 to 4.3 nm respectively (NLDFT calculation), were synthesized with trimethylalkylammonium bromide surfactants. Both the MCM-48 and MCM-41 silica materials show a high degree of long-range order in the P-XRD diagrams and high specific surface areas (900 – 1400 m^2/g). The increase of the pore diameter of the MCM-48 silica phases depends linearly on the hydrocarbon chain length of the used surfactant. Electron diffraction and high resolution transmission electron microscopy on the MCM-48 silica prove the $I4_1/a\bar{3}2/d$ space group of the material as well as the very high degree of long-range order as already found by P-XRD.

Systematic physisorption studies on the phase behavior of nitrogen, argon and krypton at 77 K and 87 K were performed for different, highly ordered pristine mesoporous MCM-48 silica materials and for a MCM-48 silica/iron(III) oxide host-guest compound (cf. chapter 4). Various methods (BJH, SF, Gurvich) were applied for the pore size analysis of pristine MCM-48 silica; the obtained results are in reasonably good agreement with each other. Since the NLDFT method is still not well-established for silica surfaces, the BJH formula is applied to the mesoporous M41S phases, keeping in mind that this well-known method generally underestimates the pore size by ca. 1.0 nm. Nevertheless it allows the determination of relative changes. The application of other methods which correct this underestimation is not appropriate, as these methods (see also Chapter 1.2.1) give no advantage in the estimation of an absolute value in comparison to the classic BJH method. Since all these methods only allow a comparison of mesoporous materials to each other, the advantage of the BJH method lies in its implementation in most of the commercially available physisorption computer programs.

The physisorption results indicate that for silica materials argon pore condensation at 77 K ($T - T_R = -6.5$ K) can only be observed in pores of diameters of less than ca.12 nm. Accordingly, argon physisorption isotherms at liquid nitrogen temperature should only be used for physisorption as long as all pores are smaller than ca. 12 nm in diameter.

The occurrence of physisorption hysteresis in M41S silica depends on temperature, pore size, and pore geometry, i.e. the thermodynamic states of pore fluid and bulk fluid. Nitrogen physisorption data at 77 K on all MCM-48 and MCM-41 do not reveal any physisorption hysteresis, whereas in case of argon physisorption at 87 K a small hysteresis loop is detected for a pore diameter D_p,N_2(BJH) of ca. 2.8 nm, but not for pores smaller than 2.5 nm. In contrast, argon physisorption data at 77 K reveal pore condensation and hysteresis for all MCM-48 and MCM-41 silica, even for a pore diameter of ca. 2.1 nm. The widths of the hysteresis loops decrease with decreasing pore diameter, in accordance with the expectation that the fluid confined to smaller pores is closer to pore criticality than the fluid in wider pores. Argon physisorption isotherms at 77 K and 87 K in MCM-48 silica also show that the width of the hysteresis loop decreases with increasing temperature as expected from theoretical predictions. The different physisorption behavior for nitrogen and argon at 77 K can be explained as a consequence of the lower temperature T/T_c of argon compared to nitrogen, where T_c is the critical temperature of the bulk fluid (T/T_c(Ar) = 0.51; T/T_c(N_2) = 0.61). The occurrence of pore condensation and hysteresis in argon physisorption isotherms at 77 K for MCM-48 silica with BJH pore diameter < 3 nm reveals that the (*quasi*) triple point of the pore fluid is shifted by at least 6.5 K to lower temperature in comparison to the bulk fluid. In contrast, argon physisorption isotherms at 77 K in the much wider pores of controlled-pore glass (16nm) which were also investigated for comparison do not show any pore condensation, indicating that in such wide pores the pore condensation line does not extend down to this temperature for pressures up to the corresponding bulk sublimation pressure. Phase transitions and pronounced physisorption hysteresis of type H1 are also found for krypton physisorption at 87 K in MCM-48 silica, i.e. ca. 28.5 K below the bulk triple point temperature. As in case of argon physisorption (77 K) the width of the hysteresis loop decreases with decreasing pore diameter, but is still observed for a BJH pore diameter as small as 2.1 nm.

The mesopores of MCM-48 and MCM-41 silica were characterized by nitrogen and argon physisorption. Both materials show reversible pore condensation without hysteresis in the nitrogen physisorption. Pore size distributions and mean pore diameters are comparable in sharpness and size. The argon physisorption data at 87 K and 77 K exhibit pore condensation with hysteresis. For both temperatures the hysteresis loop obtained for the MCM-48 silica material is significantly smaller in comparison to the hysteresis loop of the MCM-41 silica material.

NLDFT pore size calculations for nitrogen and argon physisorption data were applied to highly ordered mesoporous MCM-48 silica with BJH pore diameters above 3 nm for the first time. Although the MCM-48 silica phase consists of an interconnected pore structure, the results show clearly that the desorption branch of the hysteresis loop reflects the equilibrium phase transition. This observation confirms that hysteresis even in interconnected pore systems like the MCM-48 silica network is indeed associated with the development of metastable fluid states in the pore condensation process. These results clearly show that in case of hysteresis even in interconnected pore systems the desorption branch has to be used for the pore size analysis.

Nitrogen and argon physisorption data at 77 K and 87 K indicate that the impregnation of a pristine MCM-48 silica phase with iron(III) nitrate leads to a coating of the inner pore walls. In addition, the observed physisorption and pore condensation behavior of nitrogen, argon and krypton in MCM-48 silica/iron(III) oxide is qualitatively similar to pristine MCM-48 silica, indicating that the mesoporous host structure is still intact.

Nanostructured iron oxides, ternary cobalt iron oxides, and cobalt oxides were synthesized within the mesoporous host structure of MCM-48 silica materials. Powder X-ray diffraction, nitrogen physisorption, and transmission electron microscopy prove that the nanostructures are located almost exclusively within the mesopores. Information on the nanostructure of the oxides is obtained by X-ray absorption spectroscopy which provides both qualitative and quantitative information on the local structure (cf. chapter 5).

Various loadings with iron oxide were achieved by repeated impregnation/ calcination cycles or by single impregnation with various iron nitrate concentrations. P-XRD diagrams do not exhibit any reflections that are indicative of bulk iron oxides. Nitrogen physisorption measurements still show type IV isotherms with a reduction of the BET surface and the pore diameter, indicating a decoration/coating of the inner surface of the silica walls. Analysis of the XANES region reveals the occurrence of iron(III) exclusively. Comprehensive EXAFS analysis proves the existence of slightly disordered iron oxide nanoparticles consisting of less strongly linked FeO_6 in comparison to bulk haematite. HRTEM investigations reveal that the mesoporous host structure is still intact after the formation of the host/guest compound. Diffuse intensity or superlattice reflections are not observed by selected area electron diffraction, indicating that iron is randomly distributed within the pore structure. Chemical reduction of the iron oxide host/guest compounds requires higher hydrogen concentrations in comparison to bulk haematite. While the reduction of bulk iron oxide leads to iron(0) the reduction of the host/guest compounds leads only to a partial reduction of iron(III) to iron(II) as indicated by XAS investigations. This mixed iron(II)/ iron(III) oxide exhibits a ferromagnetic behavior typical of iron oxides as magnetite.

A ternary transition metal oxide (cobalt iron oxide) was synthesized within the mesopores of MCM-48 silica for the first time. XRD measurements exhibit the formation of 5-6 nm small particles the mesoporous host structure beeing preserved. Nitrogen physisorption data reveal the existence of mesopores with smaller pore diameters and surface areas as compared to the pristine silica phase, which can be attributed to the introduction of the Co/Fe/O phase into the mesopores. XANES analysis shows that only cobalt(II) and iron(III) are present in the nanostructured host/guest compounds. In combination with the qualitative EXAFS analyses the formation of $CoFe_2O_4$ nanoparticles is proved.

Cobalt oxide nanoparticles were also formed within the mesopores of the MCM-48 silica phase. Comparable to the cobalt ferrite within the MCM-48 silica the formation of 5-6 nm small particles is found by the P-XRD while the mesoporous host structure is maintained. The reduction of the inner surface and pore diameter is also comparable.

The formation of cobalt(0) within the mesoporous host system was achieved by chemical reduction of the nanostructured cobalt oxide host/guest compound with hydrogen. The broad reflections in the P-XRD vanish due to this reduction while the XANES investigations indicate a reduction of most cobalt(II)/(III) to cobalt(0). This is supported by EXAFS analysis which shows a strong reduction of the Co-O shell. The two Co-Co shells that are characteristic of Co_3O_4 merge together to one shell in the reduced compound with a Co-Co distance which is 0.5 Å larger in comparison to bulk cobalt(0). This indicates a high degree of disorder in this nanostructured coating of the mesoporous host system. The formation of the nanostructured Co(0) within the mesopores leads to a change of the paramagnetic behavior that is found for Co_3O_4 to a typical ferromagnetic behavior as expected.

7 Zusammenfassung (German Summary)

Seit dem ersten Bericht über die geordneten mesoporösen Molekularsiebe (sogenannte M41S Phasen) im Jahr 1992 haben diese großes Interesse auf sich gezogen. Man schreibt ihnen zahlreiche potentielle Anwendungsmöglichkeiten zum Beispiel in der Katalyse, in der Chemie der Wirt/Gast Verbindungen und als neue Adsorbentien in der Porenanalyse zu. Diese Familie wurde in drei Untergruppen eingeteilt: Eine hexagonale (MCM-41), eine kubische (MCM-48) und eine lamellare Phase (MCM-50). Im Gegensatz zu den hexagonalen MCM-41 Silicaphasen mit ihren „quasi“ eindimensionalen Porensystemen wird im folgenden hauptsächlich die kubische MCM-48 Silicaphase betrachtet, die den großen Vorteil eines dreidimensionalen Porennetzwerkes hat.

Erstmalig wurden MCM-48 Silicaphasen mit Porengrößen von 2.3 bis 3.5 nm (berechnet nach der BJH-Methode), bzw. 3.4 bis 4.8 nm (berechnet mit der NLDFT (*N*on-*L*ocal *D*ensity *F*unctional *T*herory)) mit nur einer Spezies von Tensiden synthetisiert (vgl. Kapitel 3). Dazu wurden zum Teil kommerziell nicht erhältliche Tenside synthetisiert und durch gezieltes Kopfgruppendesign in ihrem Phasenverhalten den Bedürfnissen angepaßt. Außer den mesoporösen MCM-48 Silicaphasen wurden ebenfalls mesoporöse MCM-41 Silicaphasen mit Porendurchmessern von 2.2 bis 3.0 nm (BJH), bzw. 3.3 bis 4.3 nm (NLDFT) mit Trimethylalkylammoniumbromiden synthetisiert. Sowohl die MCM-48 als auch die MCM-41 Silicaphasen sind durch ein ausgesprochen hohes Maß an Ordnung in den Röntgenpulverdiagrammen gekennzeichnet. Sie weisen hohe spezifische Oberflächen und relativ schmale Porendurchmesserverteilungen auf. Für den Porendurchmesser der MCM-48 Silicaphasen läßt sich eine lineare Zunahme von der Länge der Alkylkette des benutzten Tensids ableiten. Hochauflösende Elektronenmikroskopie und Elektronenbeugung zeigen, daß die hergestellten MCM-48 Silicaphasen der $I4_1/a\bar{3}2/d$ Raumgruppe angehören und von ausgesprochen hoher Qualität sind.

Das Phasenverhalten von Stickstoff, Argon und Krypton bei 77 und 87 K wurde für verschiedene, hochgeordnete mesoporöse MCM-48 Silicaphasen und für eine nanostrukturierte Eisen(III)/MCM-48 Silica Wirt/Gast-Verbindung systematisch untersucht (vgl. Kapitel 4). Unterschiedliche Methoden (BJH, SF, Gurvich) wurden zur Porengrößenanalyse herangezogen; die erhaltenen Werte zeigen für Porenvolumen und Porendurchmesser gute Übereinstimmung. Unter Berücksichtigung der Tatsache, daß die NLDFT-Methode noch nicht allgemein akzeptiert ist, obwohl ein entsprechendes Porenmodell für die MCM-48 Silicaphase existiert, ist die Berechnung von Porengrößenverteilungen mit dem BJH-Modell sinnvoll. Dabei ist jedoch zu beachten, daß dieses Modell die tatsächlichen Porendurchmesser um ca. 1.0 nm unterschätzt, wenn sie auf mesoporöse M41S-Phasen mit Porendurchmessern unter 5 nm angewendet wird. Trotzdem erlaubt sie die Ermittlung von relativen Änderungen der Porengrößenverteilung. Die Anwendung anderer Methoden, die den Fehler der BJH-Methode empirisch korrigieren, ist nicht gerechtfertigt, solange auch diese Methoden keine absoluten Werte liefern (siehe Kapitel 1.2.1). Der große Vorteil der BJH-Methode liegt in ihrer großen Verbreitung, da sie ist in den gängigen, kommerziell erhältlichen Computerprogrammen zur Porenanalyse enthalten ist und somit von einer großen Anzahl derer, die sich mit diesen Materialien beschäftigen, genutzt wird.

Die Ergebnisse der Argon-Physisorptionsmessungen an den mesoporösen MCM-48 Silicaphasen und an CPG-Materialien (controlled pore glass) zeigen, daß eine Porenkondensation bei 77 K ($T - T_R = -6.5$ K) nur bei Materialien mit Porendurchmessern unter ca. 12 nm beobachtet werden kann. Dementsprechend sollte Argon bei der Temperatur flüssigen Stickstoffs nur für die Analyse von Materialen benutzt werden, deren Poren alle kleiner als 12 nm sind.

Das Auftreten von Hystereseschleifen bei der Physisorption an M41S Silica hängt von Temperatur, Porengröße und Porengeometrie ab, z.B. den thermodynamischen Zuständen von Porenflüssigkeit und „bulk“-Flüssigkeit. Die Stickstoff-Physisorptionsdaten bei 77 K zeigen keine Hysterese für die verwendeten MCM-48 und MCM-41 Silicaphasen. Die entsprechenden Argon-Physisorptionmessungen bei 87 K weisen dagegen für einen Porendurchmesser D_p,N_2(BJH) von ca. 2.8 nm eine kleine Hystereseschleife auf. Für Poren kleiner als 2.5 nm ist jedoch keine Hystereseschleife mit Argon bei 87 K zu detektieren, im Gegensatz zu den Argon-Physisorptionmessungen bei 77 K. Diese zeigen Porenkondensation und Hysterese für alle untersuchten MCM-48 und MCM-41 Silica, sogar bei einem Porendurchmesser von lediglich 2.1 nm. Die Breite der Hystereseschleifen nimmt dabei mit steigendem Porendurchmesser zu, in Übereinstimmung mit der Erwartung, daß die Porenflüssigkeit in kleineren Poren näher am „porenkritischen“ Punkt ist als die Flüssigkeit in größeren

Poren. Die Physisorptionsisothermen bei 77 K und 87 K in MCM-48 Silica zeigen des weiteren, daß die Breite der Hystereseschleife mit zunehmender Temperatur abnimmt, wie es aufgrund theoretischer Betrachtungen zu erwarten ist. Das unterschiedliche Sorptionsverhalten von Stickstoff und Argon bei 77 K kann dadurch erklärt werden, daß die reduzierte Temperatur T/T_c für Argon kleiner ist als für Stickstoff (T_c ist die kritische Temperatur der „bulk“-Flüssigkeit: T/T_c (Ar) = 0.51; T/T_c (N_2) = 0.61). Das Auftreten von Porenkondensation und Hysterese bei den Argon-Physisorptionsmessungen bei 77 K für die MCM-48 Silica mit Porendurchmessern unter 3 nm zeigt, daß der (quasi-) Tripelpunkt der Porenflüssigkeit um mindestens 6.5 K zu niedriger Temperatur verschoben ist im Vergleich zur „bulk“-Flüssigkeit. Im Gegensatz dazu zeigen die Argon-Physisorptionisothermen bei 77 K in CPG, welches eine mittlere Porengröße von 16 nm hat, keine Porenkondensation. Dies demonstriert, daß für solch große Poren die Porenkondensationslinie nicht zu so tiefen Temperaturen herab reicht. Phasenübergänge und deutliche Hysteresen von Typ H1 werden auch für Krypton-Physisorptionmessungen bei 87 K in MCM-48 Silica gefunden, immerhin 28.5 K unter der Tripelpunktstemperatur der „bulk“-Flüssigkeit. Ebenso wie bei den Argon-Physisorptionmessungen bei 77 K nimmt die Breite der Hystereseschleifen mit fallendem Porendurchmesser ab und es wird sogar für einen Porendurchmesser von 2.1 nm noch eine Hysterese beobachtet.

Die MCM-48 und MCM-41 Silicaphasen zeigen reversible Porenkondensation ohne Hysterese für Stickstoff bei 77 K. Die Porengrößenverteilungen und die mittleren Porendurchmesser sind vergleichbar, sowohl in der Schärfe als auch in der Größe. Die Argon-Physisorptionsdaten bei 87 K und 77 K zeigen hingegen Porenkondensation mit Hysteresen vom Typ H1 für beide Silicaphasen. Sowohl bei 87 K als auch bei 77 K ist die Hystereseschleife für die MCM-48 Silicaphase merklich schmaler im Vergleich zu der MCM-41 Silicaphase.

Zum ersten Mal wurde die NLDFT Methode zur vergleichenden Porengrößenberechnung für Stickstoff- und Argon-Physisorptionsmessungen auf hochgeordnete mesoporöse MCM-48 Silica mit Porendurchmessern über 3 nm angewendet. Obwohl die MCM-48 Silicaphase aus einem dreidimensional verbundenen Porensystem besteht, zeigen die Ergebnisse deutlich, daß die Desorptionsäste der Hystereseschleifen den Gleichgewichtsphasenübergang widerspiegeln. Diese Beobachtung bestätigt, daß die Hysterese sogar in dreidimensional verbundenen Porensystemen wie dem der MCM-48 Silicaphase von metastabilen Zustände der Porenflüssigkeit abhängig ist.

Daraus folgt unmittelbar, daß sogar bei Porennetzwerken immer der Desorptionsast der Hystereseschleife zur Bestimmung der Porenparameter verwendet werden sollte.

Stickstoff- und Argon-Physisorptionmessungen bei 77 K und 87 K zeigen, daß die Imprägnierung hochgeordneter MCM-48 Silicaphasen mit Eisen(III)nitrat zu einer Beschichtung der Porenwände führt. Außerdem beweist das beobachtete Physisorptions- und Porenkondensationsverhalten von Stickstoff, Argon und Krypton an der nanostrukturierten Eisen(III)oxid/MCM-48 Silica Wirt/Gast-Verbindung, daß das mesoporöse Wirtsystem noch völlig intakt ist.

Nanostrukturierte Eisenoxide, ternäre Cobalteisenoxide und Cobaltoxide wurden innerhalb der Mesoporen von MCM-48 Silicaphasen synthetisiert. Röntgenpulverbeugung, Stickstoff-Physisorption, hochauflösende Transmissionelektronenmikroskopie und Elektronenbeugung beweisen, daß sich die gebildeten Nanostrukturen fast ausschließlich innerhalb des mesoporösen Wirtsystems befinden. Informationen über die Nanostruktur der Oxide wurden aus Röntgenabsorptionsmessungen erhalten, welche nach Auswertung sowohl qualitative als auch quantitative Auskunft über die lokale Struktur geben. Durch chemische Reduktion wurde das magnetische Verhalten der Nanostrukturen deutlich verändert. (vgl. Kapitel 5).

Verschiedene Konzentrationen von Eisenoxid im mesoporösen Wirtsystem wurden entweder durch wiederholte Imprägnierung und Calcination oder durch einzelne Imprägnierung mit unterschiedlich konzentrierten Eisennitratlösungen erreicht. Die Röntgenpulverdiffraktogramme zeigen keine Reflexe des Eisen(III)oxids. Stickstoff-Physisorptionsmessungen zeigen die für Mesoporen typischen Typ-IV Isothermen. Die Abnahmen der spezifischen Oberflächen und Porendurchmesser in Abhängigkeit von der eingebrachten Menge an Eisenoxid zeigen, daß das Eisenoxid als Schicht auf den Porenwänden lokalisiert ist. Die Analyse der XANES zeigt nur Eisen in der Oxidationstufe (III). Die umfassende Analyse der EXAFS-Messungen beweist die Existenz von ungeordneten Eisenoxid-Nanopartikeln, die im Vergleich zu „bulk"-Hämatit aus FeO_6-Oktaedern ohne Flächenverknüpfungen bestehen. Wie zuvor die Physisorptionsmessungen zeigen die HRTEM Untersuchungen, daß die mesoporöse Struktur des Wirtsystems nach der Einlagerung der Gastspezies noch intakt ist. In der Elektronenbeugung werden keine diffusen Intensitäten oder zusätzliche Reflexe von Fremdphasen beobachtet. Dies zeigt, ebenso wie die EDX Analyse, daß das Eisen statistisch an den Porenwänden verteilt ist. Die chemische Reduktion der nanostrukturierten Eisenoxide benötigt deutliche höhere Wasserstoffkonzentrationen im Vergleich zum „bulk“-Hämatit. Während die Reduktion von „bulk“-Hämatit zu elementarem Eisen führt, ergibt die Reduktion der Eisenoxid-Wirt/Gastverbindung nur teilweise eine Reduktion von Eisen der Oxidationstufe (III) zu (II), wie anhand von XAS-Untersuchungen gezeigt wurde. Das so anteilig erzeugte gemischte Eisen(II)/Eisen(III)oxid zeigt ferromagnetisches Verhalten, wie es z.B. für Magnetit typisch ist.

Erstmalig wurde ein ternäres Übergangsmetalloxid (Cobalteisenoxid) innerhalb der Mesoporen von MCM-48 Silica synthetisiert. Die Röntgenpulverdiffraktometrie zeigt die Bildung von 5-6 nm großen Nanopartikeln unter Erhaltung der Stuktur des Wirtsystems. Die Stickstoff-Physisorptiondaten beweisen ebenfalls den Erhalt des mesoporösen Wirtsystems, verbunden mit einer geringen Abnahme des mittleren Porendurchmessers und einer Abnahme der spezifischen Oberfläche im Vergleich zur MCM-48 Ausgangsphase. Dies kann der Einbringung der Co/Fe/O-Phase in die Mesoporen des Wirtsystems zugeschrieben werden. Die XANES zeigt, daß ausschließlich Cobalt(II) und Eisen(III) in den nanostrukturierten Wirt/Gast-Verbindungen aufzufinden sind. In Kombination mit den qualitativen EXAFS Analysen konnte die Bildung von $CoFe_2O_4$-Nanoteilchen gezeigt werden.

Cobaltoxid-Nanopartikel wurden ebenfalls innerhalb des mesoporösen MCM-48 Silica Wirtsystems gebildet. Aus den Röntgenpulverdaten wurde ähnlich wie beim Cobalteisenoxid unter Erhalt der Wirtstruktur des MCM-48 Silica die Bildung 5-6 nm großer Partikel ermittelt. Die Reduktion der spezifischen Oberflächen und der Porendurchmesser ist ebenfalls vergleichbar. Die Bildung von elementarem Cobalt innerhalb des mesoporösen Wirtsystems wurde durch chemische Reduktion des nanostrukturierten Cobaltoxids mit Wasserstoff erreicht. Die für das nanostukturierte Cobaltoxid charakteristischen breiten Reflexe in den Röntgenpulverdiagrammen verschwinden nach der Reduktion. XANES-Untersuchungen zeigen eine Verschiebung des zweiten Wendepunktes der Co-Absorptionkante von Cobalt (II)/(III) zu Cobalt 0. Dieses Ergebnis wird von der Analyse der EXAFS-Daten gestützt, die eine starke Reduktion der Koordinationszahl der Co-O-Schale zeigt. Die zwei Co-Co-Schalen, die im Co_3O_4 zu finden sind, verschmelzen im reduzierten Nanokomposit zu einer Schale; nur eine Co-Co-Schale, die 0.5 Å größer ist im Vergleich zum elementaren Cobalt ist noch aufgelöst. Diese Ergebnisse geben die gestörte Ordnung und die Nähe des nanostrukturierten, elementaren Cobalts zum Wirtsystem der MCM-48 Silicaphasen wieder. Die Bildung des nanostrukturierten elementaren Cobalts führt zu einer Änderung des paramagnetischen Verhaltens, welches für das nanostrukturierte Co_3O_4 gefunden wird, zu einem typischen ferromagnetischen Verhalten, wie es für elementares Cobalt zu erwarten ist.

8 References

[1] C. T. Kresge, M. E. Leonowicz, W. J. Roth, J. C. Vartuli, J. S. Beck, *Nature* **1992**, *359*, 710.

[2] J. S. Beck, J. C. Vartuli, W. J. Roth, M. E. Leonowicz, C. T. Kresge, K. D. Schmitt, C. T.-W. Chu, D. H. Olson, E. W. Sheppard, S. B. McCullen, J. B. Higgins, J. L. Schlenker, *J. Am. Chem. Soc.* **1992**, *114*, 10834.

[3] K. S. W. Sing, D. H. Everett, R. A. W. Haul, L. Mouscou, R. A. Pierotti, J. Rouquerol, T. Siemieniewska, *Pure & Appl. Chem.* **1985**, *57*, 603.

[4] P. Behrens, *Adv. Mater.* **1993**, *5*, 127.

[5] P. J. Branton, P. G. Hall, K. S. W. Sing, *J. Chem. Soc., Chem. Commun.* **1993** 1257.

[6] P. J. Branton, P. G. Hall, K. S. W. Sing, H. Reichert, F. Schüth, K. K. Unger, *J. Chem. Soc., Faraday Trans.* **1994**, *90*, 2965.

[7] J. H. Petropoulos, *Langmuir* **1996**, *12*, 4814.

[8] K. Morishige, H. Fujii, M. Uga, D. Kinukawa, *Langmuir* **1997**, *13*, 3494.

[9] M. Kruk, M. Jaroniec, R. Ryoo, J. M. Kim, *Chem. Mater.* **1999**, *11*, 2568.

[10] P. I. Ravikovitch, A. V. Neimark, *Langmuir* **2000**, *16*, 2419.

[11] M. Thommes, R. Köhn, M. Fröba, *Stud. Surf. Sci. Catal.* **2000**, *128*, 259.

[12] M. Thommes, R. Köhn, M. Fröba, *J. Phys. Chem. B* **2000**, *104*, 7932.

[13] J. C. Vartuli, A. Malek, W. J. Roth, C. T. Kresge, S. B. McCullen, *Microporous Mesoporous Mater.* **2001**, *44-45*, 691.

[14] M. Thommes, R. Köhn, M. Fröba, *Stud. Surf. Sci. Catal.* **2001**, *135*, 17-P-12.

[15] K. Moller, T. Bein, *Chem. Mater.* **1998**, *10*, 2950.

[16] R. Köhn, G. Bouffaud, O. Richard, G. van Tendeloo, M. Fröba, *Mat. Res. Soc. Symp. Proc.* **1999,** *547*, 81.

[17] A. Reller, S. Ebbinghaus, R. Köhn, M. Fröba, U. Sazama, P. Fortunato, *Mat. Res. Soc. Sym. Proc.* **1999**, *547*, 75.

[18] M. Fröba, R. Köhn, G. Bouffaud, O. Richard, G. van Tendeloo, *Chem. Mater.* **1999**, *11*, 2858.

[19] L. Chen, P. J. Klar, W. Heimbrodt, F. Brieler, M. Fröba, *Appl. Phys. Lett.* **2000**, *76*, 3531.

[20] R. Köhn, F. Brieler, M. Fröba, *Stud. Surf. Sci. Catal.* **2000**, *129*, 341.

[21] A. Corma, *Chem. Rev.* **1997**, *97*, 2373.

[22] J. Y. Ying, C. P. Mehnert, M. S. Wong, *Angew. Chem. Int. Ed.* **1999**, *38*, 56.

[23] R. Köhn, M. Fröba, *Catal. Today* **2001**, *68*, 227.

[24] C. Minchev, R. Köhn, T. Tsoncheva, M. Dimitrov, M. Fröba, *Stud. Surf. Sci. Catal.* **2001**, *135*, 07-P-19.

[25] Q. Huo, D. I. Margolese, U. Ciesla, D. G. Demuth, P. Feng, T. E. Gier, P. Sieger, A. Firouzi, B. F. Chmelka, F. Schüth, G. D. Stucky, *Chem. Mater.* **1994**, *6*, 1176.

[26] P. T. Tanev, T. J. Pinnavaia, *Science* **1995**, *267*, 865.

[27] S. A. Bagshaw, E. Prouzet, T. J. Pinnavaia, *Science* **1995**, *269*, 1242.

[28] D. M. Antonelli, A. Nakahira, J. Y. Ying, *Inorg. Chem.* **1996**, *35*, 3126.

[29] M. Fröba, M. Tiemann, *Chem. Mater.* **1998**, *10*, 3475.

[30] Q. Huo, D. I. Margolese, U. Ciesla, P. Feng, T. E. Gier, P. Sieger, R. Leon, P. M. Petroff, F. Schüth, G. Stucky, *Nature* **1994**, *368*, 317.

[31] A. Sayari, *Chem. Mater.* **1996**, *8*, 1840.

[32] X. S. Zhao, G. Q. Lu, G. J. Millar, *Ind. Eng. Chem. Res.* **1996**, *35*, 2075.

[33] J. S. Beck, J. C. Vartuli, *Curr. Opin. Solid State Mater. Sci.* **1996**, *1*, 76.

[34] P. Behrens, *Angew. Chem. Int. Ed.* **1996**, *35*, 515.

[35] D. Zhao, P. Yang, Q. Huo., B. F. Chmelka, G. D. Stucky, *Curr. Opin. Solid State Mater. Sci.* **1998**, *3*, 111.

[36] M. Linden, S. Schacht, F. Schüth, A. Steel, K. K. Unger, *J. Porous. Mater.* **1998**, *5*, 177.

[37] U. Ciesla, F. Schüth, *Microporous Mesoporous Mater.* **1999**, *27*, 131.

[38] M. E. Davis, C.-Y. Chen, S. Burkett, R. F. Lobo, *Mat. Res. Soc. Symp. Proc.* **1994**, *346*, 831.

[39] C.-F. Cheng, Z. Chan, J. Klinowski, *Langmuir* **1995**, *11*, 2815.

[40] T. Yanagisawa, T. Shimizu, K. Kuroda, C. Kato, *Bull. Chem. Soc. Jpn.* **1990**, *63*, 988.

[41] S. Inagaki, Y. Fukushima, K. Kuroda, *J. Chem. Soc., Chem. Commun.* **1993**, 680.

[42] T. Yanagisawa, T. Shimizu, K. Kuroda, C. Kato, *Bull. Chem. Soc. Jpn.* **1999**, *63*, 988.

[43] R. Schmidt, M. Stöcker, D. Akporiaye, E. H. Torstad, A. Olsen, *Microporous Mater.* **1995**, *5*, 1.

[44] M. W. Anderson, *Zeolites* **1997**, *19*, 220.

[45] V. Alfredsson, M. W. Anderson, *Chem. Mater.* **1996**, *8*, 1141.

[46] V. Alfredsson, M. W. Anderson, T. Ohsuna, O. Terasaki, M. Jacob, M. Bojrup, *Chem. Mater.* **1997**, *9*, 2066.

[47] K. Schumacher, P. I. Ravikovitsch, A. Du Chesne, A. V. Neimark, K. K. Unger, *Langmuir* **2000**, *16*, 4648.

[48] A. Carlsson, M. Kaneda, Y. Sakamoto, O. Terasaki, R. Ryoo, S. H. Joo, *J. Electron Microscopy*, **1999**, *48*, 795.

[49] T. Wärnheim, A. Jönsson, *J. Colloid. Interface Sci.* **1988**, *125*, 627.

[50] X Auvray, C. Petipas, R. Anthore, I. Rico, A. Lattes, *J. Phys. Chem.* **1989**, *93*, 7458.

[51] S. S. Funari, G. Rapp, *J. Phys. Chem. B* **1997**, *101*, 732.

[52] A. Monnier, F. Schüth, Q. Huo, D. Kumar, D. Margolese, R. S. Maxwell, G. D. Stucky, M. Krishnamurty, P. Petroff, A. Firouzi, M. Janicke, B. F. Chmelka, *Science* **1993**, *261*, 1299.

[53] G. D. Stucky, A. Monnier, F. Schüth, Q. Huo, D. Margolese, D. Kumar, M. Krishnamurty, P. Petroff, A. Firouzi, M. Janicke, B. F. Chmelka, *Mol. Crystl. Liq. Cryst.* **1994**, *240*, 187.

[54] J. C.Vartuli, K. D. Schmitt, C. T. Kresge, W. J. Roth, M. E. Loenowicz, S. B. McCullen, S. D. Hellring, J. S. Beck, J. L. Schlenker, D. H. Olson, E. W. Sheppard, *Chem. Mater.* **1994**, *6*, 2317.

[55] C. A. Fyfe, G. Fu, *J. Am. Chem. Soc.* **1995**, *117*, 9709.

[56] A. A. Romero, M. D. Alba, W. Zhou, J. Klinowski, *J. Phys. Chem. B* **1997**, *101*, 5294.

[57] P. Behrens, A. Glaue, C. Haggenmüller, G. Schechner, *Solid State Ionics* **1997**, *101-103*, 255.

[58] K. W. Gallis, C. C. Landry, *Chem. Mater.* **1997**, *9*, 2035.

[59] P. Van Der Voort, M. Mathieu, F. Mees, E. F. Vansant, *J. Phys. Chem. B* **1998**, *102*, 8847.

[60] A. Corma, Q. Kann, F. Rey, *Chem. Commun.* **1998**, 579.

[61] F. Chen, L. Huang, Q. Li, *Chem. Mater.* **1997**, *9*, 2685.

[62] J. Xu, Z. Luan, H. He, W. Zhou, L. Kevan, *Chem. Mater.* **1998**, *10*, 3690.

[63] J. M. Kim, S. K. Kim, R. Ryoo, *Chem. Commun.* **1998**, 259.

[64] Q. H. Huo, D. I. Margolese, G. D. Stucky, *Chem. Mater.* **1996**, *8*, 1147.

[65] Unpublished results, B-Teil, Ingo Reulecke, Hamburg, 2000.

[66] J. N. Israelachvili, D. J. Mitchell, B. W. Ninham, *J. Chem. Soc, Faraday Trans. 2* **1976**, *72*, 1525.

[67] J. N. Israelachvili, D. J. Mitchell, B. W. Ninham, *Biochim. Biophys. Acta* **1977**, *470*, 185.

[68] R. Ryoo, C. H. Ko, I.-S. Park, *Chem. Commun.* **1999**, 1413.

[69] A. Sayari, *J. Am. Chem. Soc.* **2000**, *122*, 6504.

[70] E. P. Barrett, L. G. Joyner, P. P. Halenda, *J. Amer. Chem. Soc.* **1951**, *73*, 373.

[71] M. Kruk, M. Jaroniec, A. Sayari, *Langmuir* **1997**, *13*, 6267.

[72] R. Ryoo, S. H. Joo, J. M. Kim, *J. Phys. Chem. B* **1999**, *103*, 7435.

[73] M. Kruk, M. Jaroniec, R. Ryoo, S. H. Joo, *Chem. Mater.* **2000**, *12*, 1414.

[74] Q. Huo, R. Leon, P. M. Petroff, G. D. Stucky, *Science* **1995**, *268*, 1324.

[75] D. Zhao, Q. Huo, J. Feng, J. Kim, Y. Han, G. D. Stucky, *Chem. Mater.* **1999**, *11*, 2668.

[76] M. Benjelloun, P. Van der Voort, P. Cool, O. Collart, E. F. Vansant, *Phys. Chem. Chem. Phys.* **2001**, *3*, 127.

[77] K. Schumacher, M. Grün, K. K. Unger, *Microporous Mesoporous Mater.* **1999**, *27*, 201.

[78] G. Schulz-Ekloff, J. Rathousky, A. Zukal, *Microporous Mesoporous Mater.* **1999**, *27*, 273.

[79] C. Danumah, S Vaudreuil, L. Bonneviot, M. Bousmina, S. Giasson, S. Kaliaguine, *Microporous Mesoporous Mater.* **2001**, *44-45*, 241.

[80] M. L. Pena, Q. Kan, A. Corma, F. Rey, *Microporous Mesoporous Mater.* **2001**, *44-45*, 9.

[81] M. Hartmann, C. Bischof, *J. Phys. Chem. B* **1999**, *103*, 6230.

[82] T. Tatsumi, K. A. Koyano, Y. Tanaka, S. Nakata, *J. Porous Mater.* **1999**, *6*, 13.

[83] S. Jim, J. M. Kim, R. Ryoo, Y.-S. Ahn, M.-H. Han, *Microporous Mesoporous Mater.* 2000, *41*, 119.

[84] C. G. Sonwane, S. K. Bathia, N. Calos, *Ind. Eng. Chem. Res.* **1998**, *37*, 2271.

[85] A. V. Neimark, P. I. Ravikovitch, A. Vishnyakov, *Phys. Rev. E* **2000**, *62*, R1493.

[86] S. J. Gregg, K. S. W. Sing, *Adsorption, Surface Area and Porosity*; Academic Press: London, **1982**.

[87] F. Rouquerol, J. Roquerol, K. S. W. Sing, *Adsorption by Powders & Porous Solids*; Academic Press: London, **1999**.

[88] D. H. Everett, *In The Solid-Gas Interface*; E. A. Flood, Ed.; Marcel Dekker: Vol. 2 New York, **1967**.

[89] P. C. Ball, R. Evans, *Langmuir* **1989**, *5*, 714.

[90] G. J. Mason, *Colloid Interface Sci.* **1982**, *88*, 36.

[91] G. J. Mason, *Colloid Interface Sci.* **1983**, *95*, 277.

[92] A. V. Neimark, J. Russian, *Phys. Chem.* **1986**, *60*, 1045.

[93] H. Liu, L. Zhang, N. A. Seaton, *Langmuir* **1993**, *9*, 2576.

[94] H. Liu, N. A. Seaton, *Chem. Enging. Sci.* **1994**, *49*, 1869.

[95] J. H. Page, J. Liu, B. Abeles, E. Herbolzheimer, W. A. Deckmann, D. A. Weitz, *Phys. Rev. E.* **1995**, *52*, 2763.

[96] M. W. Cole, W. F. Saam, *Phys. Rev. Lett.* **1974**, *32*, 985.

[97] A. Papadopolou, F. van Swol, U. M. B. Marconi, *J. Chem. Phys.* **1992**, *97*, 6942.

[98] G. H. Findenegg, S. Gross, T. Michalski, *Stud. Surf. Sci. Catal.* **1994,** *87*, 71.

[99] G. H. Findenegg, M. Thommes, *Physical Adsorption: Experiment, Theory and Applications*, J. Fraissard, Ed.; Kluwer: Dordrecht, **1997**.

[100] D. D. Awschalom, J. Warnock, M .W. Shafer, *Phys. Rev. Lett.* **1996**, *57*, 1607.

[101] P. Tarazona, U. M. B. Marconi, R. Evans, *Molecular Physics*, **1987**, *60*, 543.

[102] R. Evans, *Phys. Condens. Matter* **1990**, *2*, 8989.

[103] K. Binder, D. P. J. Landau, *Chem. Phys.* **1992**, *96*, 1444.

[104] C. M. Lastoskie, K. Gubbins, N. Quirke, *J. Phys. Chem.* **1993**, *97*, 4786.

[105] J. P. R. P. Walton, N. Quirke, *Mol. Simulation* **1989**, *2*, 361.

[106] K. E. Gubbins, *Physical Adsorption: Experiment, Theory and Applications*, J. Fraissard, Ed.; Kluwer: Dordrecht, **1997**.

[107] M. E. Fisher, H. J. Nakanishi, *Chem. Phys.* **1981**, *75*, 5857.

[108] Y. K. Tovbin, E. V. Votyakov, *Langmuir* **1993**, *9*, 2652.

[109] C. Eyrad, M. Brun, L. Eyraud, A. Lallemand, P. C. R. Eyraud, *Acad. Sc. Paris* **1971**, *273 (B)*, 645.

[110] H. M. Fretwell, J. A. Duffy, A. P. Clarke, M. A. Alam, R. Evans, *J. Phys.: Condens. Matter* **1996**, *8*, 9613.

[111] H. Dominguez, M. P. Allen, R. Evans, *Mol. Phys.* **1998**, *96*, 209.

[112] M. Thommes, G. H. Findenegg, *Langmuir* **1994**, *10*, 4270.

[113] L. D. Gelb, K. E. Gubbins, R. Radhakrishnan, M. Sliwinska-Bartkowiak, *Rep. Prog. Phys.* **1999**, *62*, 1573.

[114] L. Sarkisov, P. A. Monson, *Stud. Surf. Sci. Catal.* **2000**, 128, 21.

[115] P. J. Branton, P. G. Hall, K. S. W. Sing, *J. Chem. Soc., Chem. Commun.* **1993**, 1257.

[116] O. Franke, G. Schulz-Ekloff, J. Rathousky, J. Starek, A. Zukal, *J. Chem. Soc., Chem. Commun.* **1993**, 724.

[117] K. Morishige, H. Fujii, M. Uga, D. Kinukawa, *Langmuir* **1997**, *13*, 3948.

[118] M. Kruk, M. Jaroniec, A. Sayari, *J. Phys. Chem. B* **1997**, *101*, 583.

[119] J. Rathousky, A. Zukal, O. Franke, G. J. Schulz-Ekloff, *Chem. Soc., Faraday Trans.* **1994**, *90*, 2821.

[120] R. Schmidt, M. Stöcker, E. Hansen, D. Akporiaye, O. H. Ellestad, *Microporous Mater.* **1995**, *3*, 443.

[121] P. I. Ravikovitch, S. C. O. Domhnaill, A. V. Neimark, F. Schüth, K. K. Unger, *Langmuir* **1995**, *11*, 4765.

[122] P. Ravikovitch, D. Wie, W. T. Church, G. L. Haller, A. W. Neimark, *J. Phys. Chem. B* **1997**, *101*, 3671.

[123] A. V. Neimark, P. I. Ravikovitch, M. Grün, F. Schüth, K. K. Unger, *J. Colloid Interface Sci.* **1998**, *207*, 159.

[124] C. G. Sonwane, S. K. Bathia, N. Calos, *Ind. Eng. Chem. Res.* **1998**, *37*, 2271.

[125] F. Marlow, M. D. McGehee, D. Zhao, B. F. Chmelka, G. D. Stucky, *Adv. Mater.* **1999**, *11*, 632.

[126] Z. Y. Yuan, S. Q. Liu, T. H. Chen, J. Z. Wang, H. X. Li, *J. Chem. Soc., Chem. Commun.* **1995**, 973.

[127] T. Abe, Y. Tachibana, T. Uematsu, M. Iwamoto, *J. Chem. Soc., Chem. Commun.* **1995**, 1617.

[128] R. Ryoo, S. H. Joo, S. Jun, *J. Phys. Chem. B* **1999**, *103*, 7743.

[129] M. Kruk, M. Jaroniec, R. Ryoo, S. H. Joo, *J. Phys. Chem. B* **2000**, *104*, 7960.

[130] S. H. Joo, S. Jun, R. Ryoo, *Microporous Mesoporous Mater.* **2001**, *44-45*, 153.

[131] J. Lee, S. Yoon, T. Hyeon, S. M. Oh, K. B. Kim, *Chem. Commun.* **1999**, 2177.

[132] S. B. Yoon, J. Y. Kim, J.-S. Yu, *Chem. Commun.* **2001**, 559.

[133] M. S. Morey, A. Davidson, G. D. Stucky, *J. Porous Mater.* **1998**, *5*, 195.

[134] L.-Z. Wang, J.-L. Shi, W.-H. Zhang, M.-L. Ruan, J. Yu, D.-S. Yan, *Chem. Mater.* **1999**, *11*, 3015.

[135] R. Schmidt, H. Junggreen, M. Stöcker, *Chem. Commun.* **1996**, 875.

[136] H. Kosslick, G. Lischke, H. Landmesser, B. Parlitz, W. Storek, R. Fricke, *J. Catal.* **1998**, 176, 102.

[137] A. A. Romero, M. D. Alba, J. Klinowski, *J. Phys. Chem. B* **1998**, *102*, 123.

[138] F. Chen, F. Song, Q. Li, *Microporous Mesoporous Mater.* **1999**, *29*, 305.

[139] K. Schumacher, C. du Fresne von Hohenesche, K. K. Unger, R. Ulrich, A. Du Chesne, U. Wiesner, H. W. Spiess, *Adv. Mater.* **1999**, *11*, 1194.

[140] Z. Chang, R. M. Krishna, J. Xu, R. Koodali, L. Kevan, *Phys. Chem. Chem. Phys.* **2001**, *3*, 1699.

[141] Z. Y. Yuan, Q. Luo, J. Q. Liu, T. H. Chen, J. Z. Wang, H. X. Li, *Microporous Mesoporous Mater.* **2001**, *42*, 289.

[142] W. Z. Zhang, T. J. Pinnavaia, *Catal. Lett.* **1996**, *38*, 261.

[143] S. Kawi, M. Te, *Catal. Today* **1998**, *44*, 101.

[144] M. Hartmann, S. Racouchot, C Bischof, *Chem. Commun.* **1997**, 2367.

[145] M. Hartmann, S. Racouchot, C. Bischof, *Microporous Mesoporous Mater.* **1999**, *27*, 309.

[146] B. Echchahed, A. Moen, D. Nicholson, L. Bonneviot, *Chem. Mater.* **1997**, *9*, 1716.

[147] D. Y. Zhao, D. J. Goldfarb, *J. Chem. Soc., Chem. Commun.* **1995**, 875.

[148] J. Xu, Z. Luan, M. Hartmann, L. Kevan, *Chem. Mater.* **1999**, *11*, 2928.

[149] M. S. Morey, J. D. Bryan, S. Schwarz, G. D. Stucky, *Chem. Mater.* **2000**, *12*, 3435.

[150] P. Ferreira, I. S. Goncalves, F. E. Kühn, A. D. Lopes, M. A. Martins, M. Pillinger, A. Pina, J. Rocha, C. C. Romao, A. M. Santos, T. M. Santos, A. A. Valente, *Eur. J. Inorg. Chem.* **2000**, 2263.

[151] K. K. Kang, W. S. Ahn, *J. Molecul. Catal. A: Chemical* **2000**, *159*, 403.

[152] M. Morey, A. Davidson, G. Stucky, *Microporous Mater.* **1996,** *6*, 99.

[153] M. S. Morey, S. O'Brien, S. Schwarz, G. D. Stucky, *Chem. Mater.* **2000**, *12*, 898.

[154] K. A. Koyano, T. Tatsumi, *Chem. Commun.* **1996**, 145.

[155] J. V. Walker, M. Morey, H. Carlsson, A. Davidson, G. D. Stucky, A. Butler, *J. Am. Chem. Soc.* **1997**, *119*, 6921.

[156] M. Anpo, H. Yamashita, K. Ikeue, Y. Fujii, S. G. Zhang, Y. Ichihashi, D. R. Park, Y. Suzuki, K. Koyano, T. Tatsumi, *Catal. Today* **1998**, *44*, 327.

[157] W. S. Ahn, D. H. Lee, T. J. Kim, J. H. Kim, G. Seo, R. Ryoo, *Appl. Catal. A: General* **1999**, *181*, 39.

[158] P. Ferreira, I. S. Goncalves, F. E. Kühn, M. Pillinger, J. Rocha, A. M. Santos, A. Thursfield, *Eur. J. Inorg. Chem.* **2000**, 551.

[159] M. L. Pena, V. Dellarocca, F. Rey, A. Corma, S. Coluccia, L. Marchese, *Microporous Mesoporous Mater.* **2001**, *44-45*, 345.

[160] M. Widenmeyer, S. Grasser, K. Köhler, R. Anwander, *Microporous Mesoporous Mater.* **2001**, *44-45*, 327.

[161] K. Schrijnemakers, E. F. Vansant, *J. Porous Mater.* **2001**, *8*, 83.

[162] M. Morey, A. Davidson, H. Eckert, G. Stucky, *Chem. Mater.* **1996**, *8*, 486.

[163] P. Van Der Voort, M. Morey, G. D. Stucky, M. Mathieu, E. F. Vansant, *J. Phys. Chem. B* **1998**, *102*, 585.

[164] P. Van Der Voort, M. Baltes, E. F. Vansant, *J. Phys. Chem. B* **1999**, *103*, 10102.

[165] P. Van Der Voort, E. F. Vansant, *Microporous Mesoporous Mater.* **2000**, *38*, 385.

[166] M Mathieu, P. Van Der Voort, B. M. Weckhuysen, R. R. Rao, G. Catana, R. A. Schoonheydt, E. F. Vansant, *J. Phys. Chem. B* **2001**, *105*, 3393.

[167] M. L. Pena, A. Dejoz, V. Fornes, F. Rey, M. I. Vazquez, J. M. Lopez Nieto, *Appl. Catal. A: General* **2001**, *209*, 155.

[168] M. S. Morey, G. D. Stucky, S. Schwarz, M. Fröba, *J. Phys. Chem. B* **1999**, *103*, 2037.

[169] D. A. Jaeger, S. G. Rusell, H. Suinozaki, *J. Org. Chem.* **1994**, *59*, 7544.

[170] L. Chen, T. Horiuchi, T. Mori, K. Maeda, *J. Phys. Chem. B* **1999,** *103*, 1216.

[171] S. Brunauer, P. H. Emmet, E. Teller, *J. Am. Chem. Soc.* **1938**, *60*, 309.

[172] T. Ressler, *J. Synchrotron Rad.* **1998**, *5*, 118.

[173] J .J. Rehr, J. Mustre de Leon, S. I. Zabinsky, R. C. Albers, *J. Am. Chem. Soc.* **1991**, *113*, 5135.

[174] A. H. Schoen, *Infinite Periodic Minimal Surfaces without intersections*; NASA Technical Note *TD-5541*, **1970**.

[175] J. M. Thomas, O. Terasaki, P. L. Gai, W. Zhou, J. Gonzalez-Calbet, *Acc. Chem. Res.* **2001**, *34*, 583.

[176] A. Saito, H. C. Foley, *AIChE Journal* **1991**, *37*, 429.

[177] A. Saito, H. C. Foley, *Microporous Mater.* **1995**, *3*, 531.

[178] G. Horvath, K. J. Kawazoe, *Chem. Eng. Jpn.* **1983**, *16*, 474.

[179] A. Galarneau, D. Desplantier, R. Dutartre, F. Di Renzo, *Microporous Mesoporous Mater.* **1999**, *27*, 297.

[180] C. M. Lastoskie, K. E. Gubbins, *Stud. Surf. Sci. Catal.* **2000**, *128*, 41.

[181] C. Nguyen, D. D. Do, *Langmuir* **1999**, *15*, 3608.

[182] S. Inoue, Y. Hanzawa, K. Kaneko, *Langmuir* **1998**, *14*, 3079.

[183] M. W. Maddox, J. P. Olivier, K. E. Gubbins, *Langmuir* **1997**, *13*, 1737.

[184] S. Groß, G. H. Findenegg, *Ber. Bunsenges. Phys. Chem.* **1997**, *101*, 1726.

[185] V. A. Rabinovich, A. A. Vasserman, V. I. Neodostup, L. S. Veksler, *Thermophysical Properties of Neon, Argon, Krypton and Xenon*, Hemisphere Publishing: Washington DC, **1988**.

[186] C. G. V. Burgess, D. H. Everett, S. Nuttall, *Pure & Appl. Chem.* **1989**, *61*, 1845.

[187] M. Kruk, M. Jaroniec, *Chem. Mater.* **2000**, *12*, 222.

[188] M. Janicke, D. Kumar, G. D. Stucky, B. F. Chmelka, *Zeolites and Related Microporous Materials: State of the Ar*t; J. Weitkamp, H. G. Karge, H. Pfeifer, W. Hölderich, Eds.; Elsevier: Amsterdam, **1994**.

[189] B. Marler, U. Oberhagemann, S. Vortmann, H. Gies, *Microporous Mater.* **1996**, *6*, 375.

[190] C. J. Glinka, J. M. Nicol, G. D. Stucky, E. Ramli, D. Margolese, Q. Huo, J. B. Higgins, M. E. Leonowicz, *J. Porous Mater.* **1996**, *3*, 93.

[191] M. H. Lim, C. F. Blanford, A. Stein, *Chem. Mater.* **1998**, *10*, 467.

[192] W. Hammond, E. Prouzet, S. D. Mahanti, T. J. Pinnavaia, *Microporous Mesoporous Mater.* **1999**, *27*, 19.

[193] M. Fröba, O. Muth, *Adv. Mater.* **1999**, *11*, 564.

[194] A. Manceau, V. A. Drits, *Clay Miner.* **1993**, *28*, 165.

[195] R. M. Cornell, U. Schwertmann, *The Iron Oxide*s; VCH Verlagsgesellschaft: Weinheim, **1996**.

[196] R. L. Blake, R. E. Hessevick, T. Zoltai, L. W. Finger, *Am. Mineral.* **1966**, *51*, 123.

[197] E. A. Stern, *Phys. Rev. B* **1993**, *48*, 9825.

[198] B. K. Teo, *EXAFS: Basic Principles and Data Analysi*s; Springer-Verlag; Berlin, **1986**.

[199] A. H. Morrish, *Canted Antiferromagnetism: Hematite*; World Scientific; Singapore, **1994**.

[200] F. Brieler, M. Fröba, L. Chen, P. J. Klar, W. Heimbrodt, H.-A. Krug von Nidda, A. Loidl, *Chem. Eur. J.* **2001**, in press.

[201] G. Will, N. Masciocchi, W. Parrish, M. Hart, *J. Appl. Chem.* **1987**, *20*, 394.

[202] W. L. Roth, *J. Phys. Chem. Solids* **1964**, *25*, 1.

[203] M. Respaud, J. M. Broto, H. Rakoto, A. R. Fert, L. Thomas, B. Barbara, M. Verelst, E. Dnoeck, P. Lecante, A. Mosset, J. Osuna, T. Ould Ely, C. A. Miens, B. Chaudret, *Phys. Rev. B* **1998**, *57*, 2925.

I.I Abbreviations

θ	contact angle of the liquid meniscus against the pore wall
ρ	density
σ	molecular diameter
χ	magnetic susceptibility
α	fluid-wall interaction parameter
$\chi(k)$	normalized EXAFS oscillation as function of the wave vector
ξ_0	reduced area per crystallographic unit cell
σ^2	Debye-Waller factor
$2\ \theta_{hkl}$	2 theta angle of the diffraction peak hkl
a	unit cell parameter
a_0	effective head group area
A_s	specific surface
BAM	Bundesanstalt für Materialforschung und -prüfung
BET	Brunauer, Emmet and Teller
BJH	Barret-Joyner-Halenda
BTs	backtransforms
$C_{12}TAB$	dodecyltrimethylammonium bromide
$C_{14}TAB$	tetradecyltrimethylammonium bromide
$C_{16}TAB$	hexadecyltrimethylammonium bromide
$C_{18}TAB$	octadecyltrimethylammonium bromide
$C_{20}DEMAB$	eicosanyldiethylmethylammonium bromide
$C_{20}EDMAB$	eicosanylethyldimethylammonium bromide
$C_{20}TAB$	eicosanyltrimethylammonium bromide
$C_{20}TEAB$	eicosanyltriethylammonium bromide
$C_{22}DEMAB$	docosanyldiethylmethylammonium bromide

C_{22}EDMAB	docosanylethyldimethylammonium bromide
C_{22}TAB	docosanyltrimethylammonium bromide
C_{22}TEAB	docosanyltriethylammonium bromide
CMK	carbons mesostructured by KAIST
CPG	controlled-pore glasses
CTAB	cetyltrimethylammonium bromide
DFT	density functional theory
D_h	hydraulic pore diameter
d_{hkl}	d-value of the diffraction peak hkl
D_p	pore diameter
E_0	energy shift
ED	electron diffraction
EDS	energy dispersive qualitative microanalysis
emu	electromagnetic unit
EXAFS	extended X-ray absorption fine structure
FSM	folded sheet mesoporous material
FTs	Fourier transforms
g	effective surfactant ion pair packing parameter
H_{ext}	external magnetic field
HK	Horvath-Kawazoe
hkl	Miller indices
HMS	hexagonal mesoporous silica
HRTEM	high resolution transmission electron microscopy
k	wave vector
k_b	Boltzmann constant
l	kinetic surfactant tail length or curvature elastic energy
LCT	liquid crystal templating

M	magnetization
MCM	Mobil composition of matter
MSU	Michigan State University
N	coordination number
N_{ind}	number of independent degrees of freedom
NLDFT	non-local density functional theory
p	pressure
p_0	saturation pressure of bulk fluid
PC_H	pore critical point
PEO	polyethylene oxide
PSD	pore size distribution
P-XRD	powder X-ray diffraction
R	bond length
R_k	so-called core radius
R_p	pore radius
s.c.	single-crystal data
SAED	selected area electron diffraction
SBA	Santa Barbara
SF	Saito-Foley
SQUID	superconducting quantum interference device
t	film thickness
t_c	thickness of an adsorbed multilayer film
T_c	critical temperature
TEM	transmission electron microscopy
TEOS	tetraethylorthosilicate
TMAOH	tetramethylammonium hydroxide
T_N	Néel temperature

TPR	temperature programmed reduction
t_{pw}	pore wall thickness
T_R	bulk fluid triple point temperature
V	volume
V_p	pore volume
XANES	X-ray absorption near-edge structure
XAS	X-ray absorption spectroscopy
$\Delta\mu d$	absorption jump

I.II Descriptors

MESOPOROUS SILICA MATERIALS

MCM-41**A**	MCM-41 silica synthesized with C_{12}TAB
MCM-41**B**	MCM-41 silica synthesized with C_{14}TAB
MCM-41**C**	MCM-41 silica synthesized with C_{16}TAB
MCM-48**A** MCM-48$\mathbf{A_1}$	MCM-48 silica synthesized with C_{14}TAB
MCM-48**B** MCM-48$\mathbf{B_1}$	MCM-48 silica synthesized with C_{16}TAB
MCM-48**C** MCM-48$\mathbf{C_1}$ MCM-48$\mathbf{C_2}$	MCM-48 silica synthesized with C_{18}TAB
MCM-48**D**	MCM-48 silica synthesized with C_{20}EDMAB
MCM-48**E**	MCM-48 silica synthesized with C_{22}EDMAB

IRON OXIDE WITHIN MESOPOROUS SILICA

Fe-**1A-1**	MCM-41 silica after impregnation/calcination with 0.07 M iron nitrate solution
Fe-**1A-2**	MCM-41 silica after impregnation/calcination with 0.37 M iron nitrate solution
Fe-**1A-3**	MCM-41 silica after impregnation/calcination with 1.18 M iron nitrate solution
Fe-**1A-4**	MCM-41 silica after impregnation/calcination with 4.87 M iron nitrate solution
Fe-**1A-4-R**	*Fe*-**1A-4** after chemical reduction
Fe-**8A-1**	MCM-48 silica after one impregnation/calcination cycle with 1.6 M iron nitrate solution
Fe-**8A-2**	MCM-48 silica after two impregnation/calcination cycles with 1.6 M iron nitrate solution
Fe-**8A-3**	MCM-48 silica after three impregnation/calcination cycles with 1.6 M iron nitrate solution

Fe-**8B-1**	MCM-48 silica after impregnation/calcination with 0.07 M iron nitrate solution
Fe-**8B-2**	MCM-48 silica after impregnation/calcination with 0.37 M iron nitrate solution
Fe-**8B-3**	MCM-48 silica after impregnation/calcination with 1.18 M iron nitrate solution
Fe-**8B-4**	MCM-48 silica after impregnation/calcination with 4.87 M iron nitrate solution
Fe-**8B-4-R**	*Fe*-**8B-4** after chemical reduction
$\mathbf{B_1\text{-}Fe_2O_3}$	MCM-48$\mathbf{B_1}$ silica after impregnation/calcination with 1.6 M iron nitrate solution

COBALT IRON OXIDE WITHIN MESOPOROUS SILICA

CoFe$_2$-**8A-1**	MCM-48 silica after impregnation/calcination with 1.6 M mixed (1:2) cobalt iron nitrate solution and tempering at 873 K for 72 hours
CoFe$_2$-**8A-2**	MCM-48 silica after impregnation/calcination with 1.6 M mixed (1:2) cobalt iron nitrate solution and tempering at 923 K for 72 hours

COBALT /COBALT OXIDE WITHIN MESOPOROUS SILICA

Co-**8A-1**	MCM-48 silica after impregnation/calcination with 0.8 M cobalt nitrate solution
Co-**8A-2**	MCM-48 silica after impregnation/calcination with 1.6 M cobalt nitrate solution
Co-**8A-2-R**	*Co*-**8A-2** after chemical reduction

I.III Hazardous chemicals

Information on potential hazards caused by the chemicals in this work according to the European Union classification.

compound	hazard category[1]	R phrase[2]	S phrase[3]
1-Bromodocosane	Xi	36/37/38	26-36
1-Bromoeicosane			22-24/25
cobalt(II) nitrate hexahydrate	Xn	22-40-43	36/37
diethylmethylamine	F, C	11-34	16-26-36/37/39-45
dimethylethylamine	F, C	12-20/22-34	3-16-26-36-45
dodecyltrimethylammonium bromide	Xi	36/37/38	26-36
ethanol	F	11	17-26
hexadecyltrimethylammonium bromide	Xn, N	22-36/38-50/53	26-39-61
iron(III) nitrate nonahydrate	O, Xi	8-36/38	26
octadecyltrimethylammonium bromide	Xi	36/37/38	26-36
potassium hydroxide	C	22-35	26-36/37/39-45
sodium hydroxide	C	35	26-37/39-45
sulfuric acid	C	35	26-30-45
tetradecyltrimethylammonium bromide	C	34	26-36/37/39-45
tetraethyl orthosilicate	Xn	10-20-36/37	
tetramethylammonium hydroxide	T	25-34	26-36/37/39-45
triethylamine	F, C	11-20/21/22-35	3-16-26-29-36/37/39-45
trimethylamine	F+, Xn	12-20-37/38-41	16-26-39

[1] O: incendiary; C: corrosive; F: flammable, F^+: extremely flammable; Xn: harmful to health; Xi: irritant; N: dangerous for the environment; T: toxic.

[2] R8: contact with combustible material may cause fire; R10: flammable;R11: highly flammable; R12: extremely flammable; R20: harmful on inhalation; R21: harmful in contact with skin; R22: harmful if swallowed; R25: toxic if swallowed;R34: causes burns; R35: causes severe burns; R36: irritating to eyes; R37: irritating to respiratory

system; R38: irritating to skin; R40: possible risks of irreversible effects; R41: risk of serious damage to eyes;R43: may cause sensitization by skin contact; R50: very toxic to aquatic organisms; R53: may cause long-term adverse effects in the aquatic environment.

[3] S3: keep in a cool place; S16: keep away from sources of ignition - No smoking; S17: keep away from combustible material; S22: do not breathe dust; S24: avoid contact with skin; S25: avoid contact with eyes;S26: in case of contact with eyes rinse immediately with plenty of water and seek medical advice; S29: do not empty into drains; S36: wear suitable protective clothing; S37: wear suitable gloves; S39: wear eye/face protection; S45in case of accident or if you feel unwell seek medical advice immediately (show the label where possible); S61: Avoid release into the environment.

II.I Thanks

Fist of all I would like to thank *Prof. Dr. Michael Fröba* for his excellent supervision, the opportunity to work in his group, on this thesis, and his continuous support over the last five years.

Thanks to the members of our group for their patience with my weird personality:

Dr. Olaf Muth, *Nadine Oberender*, *Dr. Michael Tiemann*, *Dr. Daniela Kempe*, and *Felix Brieler*.

Special thanks to *Uta Sazama* for her helping hand and mind.

Thanks to all the students and trainees who joined my work over the last five years:

Gaëlle Bouffaud, *Axel Wichmann*, *Frank Riedel*, *Sandra Obaid*, *Ulrike Baade*, *Ingo Reulecke*, *Jan Philip Plog*, *Christina Ehlers*, and *Stephan Hauschild*.

Also thanks to *Dr. Stefan Ebbinghaus*, *Sigrid Zeckert*, *Prof. Dr. Armin Reller*, *Dr. Karsten Schwarz*, *Dr. Thomas Rentschler*, and *Dr. Jan Hanss*.

For their collaboration I would like to thank:

- *Prof. Dr. Gustaav van Tendeloo* and *Dr. Olivier Richard* from the EMAT at the University of Antwerp (Belgium) for the transmission electron microscopy investigations.
- *Dr. Matthias Thommes* for the physisorption measurements with Argon and Krypton and the helpful discussions on sorption phenomena and their interpretation.
- *Dr. Christo Minchev* and his colleagues from the Bulgarian Academy of Science in Sofia for catalytic investigations on the iron and the copper nanostructures although they are not mentioned in this thesis.
- *Frank Wiekhorst* at the University of Hamburg for the magnetic measurements on the cobalt nanostructures.
- *Dr. Hans-Albrecht Krug von Nidda* at the University of Augsburg for the magnetic measurements on the iron nanostructures.

Special personal thanks to

- My sandpit-mate *Björn Wortmann* for his friendship and a job that students dream of.
- My oldest schoolmate *Tim Lemke* for the never-ending friendship and the spiritual unity.
- *My schoolmates Reno* and *Marco Plaumann* for their friendship over all the years.
- My schoolmate *Nils Heining* for his friendship and the years in our special "WG".
- My schoolmate *Tanja Sinn* for her friendship and the time we spent together.

Continuing special personal thanks to

- *Nils Rothe* for his friendship and the good times we spent together.
- *Gunnar Meinert* for his friendship and so many interesting conversation about almost everything and everybody.
- *Tuija Arola* for the friendship and the never ending principle discussions.
- *Michael Frank* for his continuous friendship over the time and distance.

Special thanks to my family, in particular:

My aunt *Giesla* and my uncle *Manfred* for their continuous interest and support in my life.

My brother *Bernd* and *Tatjana* and their recently born son *Nicolai*.

And last but not least I want to thank my parents:

my mother *Gertrud* for her continuous support and trust in whatever I did and my father *Hans* for the simple wisdom about life he gave to me.

Finally I would like to thank *Sabrina* for her love, patience, endurance, and her never-ending critical view on my personality.

II.II List of publications

Peer-reviewed paper

R. Köhn, G. Bouffaud, O. Richard, G. van Tendeloo, M. Fröba, Iron(III) oxide within mesoporous MCM-48 silica phases: Synthesis and characterization. *Mat. Res. Soc. Sym. Proc.* **1998**, *547*, 81.

A. Reller, S. Ebbinghaus, R. Köhn, M. Fröba, U. Sazama and P. Fortunato, Redox processes in polynary copper oxides and copper oxide/mesoporous silica composites. *Mat. Res. Soc. Sym. Proc.* **1998**, *547*, 75.

M. Fröba, R. Köhn, G. Bouffaud, O. Richard, G. van Tendeloo, Fe_2O_3 nanoparticles within mesoporous MCM-48 silicates: in-situ formation and characterization. *Chem. Mater.* **1999**, *11*, 2858.

M. Thommes, R. Köhn and M. Fröba, Systematic sorption studies on surface and pore size characteristics of different MCM-48 silica materials. *Stud. Surf. Sci. Catal.* **2000**, *128*, 259.

R. Köhn, F. Brieler, M. Fröba, Ternary transition metal oxides within mesoporous MCM-48 silica phases: Synthesis and characterization. *Stud. Surf. Sci. Catal* **2000**, *129*, 341.

M. Thommes, R. Köhn and M. Fröba, Sorption and pore condensation behavior of nitrogen, argon and krypton on MCM-48 silica materials. *J. Phys. Chem. B* **2000**, *104*, 7932.

R. Köhn and M. Fröba, Nanoparticles of 3d transition metal oxides in mesoporous MCM-48 silica host structures: Synthesis and characterization. *Catal. Today* **2001**, *68*, 227.

C. Minchev, R. Köhn, T. Tsoncheva, M. Dimitrov, M. Fröba, Preparation and characterization of copper oxide modified MCM-41 molecular sieves. *Stud. Surf. Sci. Catal.* **2001**, *135*, 07-P-19.

M. Thommes, R. Köhn and M. Fröba, Sorption and pore condensation behavior of pure fluids in mesoporous MCM-48 silica, MCM-41 silica and controlled pore glass. *Stud. Surf. Sci. Catal.* **2001**, *135*, 17-P-12.

T. Tsoncheva, M. Dimitrov, D. Paneva, I. Mitov, R. Köhn, M. Fröba, C. Minchev, Methanol decompostion on Fe_2O_3 / MCM-48 silica catalyst. *Reac. Kinetics Catal. Lett.* **2001**, submitted.

M. Thommes, R. Köhn and M. Fröba, Characterization of porous solids: Sorption and phase behavior of nitrogen, argon, and krypton in ordered and disorderd mesoporous silica materials (MCM-41, MCM-48, SBA-15, controlled pore glass, silica gel) at temperature above and below the bulk triple point. *AIChE J.* **2001**, submitted.

Reports and extended abstracts

R. KÖHN, G. BOUFFAUD, M. FRÖBA, Fe K-Edge EXAFS studies on iron oxides incorporated into mesoporous MCM-48 silica phases. *Hamburger Synchrotronstrahlungslabor (HASYLAB) Annual Report* **1998**, 807-808.

R. KÖHN, G. BOUFFAUD, M. FRÖBA, EXAFS investigations of iron(III) oxide nanoparticles within mesoporous MCM-48 silicates. *Hamburger Synchrotronstrahlungslabor (HASYLAB) Annual Report* **1999**, 795-796.

S. EBBINGHAUS, A. RELLER, R. KÖHN, M. FRÖBA, Reversible reduction and reoxidation of CuO and NiO within the pores of MCM-48 silicate. *Hamburger Synchrotronstrahlungslabor (HASYLAB) Annual Report* **1999**, 809-810.

M. FRÖBA, M. TIEMANN, N. OBERENDER, R. KÖHN, O. MUTH, D. KEMPE, J. WONG, G. SCHECHNER, P. BEHRENS, B. PILLEP, I. GROHMANN, A. HESS, E. KEMNITZ, H. THOMS, M. EPPLE, A. RELLER, XANES spectroscopy in the 1-2 keV Region: A synchrotron probe to investigate important low-Z materials. *Stanford Synchrotron Radiation Laboratory (SSRL) Activity Report* **1999**, 260-263.

R. KÖHN, F. BRIELER AND M. FRÖBA, Characterization of ternary transition metal oxides within mesoporous MCM-48 silica by XANES/EXAFS. *Hamburger Synchrotronstrahlungslabor (HASYLAB) Annual Report* **2000**, 767-768.

R. KÖHN, C. MINCHEV AND M. FRÖBA, Characterization of nanostructured copper oxide within mesoporous silica materials by XANES/EXAFS. *Hamburger Synchrotronstrahlungslabor (HASYLAB) Annual Report* **2001**, 759-760.

Oral presentations

R. KÖHN, G. BOUFFAUD, F. BRIELER, M. FRÖBA, Nanostructured host/guest compounds: Transition metal oxides in mesoporous silica. *VIIth European Conference on Solid State Chemistry*, Madrid (Spain), Sep. 15-18, 1999.

R. KÖHN, F. BRIELER, M. FRÖBA, Ternary transition metal oxides within mesoporous MCM-48 silica phases: Synthesis and characterization. *2nd Conference on Access in Nanoporous Materials*; Banff (Canada), May 25-30, 2000.

R. KÖHN, S. EBBINGHAUS, M. FRÖBA, In situ formation of metal and metal oxide nanostructures within highly ordered mesoporous MCM-48 silica phases. International Conference *Solid State Chemistry 2000*; Prague (Czech Republic), Sep. 3-8, 2000.

R. KÖHN, M. THOMMES, M. FRÖBA, Sorption and pore condensation behaviour of nitrogen, argon, krypton in mesoporous MCM-48 silica materials. *Xth Porotec Workshop*, Bad Soden (Germany), Nov. 15-16, 2000.

R. KÖHN AND M. FRÖBA. Nanoparticles of 3d transition metal oxides in mesoporous MCM-48 silica host structures: Synthesis and characterization. *221st ACS National Meeting*, San Diego (USA), Apr. 1-5, 2001.

R. KÖHN, U. SAZAMA, M. FRÖBA, Redox behavior of iron and copper oxide within mesoporous MCM-41/48 silica phases in comparison to the corresponding bulk oxides. *GEFTA Annual Meeting*, Munich (Germany), Sep. 9-13, 2001.

Poster presentations

R. KÖHN, G. BOUFFAUD, M. FRÖBA, Controlled coating of the inner surface of MCM-48 silica phases with hematite. *VIth European Conf. on Solid State Chemistry*, Zurich (Switzerland), Sep. 17-20, 1997.

R. KÖHN, GAËLLE BOUFFAUD, M. FRÖBA, Intracage chemistry: Nanostructured hematite synthesized within the mesopores of MCM-48 silica phases. *10th German Zeolite Conference*, Bremen (Germany), Mar. 9-11, 1998.

R. KÖHN, GAËLLE BOUFFAUD F. BRIELER, M. FRÖBA, Eisenoxide, Cobaltoxide und Eisencobaltoxide in mesoporösen MCM-48 Silicaphasen: Synthese und Charakterisierung. *9th German Conference on Solid State Chemistry*, Saarbrücken (Germany), Sep. 23-25, 1998.
R. KÖHN, GAËLLE BOUFFAUD F. BRIELER, M. FRÖBA, Binary and ternary iron/cobalt oxides within mesoporous MCM-48 silica phases: Synthesis and characterization. *Fall Meeting Materials Research Society*, Boston (USA), Nov. 30 – Dec. 5, 1998.

R. KÖHN, GAËLLE BOUFFAUD, M. FRÖBA, EXAFS investigations of iron(III) oxide nanoparticles within mesoporous MCM-48 silicates. *11th German Zeolite Conference*, Stuttgart (Germany), Mar. 3-5, 1999.

M. THOMMES, R. KÖHN, M. FRÖBA, Sorption studies on surface and pore size characteristics of different MCM-48 materials. *5th International Symposium on the Characterisation of Porous Solids (COPS V)*, Heidelberg (Germany), May 30 - June 2, 1999.

R. KÖHN AND M. FRÖBA, Synthese und Charakterisierung nanostrukturierter Übergangsmetalle und -metalloxide innerhalb mesoporöser Silicastrukturen. *3rd Antragskolloquium des Schwerpunktprogrammes „Reaktivität von Festkörpern“ der Deutschen Forschungsgemeinschaft (DFG)*, Bonn (Germany), Feb. 20-22, 2000.

R. KÖHN, G. BOUFFAUD, M. FRÖBA, EXAFS investigations of iron(III) oxide nanoparticles within mesoporous MCM-48 silicates. *HERCULES X Euroconference*, Grenoble (France), Apr. 6-9, 2000.

M. THOMMES, R. KÖHN, M. FRÖBA, Sorption studies on surface and pore size characteristics of different MCM-48 silica materials. *2nd Conference on Access in Nanoporous Materials*; Banff (Canada), May 25-30, 2000.

R. KÖHN, U. BAADE, M. FRÖBA, Parallel hydrothermal synthesis of mesoporous MCM-48 and MCM-41 silica materials in a single batch. *13th German Zeolite Conference*, Erlangen-Nuremberg (Germany), Mar. 7-9, 2001.

R. KÖHN, C. MINCHEV, T. TSONCHEVA, M. DIMITROV, M. FRÖBA, Preparation and characterization of copper oxide modified MCM-41 molecular sieves. *13th International Zeolite Conference*, Montpellier (France), July 8-13, 2001.

R. KÖHN, M. THOMMES, M. FRÖBA, Sorption and pore condensation behavior of pure fluids in mesoporous MCM-48 silica, MCM-41 silica and controlled pore glass. *13th International Zeolite Conference*, Montpellier (France), July 8-13, 2001.

II.III Curriculum Vitae

Ralf Köhn, born November 6, 1969 in Hamburg, Germany.

Education

1976-1980	Elementary school, Nahe in Schleswig-Holstein, Germany
1980-1989	Grammar school, *Lise-Meitner-Gymnasium*, Norderstedt in Schleswig-Holstein, Germany
May 1989	*Abitur*
June 1989 - Sep. 1990	National Civil Service at the *Arbeiter-Samariter-Bund*, Schleswig-Holstein, Germany
Apr. 1991 - Sep. 1991	Study of Chemistry and Physics at the *Technical University of Clausthal-Zellerfeld*, Germany
Oct. 1991 - July 1997	Study of Chemistry at the *University of Hamburg*, Germany
Sep. 28, 1993	*Diplomvorprüfung*
Jan. 1995 - Mar. 1995	Guest study at the *University of Sheffield*, Great Britain (biochemistry research project in the group of Dr. J. Grasby)
Apr. 1995 - Aug. 1995	Participant in three north-sea field trips (7 weeks on the research ships Valdivia and Heincke) of the *Transwatt* and *Custos* projects in the group of Priv.-Doz. Dr. U. Brockmann
Oct. 1996 - July 1997	Work on Diploma thesis *"Darstellung mesoporöser Silicate als Wirtstrukturen und die Synthese von nanostrukturierten Eisenoxiden innerhalb der Porensysteme"* in the group of Prof. Dr. Fröba at the Institute of Inorganic and Applied Chemistry at the University of Hamburg, Germany
July 31, 1997	*Diplom* in Chemistry
Aug. 1997 - Sep. 2001	Work on *Dissertation* (PhD Thesis) "*Synthesis, Characterization, and Modification of Various Mesoporous Silica Phases*" in the group of Prof. Dr. Fröba at the Institute

	of Inorganic and Applied Chemistry at the University of Hamburg, Germany
Apr. - Jul. 1997	Fellowship of *Werner-Ranz-Stiftung*
Oct. 6 - 17, 1997	Participant in the course “*Investigations on the dynamic of condensed matter by synchrotron radiation”* at the University of Rostock
Apr. 1998 - Sep. 2001	Scientific Assistant at the University of Hamburg
Feb. 27 - Mar. 9, 2000	Participation at the Higher European Research Course for Users of Large Experimental Systems HERCULES, Grenoble, France: *“Neutron and Synchrotron Radiation for Physics and Chemistry of Condensed Matter”*
May 2001	Best presentation award for the oral presentation of *“Nanoparticles of 3d transition metal oxides in mesoporous MCM-48 silica host structures: Synthesis and characterization”* at Symposium on Nanotechnology in Catalysis, ACS 211 National Meeting, San Diego, California, USA